

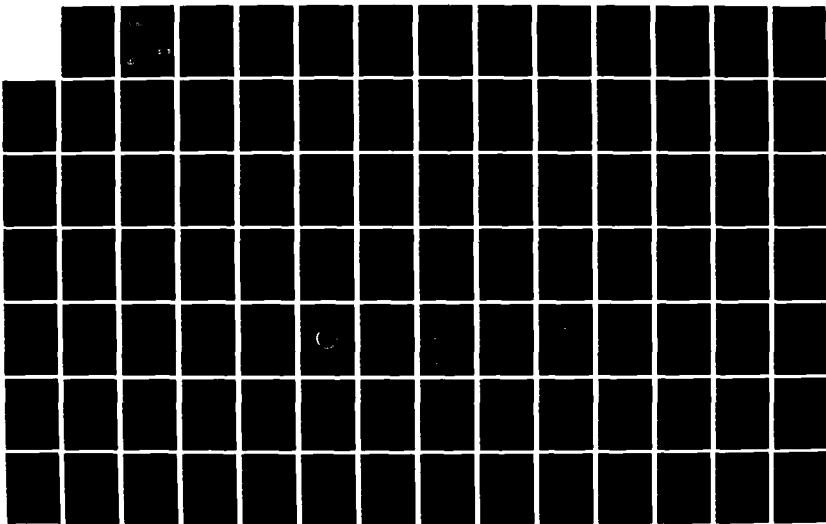
AD-A159 936

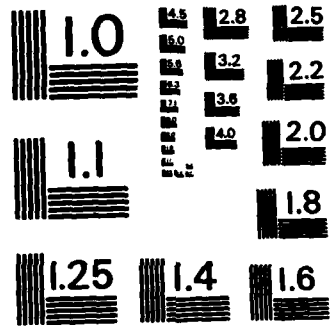
SOUND TRANSMISSION INTO SHELLS DOUBLY EXCITED BY
INCIDENT WAVES AND BY AR. (U) NAVAL SURFACE WEAPONS
CENTER SILVER SPRING MD G C GAUNAIRD ET AL. 15 JAN 85
NSWC/TR-85-42 F/G 20/1

172

UNCLASSIFIED

NL





MICROCOPY RESOLUTION TEST CHART
NATIONAL BUREAU OF STANDARDS-1963-A

NSWC TR 85-42

10

SOUND TRANSMISSION INTO SHELLS DOUBLY EXCITED BY INCIDENT WAVES AND BY ARBITRARY SURFACE FORCING FUNCTIONS

BY G. C. GAUNAURD J. BARLOW
RESEARCH AND TECHNOLOGY DEPARTMENT

15 JANUARY 1985

AD-A159 936

Approved for public release; distribution is unlimited.

DTIC
ELECTE
OCT 7 1985
S A D

DTIC FILE COPY



NAVAL SURFACE WEAPONS CENTER

Dahlgren, Virginia 22448 • Silver Spring, Maryland 20910

85 10 02 092

UNCLASSIFIED

SECURITY CLASSIFICATION OF THIS PAGE (When Data Entered)

REPORT DOCUMENTATION PAGE		READ INSTRUCTIONS BEFORE COMPLETING FORM
1. REPORT NUMBER NSWC TR 85-42	2. GOVT ACCESSION NO. AD-A159 936	3. RECIPIENT'S CATALOG NUMBER
4. TITLE (and Subtitle) SOUND TRANSMISSION INTO SHELLS DOUBLY EXCITED BY INCIDENT WAVES AND BY ARBITRARY SURFACE FORCING FUNCTIONS	5. TYPE OF REPORT & PERIOD COVERED FINAL--FY84	
	6. PERFORMING ORG. REPORT NUMBER	
7. AUTHOR(s) G. C. GAUNAURD AND J. BARLOW	8. CONTRACT OR GRANT NUMBER(s) N00014-84AF-00001 and 0004R01AA-850	
9. PERFORMING ORGANIZATION NAME AND ADDRESS Naval Surface Weapons Center (Code R43) 10901 New Hampshire Avenue Silver Spring, MD 20903-5000	10. PROGRAM ELEMENT, PROJECT, TASK AREA & WORK UNIT NUMBERS	
11. CONTROLLING OFFICE NAME AND ADDRESS	12. REPORT DATE 15 January 1985	
	13. NUMBER OF PAGES 112	
14. MONITORING AGENCY NAME & ADDRESS (if different from Controlling Office)	15. SECURITY CLASS. (of this report) UNCLASSIFIED	
	15a. DECLASSIFICATION/DOWNGRADING SCHEDULE	
16. DISTRIBUTION STATEMENT (of this Report) Approved for public release; distribution unlimited.		
17. DISTRIBUTION STATEMENT (of the abstract entered in Block 20, if different from Report)		
18. SUPPLEMENTARY NOTES Excerpts presented at a recent meeting of the Acoustical Society of America. Excerpts published in the Journal of the Acoustical Society of America.		
19. KEY WORDS (Continue on reverse side if necessary and identify by block number) Transmission of Sound Caustics Cylindrical Shell Loaded Shells Internal Sound Pressure Levels Dynamic Response Focusing Action of Shells Filtering Action of Shells		
20. ABSTRACT (Continue on reverse side if necessary and identify by block number) We develop the fundamental exact analytical and computational model required to study the transmission of incident plane sound waves into submerged elastic cylindrical shells subjected to arbitrary loads on their outer surface. We use the superposition principle in this linear problem to separate the contributions to the internally transmitted field caused by the incident wave from that of the surface load. This basic model uses the exact (2-D) formulation of elastodynamics to describe the shell motions,		

DD FORM 1 JAN 73 1473

EDITION OF 1 NOV 65 IS OBSOLETE
S/N 0102-LF-014-6601

UNCLASSIFIED
SECURITY CLASSIFICATION OF THIS PAGE (When Data Entered)

A

and that of general linear acoustics to describe the wave motion in the inner and outer fluids. We display the isobaric contours of the internally transmitted pressure fields, exhibiting their caustics and their progressive development as the frequency is increased within the band $0 < k_3 a < 10$. The contour plots are generated for all the possible combinations of loading and insonification conditions with a view toward computing an advantage ratio P_R which measures the gains that would result from sensing the internally transmitted field, rather than the field external to the shell. This advantage ratio is shown always to be greater than unity and, in many cases, much greater than unity. The effects of two basically different types of loads are analyzed via the isobaric plots, and also by means of spectral plots computed at several fixed points inside the shell. The effect of the monopole ($n=0$) mode of vibration on the internal pressure field is analyzed in detail. We study its spectral characteristics at fixed internal points, and its radial dependence at various frequencies. We observe an encouraging overall permanence of the caustic locations, at fixed frequencies, as the types of surface loads are varied. The present investigation of sound transmission into arbitrarily loaded shells clearly demonstrates the filtering behavior of the shell in the frequency domain, and its focusing action in space. Hence, for moderate surface loads, the air-filled submerged shell analyzed here acts as a very effective sound concentrator, particularly near the resonances of its monopole mode.

We have carried on a detailed computational study in the final sections of this report to quantitatively determine the effect of shell thickness, stiffness, and general material composition, on the sound fields transmitted into the loaded shells. This analysis makes the work valid for various metals and for shell relative-thicknesses between 1% and 20%, which is a range covering most practical cases. This final section shows that for all thicknesses and compositions, the large values of the advantage ratio P_R , still show large gains in sensing internal rather than external fields in all cases considered, provided the forcing (flow) function is below acceptable bounds.

Accession For	
NTIS CRA&I	<input checked="" type="checkbox"/>
DTIC TAB	<input type="checkbox"/>
Unannounced:	<input type="checkbox"/>
Justification	
By	
Distribution /	
Availability Codes	
Dist	Avail and/or Special
A1	



EXECUTIVE SUMMARY

We develop the fundamental exact analytical and computational model required to study the transmission of incident plane sound waves into submerged elastic cylindrical shells subjected to arbitrary loads on their outer surface. We use the superposition principle in this linear problem to separate the contributions to the internally transmitted field caused by the incident wave from that of the surface load. This basic model uses the exact (2-D) formulation of elastodynamics to describe the shell motions, and that of general linear acoustics to describe the wave motion in the inner and outer fluids. We display the isobaric contours of the internally transmitted pressure fields, exhibiting their caustics and their progressive development as the frequency is increased within the band $0 < k_3 a < 10$. The contour plots are generated for all the possible combinations of loading and insonification conditions with a view toward computing an advantage ratio P_R which measures the gains that would result from sensing the internally transmitted field, rather than the field external to the shell. This advantage ratio is shown always to be greater than unity, and in many cases, much greater than unity. The effects of two basically different types of loads are analyzed via the isobaric plots, and also by means of spectral plots computed at several fixed points inside the shell. The effect of the monopole ($n=0$) mode of vibration on the internal pressure field is analyzed in detail. We study its spectral characteristics at fixed internal points, and its radial dependence at various

frequencies. We observe an encouraging overall permanence of the caustic locations, at fixed frequencies, as the types of surface loads are varied. The present investigation of sound transmission into arbitrarily loaded shells clearly demonstrates the filtering behavior of the shell in the frequency domain, and its focusing action in space. Hence, for moderate surface loads, the air-filled submerged shell analyzed here acts as a very effective sound concentrator, particularly near the resonances of its monopole mode.

We have carried on a detailed computational study in the final sections of this report to quantitatively determine the effect of shell thickness, stiffness, and general material composition, on the sound fields transmitted into the loaded shells. This analysis makes the work valid for various metals and for shell relative-thickness between 1 percent and 20 percent, which is a range covering most practical cases. This final section shows that for all thicknesses and compositions, the large values of the advantage ratio P_R , still show large gains in sensing internal rather than external fields in all cases considered, provided the forcing (flow) function is below acceptable bounds.

FOREWORD

This report presents a detailed analytical and computational study of the sound transmission process that takes place when an elastic cylindrical shell submerged in water is subjected to the double excitation caused by an incident acoustic wave and by the action of surface forcing functions, of various essentially different types, applied along the periphery of the shell. We constructed a novel analytic methodology to evaluate the sound pressure fields inside the shell caused by all possible combinations of insonification and surface excitation conditions. This methodology is used to compute an advantage ratio P_R which measures the gains that would result from sensing internally-transmitted fields, rather than fields external to the shell.

This work was partly supported by Code 432 of the Office of Naval Research and partly by the Independent Research Board of the Naval Surface Weapons Center during FY83 and FY84.

Approved by:



IRA M. BLATSTEIN, Head
Radiation Division

CONTENTS

<u>Section</u>	<u>Page</u>
1 INTRODUCTION.....	1
2 THEORETICAL BACKGROUND.....	3
3 SUPERPOSITION PROPERTIES OF THE LOADED SHELL SOLUTION.....	11
4 NUMERICAL RESULTS.....	17
5 SHELL-THICKNESS AND MATERIAL COMPOSITION EFFECTS.....	33
6 CONCLUSIONS.....	41
REFERENCES.....	93
APPENDIX A-- NON-VANISHING ELEMENTS OF THE MATRICES.....	A-1
DISTRIBUTION.....	(1)

FOREWORD

This report presents a detailed analytical and computational study of the sound transmission process that takes place when an elastic cylindrical shell submerged in water is subjected to the double excitation caused by an incident acoustic wave and by the action of surface forcing functions, of various essentially different types, applied along the periphery of the shell. We constructed a novel analytic methodology to evaluate the sound pressure fields inside the shell caused by all possible combinations of insonification and surface excitation conditions. This methodology is used to compute an advantage ratio P_R which measures the gains that would result from sensing internally-transmitted fields, rather than fields external to the shell.

This work was partly supported by Code 432 of the Office of Naval Research and partly by the Independent Research Board of the Naval Surface Weapons Center during FY83 and FY84.

Approved by:



IRA M. BLATSTEIN, Head
Radiation Division

CONTENTS

<u>Section</u>	<u>Page</u>
1 INTRODUCTION.....	1
2 THEORETICAL BACKGROUND.....	3
3 SUPERPOSITION PROPERTIES OF THE LOADED SHELL SOLUTION.....	11
4 NUMERICAL RESULTS.....	17
5 SHELL-THICKNESS AND MATERIAL COMPOSITION EFFECTS.....	33
6 CONCLUSIONS.....	41
REFERENCES.....	93
APPENDIX A-- NON-VANISHING ELEMENTS OF THE MATRICES.....	A-1
DISTRIBUTION.....	(1)

ILLUSTRATIONS

<u>Figure</u>		<u>Page</u>
1	THE CYLINDRICAL SHELL, WITH LOAD #1 ACTING ON ITS ENTIRE OUTER SURFACE, AS IT INTERACTS WITH THE INCIDENT SOUND WAVE OF AMPLITUDE p_0	47
2	THE CYLINDRICAL SHELL WITH LOAD #2 ACTING ON PORTION OF ITS OUTER SURFACE. THE INCIDENT SOUND WAVE TRAVELS FROM LEFT TO RIGHT AND IT IS TRANSMITTED INTO THE LOADED SHELL'S INTERIOR .	48
3	INTERNALLY TRANSMITTED ISOBARIC CONTOUR PLOTS OF AN UNLOADED STEEL CYLINDRICAL SHELL INTERACTING WITH A PLANE MONOCHROMATIC INCIDENT SOUND WAVE OF AMPLITUDE p_0 , FOR FOUR VALUES OF k_3a ($= 1, 3, 5$ AND 10)	49
4	INTERNALLY TRANSMITTED ISOBARIC CONTOUR PLOTS OF AN AIR-FILLED CYLINDRICAL STEEL SHELL, LOADED WITH LOAD #1, WHICH INTERACTS WITH A PLANE INCIDENT ACOUSTIC WAVE AT FREQUENCIES SUCH THAT $k_3a = 1, 3, 5$ AND 10	50
5	INTERNALLY TRANSMITTED ISOBARIC CONTOUR PLOTS FOR AN AIR-FILLED CYLINDRICAL SHELL IN WATER LOADED WITH LOAD #2, WHICH INTERACTS WITH A PLANE INCIDENT SOUND WAVE AT FREQUENCIES SUCH THAT $k_3a = 3, 5$ AND 10	51
6	INTERNALLY TRANSMITTED ISOBARIC CONTOUR PLOTS FOR A SUBMERGED, AIR-FILLED, CYLINDRICAL SHELL, LOADED WITH LOAD #1 (UPPER PLOT), OR WITH LOAD #2 (LOWER PLOT), BOTH FOR $k_3a = 5$. NO INCIDENT WAVE INTERACTS WITH THE SHELL HERE	52
7a	INTERIOR PRESSURE LEVELS, $ p_3/p_0 $, VERSUS k_3a , AT FIVE (OF ELEVEN) LOCATIONS INSIDE AN UNLOADED CYLINDRICAL SHELL IN WATER INSONIFIED BY AN INCIDENT PLANE WAVE	53
7b	INTERIOR PRESSURE LEVELS, $ p_3/p_0 $, VERSUS k_3a , AT SIX ADDITIONAL (OF ELEVEN) POINTS INSIDE AN UNLOADED SHELL IN WATER INSONIFIED BY AN INCIDENT PLANE WAVE.	54
8a	INTERIOR PRESSURE LEVELS, $ p_3/p_0 $, VERSUS k_3a , AT FIVE (OF ELEVEN) POINTS INSIDE A SUBMERGED CYLINDRICAL SHELL LOADED WITH LOAD #1, AND INSONIFIED BY AN INCIDENT PLANE WAVE	55

ILLUSTRATIONS (CONT.)

<u>Figure</u>		<u>Page</u>
8b	INTERIOR PRESSURE LEVELS, $ p_3/p_0 $, VERSUS k_3a , AT FIVE (OF ELEVEN) POINTS INSIDE A SUBMERGED CYLINDRICAL SHELL LOADED WITH LOAD #1, AND INSONIFIED BY AN INCIDENT PLANE WAVE	56
9a	INTERIOR PRESSURE LEVELS p_3/p_0 VERSUS k_3a AT SIX (OF ELEVEN) POINTS INSIDE A SUBMERGED CYLINDRICAL SHELL, LOADED WITH LOAD #2, AND INSONIFIED BY AN INCIDENT PLANE WAVE	57
9b	INTERIOR PRESSURE LEVELS p_3/p_0 VERSUS k_3a AT SIX (OF ELEVEN) POINTS INSIDE A SUBMERGED CYLINDRICAL SHELL, LOADED WITH LOAD #2, AND INSONIFIED BY AN INCIDENT PLANE WAVE	58
10	INTERIOR SPL, $ p_3/p_0 $, VERSUS k_3a , COMPUTED AT SIX RADIAL LOCATIONS INSIDE AN UNLOADED CYLINDRICAL SHELL, FOR ITS MONOPOLE ($n = 0$) MODE	59
11	INTERIOR SPL, $ p_3/p_0 $, VERSUS k_3a , COMPUTED AT SIX RADIAL LOCATIONS INSIDE A CYLINDRICAL SHELL LOADED WITH LOAD #1, FOR ITS MONOPOLE ($n = 0$) MODE.	60
12	INTERIOR SPL, $ p_3/p_0 $, VERSUS k_3a , AT FIVE RADIAL LOCATIONS INSIDE A CYLINDRICAL SHELL LOADED WITH LOAD #2, FOR ITS MONOPOLE ($n = 0$) MODE.	61
13	RADIAL DEPENDENCE OF THE INTERNAL SPL, $ p_3/p_0 $, FOR THE MONOPOLE ($n = 0$) MODE OF AN UNLOADED CYLINDRICAL SHELL AT FOUR FREQUENCIES SUCH THAT $k_3a = 1, 3, 5$ AND 10	62
14	RADIAL DEPENDENCE OF THE INTERNAL SPL, $ p_3/p_0 $, FOR THE MONOPOLE ($n = 0$) MODE OF A CYLINDRICAL SHELL LOADED WITH LOAD #1, AT FOUR FREQUENCIES SUCH THAT $k_3a = 1, 3, 5$ AND 10	63
15	RADIAL DEPENDENCE OF THE INTERNAL SPL, $ p_3/p_0 $, FOR THE MONOPOLE ($n = 0$) MODE OF A CYLINDRICAL SHELL LOADED WITH LOAD #2, AT FOUR FREQUENCIES SUCH THAT $k_3a = 1, 3, 5$ AND 10	64
16	ISOBARIC CONTOUR PLOTS FOR THE INTERNALLY TRANSMITTED SOUND PRESSURE LEVELS INSIDE AN UNLOADED STEEL SHELL IN WATER AT $k_3a=5$ FOR FOUR SHELL-THICKNESSES (i.e., $b/a=0.80, 0.85, 0.90$ AND 0.95). THE LOCATIONS OF THE CAUSTICS ARE DETERMINED	65
17	ISOBARIC CONTOUR PLOTS FOR THE INTERNALLY TRANSMITTED SOUND PRESSURE LEVELS INSIDE A STEEL SHELL IN WATER LOADED WITH LOAD #1 AT $k_3a=5$, FOR FOUR SHELL-THICKNESSES (i.e., $b/a=0.80, 0.85, 0.90$ AND 0.95).	66

ILLUSTRATIONS (CONT.)

<u>Figure</u>		<u>Page</u>
18	ISOBARIC CONTOUR PLOTS FOR THE INTERNALLY TRANSMITTED SOUND PRESSURE LEVELS INSIDE A STEEL SHELL IN WATER LOADED WITH LOAD #2 AT $k_3a=5$, FOR FOUR SHELL-THICKNESSES (i.e., $b/a=0.80, 0.85, 0.90$ AND 0.95)	67
19	ISOBARIC CONTOUR PLOTS FOR THE INTERNALLY TRANSMITTED SOUND PRESSURE LEVELS INSIDE AN UNLOADED STEEL SHELL IN WATER AT $k_3a=7.0$, FOR FOUR SHELL-THICKNESSES (i.e., $b/a=0.80, 0.85, 0.90$ AND 0.95). THE LOCATIONS OF THE CAUSTICS ARE DETERMINED	68
20	ISOBARIC CONTOUR PLOTS FOR THE INTERNALLY TRANSMITTED SOUND PRESSURE LEVELS INSIDE A STEEL SHELL IN WATER LOADED WITH LOAD #1 AT $k_3a=7.0$, FOR FOUR SHELL-THICKNESSES (i.e., $b/a=0.80, 0.85, 0.90$ AND 0.95)	69
21	ISOBARIC CONTOUR PLOTS FOR THE INTERNALLY TRANSMITTED SOUND PRESSURE LEVELS INSIDE A STEEL SHELL IN WATER LOADED WITH LOAD #2 AT $k_3a=7.0$, FOR FOUR SHELL-THICKNESSES (i.e., $b/a=0.80, 0.85, 0.90$ AND 0.95)	70
22	ISOBARIC CONTOUR PLOTS FOR THE INTERNALLY TRANSMITTED SOUND PRESSURE LEVELS INSIDE AN UNLOADED ALUMINUM SHELL IN WATER AT $k_3a=5$, FOR FOUR SHELL-THICKNESSES (i.e., $b/a=0.80, 0.85, 0.90$ AND 0.95). THE LOCATIONS OF THE CAUSTICS ARE DETERMINED	71
23	ISOBARIC CONTOUR PLOTS FOR THE INTERNALLY TRANSMITTED SOUND PRESSURE LEVELS INSIDE AN ALUMINUM SHELL IN WATER LOADED WITH LOAD #1 AT $k_3a=5$, FOR FOUR SHELL-THICKNESSES (i.e., $b/a=0.80, 0.85, 0.90$ AND 0.95)	72
24	ISOBARIC CONTOUR PLOTS FOR THE INTERNALLY TRANSMITTED SOUND PRESSURE LEVELS INSIDE AN ALUMINUM SHELL IN WATER LOADED WITH LOAD #2 AT $k_3a=5$, FOR FOUR SHELL-THICKNESSES (i.e., $b/a=0.80, 0.85, 0.90$ AND 0.95)	73
25	ISOBARIC CONTOUR PLOTS FOR THE INTERNALLY TRANSMITTED SOUND PRESSURE LEVELS INSIDE AN UNLOADED ALUMINUM SHELL IN WATER AT $k_3a=7.0$, FOR FOUR SHELL-THICKNESSES (i.e., $b/a=0.80, 0.85, 0.90$ AND 0.95). THE LOCATIONS OF THE CAUSTICS ARE DETERMINED	74
26	ISOBARIC CONTOUR PLOTS FOR THE INTERNALLY TRANSMITTED SOUND PRESSURE LEVELS INSIDE AN ALUMINUM SHELL IN WATER LOADED WITH LOAD #1 AT $k_3a=7.0$, FOR FOUR SHELL-THICKNESSES (i.e., $b/a=0.80, 0.85, 0.90$ AND 0.95)	75

ILLUSTRATIONS (CONT.)

<u>Figure</u>		<u>Page</u>
27	ISOBARIC CONTOUR PLOTS FOR THE INTERNALLY TRANSMITTED SOUND PRESSURE LEVELS INSIDE AN ALUMINUM SHELL IN WATER LOADED WITH LOAD #2 AT $k_3a=7.0$, FOR FOUR SHELL-THICKNESSES (i.e., $b/a=0.80$, 0.85 , 0.90 AND 0.95).	76
28	INTERNALLY TRANSMITTED ISOBARIC CONTOUR PLOTS FOR A SUBMERGED, AIR-FILLED STEEL CYLINDRICAL SHELL IN WATER. THE SYMMETRIC LOAD #1 IS ACTING ON THE OUTER SURFACE OF THE SHELL. NO INCIDENT WAVE IS PRESENT HERE. FOUR SHELL-THICKNESSES ARE DISPLAYED HERE: $b/a=0.80$, 0.85 , 0.90 , AND 0.95 . ALL CALCULATIONS ARE DONE FOR $k_3a=5.0$. THIS IS THE EFFECT OF THE SURFACE LOAD ALONE AS GIVEN IN EQUATIONS (30) AND (26)	77
29	INTERNALLY TRANSMITTED ISOBARIC CONTOUR PLOTS FOR A SUBMERGED, AIR-FILLED STEEL CYLINDRICAL SHELL IN WATER. THE ASYMMETRIC LOAD #2 IS ACTING ON THE <u>STEEL SHELL</u> . NO INCIDENT WAVE IS PRESENT HERE. FOUR SHELL-THICKNESSES ARE DISPLAYED HERE: $b/a=0.80$, 0.85 , 0.90 , AND 0.95 . ALL CALCULATIONS ARE DONE FOR $k_3a=5.0$. THIS IS THE EFFECT OF THE SURFACE LOAD ALONE AS GIVEN IN EQUATIONS (30) AND (26)	78
30	INTERNALLY TRANSMITTED ISOBARIC CONTOUR PLOTS FOR A SUBMERGED, AIR-FILLED ALUMINUM SHELL EXTERNALLY EXCITED BY LOAD #1, AT $k_3a=5.0$. NO INCIDENT WAVE IS PRESENT HERE. FOUR SHELL THICKNESSES ARE DISPLAYED HERE: $b/a=0.80$, 0.85 , 0.90 AND 0.95 . THIS IS THE EFFECT OF THE SURFACE LOAD ALONE AS GIVEN IN EQUATIONS (30) AND (26)	79
31	INTERNALLY TRANSMITTED ISOBARIC CONTOUR PLOTS FOR A SUBMERGED, AIR-FILLED ALUMINUM SHELL EXTERNALLY EXCITED BY LOAD #2, AT $k_3a=5.0$. NO INCIDENT WAVE IS PRESENT HERE. FOUR SHELL-THICKNESSES ARE DISPLAYED HERE: $b/a=0.80$, 0.85 , 0.90 AND 0.95 . THIS IS THE EFFECT ON THE SURFACE LOAD ALONE AS GIVEN IN EQUATIONS (30) AND (26)	80
32	INTERIOR PRESSURE LEVELS $ p_3/p_0 $ AT SEVEN POINTS INSIDE AN UNLOADED STEEL SHELL IN WATER INSONIFIED BY A PLANE WAVE, VS. k_3a . THE RELATIVE SHELL-THICKNESS IS $b/a=0.80$	81
33	INTERIOR PRESSURE LEVELS $ p_3/p_0 $ AT SEVEN POINTS INSIDE AN UNLOADED STEEL SHELL IN WATER INSONIFIED BY A PLANE WAVE, VS. k_3a . THE RELATIVE SHELL-THICKNESS IS $b/a=0.85$	82
34	INTERIOR PRESSURE LEVELS $ p_3/p_0 $ AT SEVEN POINTS INSIDE AN UNLOADED STEEL SHELL IN WATER INSONIFIED BY A PLANE WAVE, VS. k_3a . THE RELATIVE SHELL-THICKNESS IS $b/a=0.90$	83

ILLUSTRATIONS (CONT.)

<u>Figure</u>	<u>Page</u>
35	INTERIOR PRESSURE LEVELS $ p_3/p_0 $ AT SEVEN POINTS INSIDE AN UNLOADED STEEL SHELL IN WATER INSONIFIED BY A PLANE WAVE, VS. k_3a . THE RELATIVE SHELL-THICKNESS IS $b/a=0.95$ 84
36	INTERIOR PRESSURE LEVELS $ p_3/p_0 $ AT SEVEN POINTS INSIDE A STEEL SHELL IN WATER LOADED WITH LOAD #1, AND INSONIFIED BY A PLANE WAVE, VS. k_3a . THE RELATIVE SHELL-THICKNESS IS $b/a=0.80$. 85
37	INTERIOR PRESSURE LEVELS $ p_3/p_0 $ AT SEVEN POINTS INSIDE A STEEL SHELL IN WATER LOADED WITH LOAD #1, AND INSONIFIED BY A PLANE WAVE, VS. k_3a . THE RELATIVE SHELL-THICKNESS IS $b/a=0.85$. 86
38	INTERIOR PRESSURE LEVELS $ p_3/p_0 $ AT SEVEN POINTS INSIDE A STEEL SHELL IN WATER LOADED WITH LOAD #1, AND INSONIFIED BY A PLANE WAVE VS. k_3a . THE RELATIVE SHELL-THICKNESS IS $b/a=0.90$. . 87
39	INTERIOR PRESSURE LEVELS $ p_3/p_0 $ AT SEVEN POINTS INSIDE A STEEL SHELL IN WATER LOADED WITH LOAD #1, AND INSONIFIED BY A PLANE WAVE VS. k_3a . THE RELATIVE SHELL-THICKNESS IS $b/a=0.95$. . 88
40	INTERNAL PRESSURE LEVELS $ p_3/p_0 $ AT SEVEN POINTS INSIDE A STEEL SHELL IN WATER LOADED WITH LOAD #2, AND INSONIFIED BY A PLANE WAVE, VS. k_3a . THE RELATIVE SHELL-THICKNESS IS $b/a=0.80$. 89
41	INTERNAL PRESSURE LEVELS $ p_3/p_0 $ AT SEVEN POINTS INSIDE A STEEL SHELL IN WATER LOADED WITH LOAD #2, AND INSONIFIED BY A PLANE WAVE VS. k_3a . THE RELATIVE SHELL-THICKNESS IS $b/a=0.85$. . 90
42	INTERNAL PRESSURE LEVELS $ p_3/p_0 $ AT SEVEN POINTS INSIDE A STEEL SHELL IN WATER LOADED WITH LOAD #2, AND INSONIFIED BY A PLANE WAVE VS. k_3a . THE RELATIVE SHELL-THICKNESS IS $b/a=0.90$. . 91
43	INTERNAL PRESSURE LEVELS $ p_3/p_0 $ AT SEVEN POINTS INSIDE A STEEL SHELL IN WATER LOADED WITH LOAD #2, AND INSONIFIED BY A PLANE WAVE VS. k_3a . THE RELATIVE SHELL-THICKNESS IS $b/a=0.95$. . 92

TABLES

<u>Table</u>		<u>Page</u>
1	VALUES OF P_R (EQUATION (31)) FOR $k_3a = 5$	23
2	VALUES OF P_R FOR VARIOUS SHELL-THICKNESSES AND COMPOSITIONS.	37

SECTION 1
INTRODUCTION

The scattering of sound waves incident on cylindrical elastic shells has traditionally been studied in the outer fluid surrounding the shells, particularly at far away distances. This is a consequence of the fact that this is the operating region of most sensing devices. The literature on this type of sound/structure interaction problems is quite voluminous¹⁻¹² and it is not possible to cover it extensively here. Some authors have treated a single bare shell.^{1,7,9} Others have studied layered concentric shells,^{5,6,8} either all elastic¹¹ or some elastic and some viscoelastic.^{6,10} Some have described the shell(s) motions by the exact equations of linear two-dimensional elastodynamics (viscoelastodynamics) while others have described the shell responses by means of the equations of some approximate shell theory.^{2,3} Some have considered the same fluid inside and outside the shell,⁷ while others have studied the shell separating dissimilar fluids.^{5,12} Sometimes the analysis has focused on techniques for the low-frequency response⁷ while other authors have emphasized methods particularly useful at high frequencies.^{1,6} Some studies have shown connections between the scattering and the radiation of sound. In most cases¹⁻¹² the incident waves are considered plane as they would be if they emerged from a distant transducer, although some isolated cases of spherical wave incidences have been treated.¹³⁻¹⁵ For incident plane waves, almost all the literature has dealt with the scattered waveforms in the outer medium, far away from the shell. We know of hardly any studies of

backscattered near-fields. In all cases that we have ever encountered, the shells are usually immersed in fluids, but are otherwise unloaded.

In the present paper we will study the transmission of sound energy into the fluid medium inside a single, elastic, and loaded cylindrical shell submerged in a dissimilar fluid. We are not aware of any published work on these aspects of the interaction. The incident acoustic wave is plane and it sets the shell into vibration as it falls upon it. The shell is free to translate by radiation pressure as the wave hits it. The shell is of a great length, and the incidence is at broadside aspects. In this common two-dimensional situation, the shell motions are governed by the corresponding z-independent equations of linear elastodynamics. The shell is not only excited by the incident plane harmonic wave, but it is also subjected to an arbitrary loading on its outer surface caused perhaps (although the cause is not important here) by a relative motion of the outer fluid past the shell. So, the shell is not only hydrostatically fluid-loaded by the simple fact that it is submerged in a fluid, but also because there is an externally-generated arbitrary load acting on its outer surface. We wish to systematically study the internal sound fields developed inside the shell as a result of the double action of the incident plane wave of amplitude p_0 and of the arbitrary surface load of amplitude p_2 . It becomes immediately obvious that the innumerable modal shell resonances that are excited by this double action, will induce various caustics in the internally transmitted sound pressure fields, and that at these selected points, the internal pressures could be very pronounced. We will see how these intuitive empiricisms actually emerge and are substantiated by the following model and its analytic predictions.

SECTION 2
THEORETICAL BACKGROUND

The theory has already been developed for bare and coated but unloaded cylindrical shells.^{1,5} We briefly outline the basics⁵ for completeness.

Navier equations for the (infinite) cylindrical geometry are

$$\begin{cases} \nabla_{r\theta}^2 u_r - \frac{u_r}{r} - \frac{2}{r} \frac{\partial u_\theta}{\partial \theta} + \frac{\lambda + \mu}{\mu} \frac{\partial \Delta}{\partial r} + k_s^2 u_r = 0 \\ \nabla_{r\theta}^2 u_\theta - \frac{u_\theta}{r} + \frac{2}{r} \frac{\partial u_r}{\partial \theta} + \frac{\lambda + \mu}{\mu} \frac{1}{r} \frac{\partial \Delta}{\partial \theta} + k_s^2 u_\theta = 0 \end{cases} \quad (1)$$

where the Laplacian and the dilatation are, respectively,

$$\nabla_{r\theta}^2 = \frac{\partial^2}{\partial r^2} + \frac{1}{r} \frac{\partial}{\partial r} + \frac{1}{r^2} \frac{\partial^2}{\partial \theta^2}, \quad (2a)$$

$$\Delta = \frac{\partial u_r}{\partial r} + \frac{1}{r} \frac{\partial u_\theta}{\partial \theta} + \frac{u_r}{r}, \quad (2b)$$

where $k_s^2 = \rho\omega^2/\mu$, $k_d^2 = \rho\omega^2/(\lambda + 2\mu)$, and where time-dependence of the form $\exp(-i\omega t)$ has been assumed throughout.

We have shown earlier¹⁶ that Equations (1) are automatically satisfied if two scalar potentials are introduced which satisfy the two scalar Helmholtz equations

$$(\nabla_{r\theta}^2 + k_d^2)\phi = 0, \quad (\nabla_{r\theta}^2 + k_s^2)\psi_z = 0. \quad (3)$$

All the relevant displacement and stress components can be obtained from ϕ and ψ_z by means of the following formulas:¹⁶

$$\begin{cases} u_r = \frac{\partial \phi}{\partial r} + \frac{1}{r} \frac{\partial \psi_z}{\partial \theta} \\ u_\theta = \frac{1}{r} \frac{\partial \phi}{\partial \theta} - \frac{\partial \psi_z}{\partial r} \end{cases} \quad (4)$$

$$\begin{cases} \tau_{rr} = -\lambda k_d^2 \phi + 2\mu \left[\frac{\partial^2 \phi}{\partial r^2} + \frac{\partial}{\partial r} \left(\frac{1}{r} \frac{\partial \psi_z}{\partial \theta} \right) \right] \\ \tau_{r\theta} = \mu \left[2 \frac{\partial^2}{\partial r \partial \theta} \left(\frac{\phi}{r} \right) - \left(\frac{\partial^2 \psi_z}{\partial r^2} - \frac{1}{r} \frac{\partial \psi_z}{\partial r} - \frac{1}{r^2} \frac{\partial^2 \psi_z}{\partial \theta^2} \right) \right] \end{cases} \quad (5)$$

Solving the uncoupled Equations (3) subject to suitable boundary conditions, which are set-up by means of Equations (4) and (5), one is really solving the coupled Equations (1). Once the fully determined ϕ and ψ_z are found, then the same Equations (4) and (5) yield the displacement and stress fields everywhere.

NORMAL MODE SOLUTION FOR THE UNLOADED SHELL

This solution can be obtained, for an unloaded shell, from earlier published work.⁵ In the three media one has,

$$p_1(r, \theta, t) = p_0 e^{-i\omega t} \sum_{n=0}^{\infty} i^n \epsilon_n [J_n(k_1 r) + b_n H_n^{(1)}(k_1 r)] \cos n\theta \quad (6)$$

for the outer fluid (medium 1), together with

$$u_r^{(1)} = \frac{1}{\rho_1 \omega} \frac{\partial p_1}{\partial r} \quad (7)$$

In the shell material (medium 2), the elastic potentials are

$$\begin{cases} \phi_2 = p_0 e^{-i\omega t} \sum_{n=0}^{\infty} i^n \epsilon_n [g_n J_n(k_{d_2} r) + h_n Y_n(k_{d_2} r)] \cos n\theta \\ \psi_{z_2} = p_0 \bar{e}^{i\omega t} \sum_{n=0}^{\infty} i^n \epsilon_n [\ell_n J_n(k_{s_2} r) + m_n Y_n(k_{s_2} r)] \sin n\theta, \end{cases} \quad (8)$$

where $k_{d_2} = \omega/c_{d_2}$ and $k_{s_2} = \omega/c_{s_2}$. Finally, the pressure in the inner fluid (medium 3) is

$$p_3(r, \theta, t) = p_0 e^{-i\omega t} \sum_{n=0}^{\infty} i^n \epsilon_n q_n J_n(k_3 r) \cos n\theta, \quad (9)$$

where $k_3 = \omega/c_3$ and the six sets of constants b_n , g_n , h_n , ℓ_n , m_n , and q_n are determined from the boundary conditions, which for the unloaded shell are,

$$\begin{cases} \tau_{rr}^{(2)}|_{r=a} = -p_1|_{r=a}, \quad u_r^{(1)}|_{r=a} = u_r^{(2)}|_{r=a}, \quad \tau_{r\theta}^{(2)} = 0, \\ \tau_{rr}^{(2)}|_{r=b} = -p_3|_{r=b}, \quad u_r^{(2)}|_{r=b} = u_r^{(3)}|_{r=b}, \quad \tau_{r\theta}^{(2)} = 0. \end{cases} \quad (10)$$

and where the Neumann symbol is $\epsilon_n = 2 - \delta_{n0}$. We will treat the case of the loaded shell later. Substituting Equations (6)-(9) into (10) yields the following vector/matrix linear relation

$$D\vec{x}_n = \vec{A}_n^*, \quad (11)$$

where $\vec{x}_n = (b_n, g_n, h_n, \ell_n, m_n, q_n)^T$ and $\vec{A}_n^* = (A_1^*, A_2^*, 0, 0, 0, 0)^T$, and

D is a 6 x 6 matrix that can be easily obtained from the 10 x 10 matrix found earlier⁵ for coated shells. The result is,

$$D_n = \begin{vmatrix} d_{11} & d_{12} & d_{13} & d_{14} & d_{15} & 0 \\ d_{21} & d_{22} & d_{23} & d_{24} & d_{25} & 0 \\ 0 & d_{32} & d_{33} & d_{34} & d_{35} & 0 \\ 0 & d_{86} & d_{87} & d_{88} & d_{89} & d_{8,10} \\ 0 & d_{96} & d_{97} & d_{98} & d_{99} & d_{9,10} \\ 0 & d_{10,6} & d_{10,7} & d_{10,8} & d_{10,9} & 0 \end{vmatrix} \quad (12)$$

where these elements are all listed before.^{5,8} We could relabel them as follows:

$$D_n = \begin{vmatrix} d_{11} & d_{12} & d_{13} & d_{14} & d_{15} & 0 \\ d_{21} & d_{22} & d_{23} & d_{24} & d_{25} & 0 \\ 0 & d_{32} & d_{33} & d_{34} & d_{35} & 0 \\ 0 & d_{42} & d_{43} & d_{44} & d_{45} & d_{46} \\ 0 & d_{52} & d_{53} & d_{54} & d_{55} & d_{56} \\ 0 & d_{62} & d_{63} & d_{64} & d_{65} & 0 \end{vmatrix} \quad (12')$$

so that the indices run from 1 to 6, as they should in this (uncoated) case. Equation (11) can be solved for any of the six sets of constants it contains, by Cramer's rule. For example, the set of constants q_n is given by the quotient

$$q_n = \frac{Q_n}{D_n}, \quad (13)$$

where D_n is as above, and Q_n is like D_n but with its sixth column replaced by the column vector \hat{A}_n^* , i.e.,

$$q_n = (1/D_n) \begin{vmatrix} d_{11} & d_{12} & d_{13} & d_{14} & d_{15} & A_1^* \\ d_{21} & d_{22} & d_{23} & d_{24} & d_{25} & A_2^* \\ 0 & d_{32} & d_{33} & d_{34} & d_{35} & 0 \\ 0 & d_{42} & d_{43} & d_{44} & d_{45} & 0 \\ 0 & d_{52} & d_{53} & d_{54} & d_{55} & 0 \\ 0 & d_{62} & d_{63} & d_{64} & d_{65} & 0 \end{vmatrix} \quad (14)$$

which completes the solution. The 30 different elements contained in the numerator and denominator of this equation are listed in Appendix A to make this work self-contained, although they could be obtained with relative ease from our earlier work.^{5,8} Finally, it follows from Equation (9) that

$$p_0 = \left| \frac{p_3}{p_0} \right| = \left| \sum_{n=0}^{\infty} i^n \epsilon_n q_n J_n(k_3 r) \cos n\theta \right|. \quad (14')$$

THE LOADED SHELL CASE

If the outer surface (i.e., $r = a$) of the shell is additionally loaded with a spatially varying (i.e., θ - dependent) excitation $p_L(a, \theta, t)$, then the normal-mode solution given above continues to hold, but now the first of the boundary conditions changes. The first boundary condition in this loaded case is

$$\tau_{rr}^{(2)} \Big|_{r=a} = - [p_1(r, \theta, t) + p_L(r, \theta, t)]_{r=a}, \quad (15)$$

where p_1 is still given by Equation (6) and p_L is the new, arbitrary surface load. Let this load be harmonic in time and spatially symmetric about the

direction $\theta = 0$ of the incident wave. The load is then an even function, and by means of a Fourier (cosine) transform we can write

$$p_L(a, \theta, t) = p_2 e^{-i\omega t} \sum_{n=0}^{\infty} i^n \epsilon_n \cos n\theta \left[\frac{1}{\pi} \int_0^{\pi} p_L(\theta) \cos n\theta d\theta \right], \quad (16)$$

where $p_2 (\neq p_0)$ is the amplitude of this load. We recall that the incident plane wave is given by the expansion,⁵

$$p_{inc}(r, \theta, t) = p_0 \exp [i(\vec{k}_1 \cdot \vec{r} - \omega t)] = p_0 e^{-i\omega t} \sum_{n=0}^{\infty} i^n \epsilon_n J_n(k_1 r) \cos n\theta. \quad (17)$$

In view of the fact that there is a new boundary condition at $r = a$, all the sets of constants (i. e., $\tilde{b}_n, \tilde{c}_n, \dots, \tilde{q}_n$) for this loaded case will be different from before, and that is why we have labeled them with tildes.

If we substitute the solutions into the boundary conditions to determine the new sets of constants, and we concentrate on the set \tilde{q}_n , it turns out that we find an expression very similar to that found for the unloaded case and that is why we introduced it earlier. The result now is

$$\tilde{q}_n = \frac{1}{D_n} \begin{vmatrix} d_{11} & d_{12} & d_{13} & d_{14} & d_{15} & \tilde{A}_1^* \\ d_{21} & d_{22} & d_{23} & d_{24} & d_{25} & A_2^* \\ 0 & d_{32} & d_{33} & d_{34} & d_{35} & 0 \\ 0 & d_{42} & d_{43} & d_{44} & d_{45} & 0 \\ 0 & d_{52} & d_{53} & d_{54} & d_{55} & 0 \\ 0 & d_{62} & d_{63} & d_{64} & d_{65} & 0 \end{vmatrix} \quad (18)$$

where D_n is still given in Equation (12') and the above determinant is almost identical to that in Equation (14), except for the element in its upper right corner which in Equation (14) was simply, (c/o Appendix A)

$$A_1^* = -(\rho_1/\rho_2)k_{s_2}^2 a^2 J_n(k_1 a) \quad (19)$$

while now in Equation (18), with the tilde, it takes the form

$$\tilde{A}_1^* = A_1^* + I_n = -(\rho_1/\rho_2)k_{s_2}^2 a^2 [J_n(k_1 a) + \frac{p_2}{p_0} \frac{1}{\pi} \int_0^\pi p_L(\theta) \cos n\theta d\theta]. \quad (20)$$

Clearly, the portion labeled I_n , containing the integral, is the portion that accounts for the surface loading p_L , which is now assumed of unit amplitude (see Figure 1) since its amplitude p_2 , normalized to p_0 has been taken out of the integral and placed in front of it as a factor.

For the internal sound pressure levels (SPL) inside the shell (i.e., medium 3), Equation (9) can be rewritten in normalized form as follows

$$\tilde{p} = \left| \frac{p_3}{p_0} \right| = \left| \sum_{n=0}^{\infty} \epsilon_n i^n \tilde{q}_n J_n(k_3 r) \cos n\theta \right|, \quad (21)$$

where \tilde{q}_n , for the loaded shell, is given in Equation (18) with \tilde{A}_1^* in Equation (20). This is the key result for the systematic study of the internal field of the loaded shell insonified by the incident plane wave. No shell theories have been introduced. The results are all exact under the conditions stated. Note that \tilde{q}_n is the only one of the new sets of constants that enters the series expression for the (normalized) pressure field inside the arbitrarily loaded shell. Most of the following sections will study various properties of

the solution given by Equations (21) and (20). Before the advent of the present computer age, it would have been unthinkable to evaluate formulas such as these. Note that coefficients \tilde{q}_n and q_n , from Equations (18) and (14), for the loaded and unloaded cases, respectively, contain all the necessary dependence on geometry, on material composition of the shell and of its surrounding fluids, and on the amplitudes of the incident wave and the surface load, as well as on the spatial distribution of the surface load. All these coefficients also depend on frequency and this general solution is valid for the entire frequency spectrum including its low, middle, and high regions. In view of the usual slow convergence of series solutions containing Bessel functions such as that in Equation (21), it may be computationally expensive and/or analytically unfeasible to carry on meaningful calculations beyond a value of k_3a of about 15 or 20. Beyond this value, the series must be conditioned via the Watson-Sommerfeld method⁶ or other similar techniques, not only to accelerate the series convergence, but to bring out the physics. At these high frequencies, the motivation for the present work on internal fields within shells loses its urgency and it will not be pursued here.

SECTION 3

SUPERPOSITION PROPERTIES OF THE LOADED SHELL SOLUTION

In view of the linearity of this problem we can study the effect of the incident monochromatic wave on the internally transmitted field separate from the effect of the surface load. From Equations (18) and (20) it follows that

$$\tilde{q}_n = q_n + \hat{q}_n \quad (22)$$

where \hat{q}_n is the coefficient associated with the unloaded shell excited only by the incident plane wave already given in Equation (14), and \hat{q}_n is a new coefficient given by the determinant ratio

$$\hat{q}_n = \frac{1}{D_n} \begin{vmatrix} d_{11} & d_{12} & d_{13} & d_{14} & d_{15} & I_n \\ d_{21} & d_{22} & d_{23} & d_{24} & d_{25} & 0 \\ 0 & d_{32} & d_{33} & d_{34} & d_{35} & 0 \\ 0 & d_{42} & d_{43} & d_{44} & d_{45} & 0 \\ 0 & d_{52} & d_{53} & d_{54} & d_{55} & 0 \\ 0 & d_{62} & d_{63} & d_{64} & d_{65} & 0 \end{vmatrix} \quad (23)$$

where

$$I_n = -\frac{\rho_1}{\rho_2} k_{s_2}^2 a^2 \left(\frac{\rho_2}{\rho_0}\right) \frac{1}{\pi} \int_0^\pi p_L(\theta) \cos n\theta d\theta. \quad (24)$$

This new nondimensional coefficient represents the contribution to the internally transmitted field caused by the (isolated) surface load in the absence of the incident wave. This contribution clearly vanishes for unloaded shells. The determinant D_n is still as given in Equation (12').

For ease of calculation, and in order to best be able to interpret the steps of the analysis that will follow in this section, we will rewrite Equation (22) in the form

$$\tilde{q}_n = q_n + \left(\frac{p_2}{p_0}\right) \hat{q}_n \quad (25)$$

where \hat{q}_n now is given by

$$\hat{q}_n = \frac{1}{D_n} \begin{vmatrix} d_{11} & d_{12} & d_{13} & d_{14} & d_{15} & \hat{I}_n \\ d_{21} & d_{22} & d_{23} & d_{24} & d_{25} & 0 \\ 0 & d_{32} & d_{33} & d_{34} & d_{35} & 0 \\ 0 & d_{42} & d_{43} & d_{44} & d_{45} & 0 \\ 0 & d_{52} & d_{53} & d_{54} & d_{55} & 0 \\ 0 & d_{62} & d_{63} & d_{64} & d_{65} & 0 \end{vmatrix} \quad (26)$$

and where

$$\hat{I}_n = -\frac{\rho_1}{\rho_2} k_{s_2}^2 a^2 \frac{1}{\pi} \int_0^\pi p_L(\theta) \cos n\theta d\theta. \quad (27)$$

We have simply explicitly pulled out the factor (p_2/p_0) from Equation (24). It is now possible to return to Equation (21) which gives the (normalized) internal sound-pressure level of the loaded shell, and analyze its two components given by Equation (25) separately. We define

$$p_o \equiv \left| \frac{p_3}{p_0} \right| \equiv \left| \sum_{n=0}^{\infty} \epsilon_n i^n q_n J_n(k_3 r) \cos n\theta \right|. \quad (28)$$

as the contribution to the SPL caused solely by the incident wave, and

$$\hat{p} \equiv \left| \frac{\hat{p}_3}{p_0} \right| \equiv \left| \sum_{n=0}^{\infty} \epsilon_n i^n \frac{p_2}{p_0} \hat{q}_n J_n(k_3 r) \cos n\theta \right| \quad (29)$$

as the contribution to the internal SPL solely due to the surface load.

Multiplication through by (p_0/p_2) yields,

$$\frac{p_0}{p_2} \hat{p} = \left| \frac{\hat{p}_3}{p_2} \right| = \left| \sum_{n=0}^{\infty} \epsilon_n i^n \hat{q}_n J_n(k_3 r) \cos n\theta \right|. \quad (30)$$

We now consider the ratio of the contributions of Equations (28) and (30) to the total internal SPL. This would be the ratio of the (duly normalized) contribution to the internally transmitted pressure field caused by the incident wave alone, to that of the contribution caused by the surface load alone. This resulting ratio P_R is,

$$P_R = \frac{|p_3/p_0|}{|\hat{p}_3/p_2|} = \frac{|p_3/\hat{p}_3|}{|p_0/p_2|} = \frac{\left| \sum_{n=0}^{\infty} \epsilon_n i^n q_n J_n(k_3 r) \cos n\theta \right|}{\left| \sum_{n=0}^{\infty} \epsilon_n i^n \hat{q}_n J_n(k_3 r) \cos n\theta \right|}. \quad (31)$$

This interesting result shows the ratio of the incident signal to surface-load amplitudes, when they are computed inside the shell (numerator) and outside the shell (denominator). Coefficients q_n , \hat{q}_n are given in Equations (14) and (26) respectively. If the surface load is to be viewed as some undesirable "noise" that corrupts the incident waveform, then the ratio P_R can be interpreted as the "signal-to-noise ratio" sensed after transmission into the shell, divided by the signal-to-noise ratio, sensed outside of it. If $P_R > 1$ it then follows that there would be an advantage in sensing these fields

internally rather than externally.

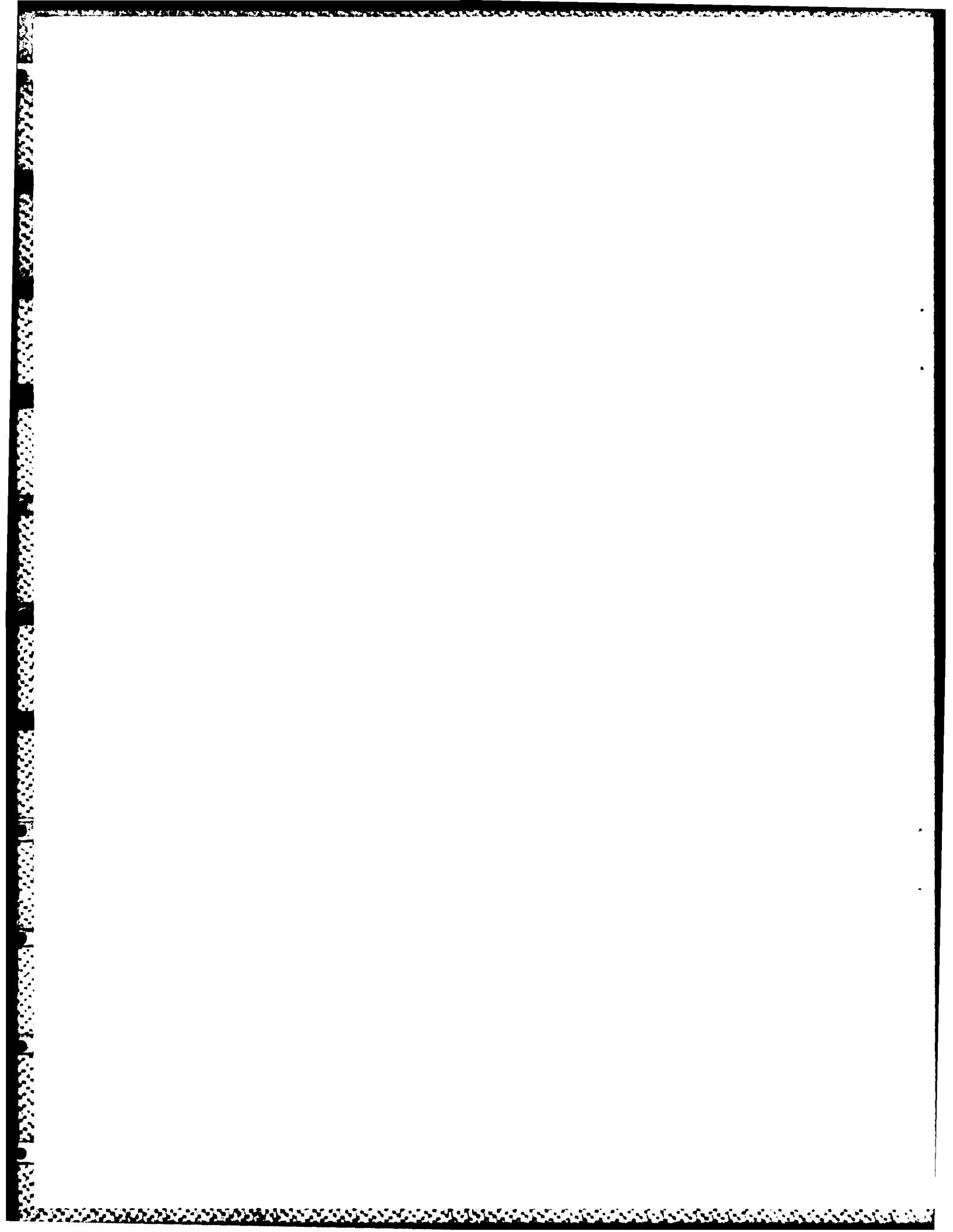
Finally, if we want to study the total internal pressure field containing the contributions from both incident signal and the arbitrary surface load, the result is that given in Equation (21), with \tilde{q}_n given by Equation (25). This normalized result is,

$$P_T = \left| \frac{p_3}{p_0} \right| = \left| \sum_{n=0}^{\infty} \epsilon_n i^n \left[q_n + \left(\frac{p_2}{p_0} \right) \hat{q}_n \right] J_n(k_3 r) \cos n\theta \right|, \quad (32)$$

where q_n and \hat{q}_n are respectively given in Equations (14) and (26). The result computed from this formula would not differ much from the analogous result for an unloaded shell given in Equation (28) if the effect of the surface load were negligible. This obvious criterion will serve to determine if a given surface load is negligible or not. We will see that there are some types of surface loads that affect just a couple of the shell's normal modes of vibration and, thus, have a relatively small disturbing effect on the pressure field transmitted into the shell as a result of the (dominant) incident-wave contribution. Other types of surface loads affect many, if not all, of the shell's normal modes of vibration and, therefore, have a pronounced distorting effect on the internal fields caused by the incident wave contribution.

Before showing numerical results for specific loads and geometries, we can make some general remarks based on physical intuition and common scientific sense. As the outer shell to sound wavelength-ratio (a/λ) is increased, a more and more complex sound field will be transmitted into the shell's interior and families of caustics will inevitably be developed internally. If we plot the internal isobars (i.e., the loci of points

exhibiting the same value of the internal sound pressure levels), we will indeed expect to see how these isobars group around certain points at which the isobar level becomes a local maximum. These points define the locations of the internal field's caustics. The higher the value of a/λ considered, the more caustics one is expected to see, and the more detailed and complex the isobaric contours of the internal sound field will be. These internal isobaric plots can be constructed at increasingly higher a/λ - values to observe the quantitative development of the internal field, as well as the caustic migrations for three cases: (1) when the surface load is acting on the insonified shell, (2) when it is not acting on the still insonified shell, and (3) when the surface load is present, but the shell is not being insonified by any incident wave. The interplay between these cases will serve to derive a variety of conclusions, most of them originally conceived on the basis of intuition and of our expectations for the shell behavior as a mechanical filter of acoustical energy.



SECTION 4
NUMERICAL RESULTS

The shell material is initially steel of properties: (1) density $\rho_2 = 7.84 \text{ g/cm}^3$, (2) dilatational wave-speed $c_{d_2} = 5.8 \times 10^5 \text{ cm/sec}$ and, (3) shear wave-speed $c_{s_2} = 3.1 \times 10^5 \text{ cm/sec}$. The shell is thin and the a/b ratio is initially $180/178 = 1.011235$, where a is the outer shell radius and b its inner radius. The shell is immersed in water at 20°C , of properties: $c_1 = 1.476 \times 10^5 \text{ cm/sec}$, and $\rho_1 = 1.0 \text{ g/cm}^3$. The inner fluid is air of properties: $c_3 = 0.344 \times 10^5 \text{ cm/sec}$, and $\rho_3 = 0.0012 \text{ g/cm}^3$. The water is medium 1, the shell is medium 2, and the air is medium 3.

We will consider two loads acting on the outer shell surface $r = a$. They are shown in Figures 1 and 2. Load #1, shown in Figure 1, is a wavy load that acts on the entire surface of the shell and is described by the relation:

$$p_L(\theta) = K \left(1 + \frac{1}{r} \cos s\theta \right), \quad (33)$$

where r and s are numerical parameters associated with the number of lobes in the pattern, and the maxima or minima levels of its amplitude K . In the above text we denoted the mean amplitude K by p_2 . The numerical values of r and s for this load are $r = 4$ and $s = 6$. Load #2, shown in Figure 2, is a sinusoidal type of load that acts on a relatively small portion of the shell's surface and has equation

$$p_L(\theta) = \begin{cases} 0 & \dots & 0 < \theta < \pi/3 \\ \sin(2\theta - \frac{2\pi}{3}) & \dots & \pi/3 < \theta < 5\pi/6 \\ 0 & \dots & 5\pi/6 < \theta < \pi \end{cases} \quad (34)$$

The amplitude of this load was said to be p_2 in the text, but here it is shown to be unity for reasons discussed before. Both these loads are symmetric with respect to the $\theta = 0$ direction, and admit Fourier cosine decompositions. The incident wave always hits these loaded shells from the left, along the $\theta = 0$ direction.

We now consider the Fourier integral appearing in Equation (24), viz,

$$\tilde{\gamma}_n = \frac{1}{\pi} \int_0^\pi p_L(\theta) \cos n\theta d\theta \quad (35)$$

and evaluate it for the two loads given in Equations (33) and (34) and shown in Figures 1 and 2. For load # 1 the result is,

$$\tilde{\gamma}_n = \frac{p_2}{\pi p_0} \int_0^\pi (1 + \frac{1}{4} \cos 6\theta) \cos n\theta d\theta = \begin{cases} p_2/p_0, & \dots & n = 0 \\ p_2/2rp_0, & \dots & n = (s) 6 \\ 0, & \dots & \text{any other } n. \end{cases} \quad (36)$$

Thus, for $r = 4$, and $s = 6$ the integral $\tilde{\gamma}_n$ has value p_2/p_0 for $n = 0$, $p_2/8p_0$ for $n = 6$, and vanishes for any other value of n . Clearly, this is the type of load that will affect only a couple of the shell's vibrational modes. Note that here, p_2/p_0 can be considered of unit value since the factor (p_2/p_0) was already taken out of the pertinent integrals, as shown in Equation (25). For load # 2 we must evaluate,

$$\tilde{\gamma}_n = \frac{1}{\pi} \left(\frac{p_2}{p_0}\right) \int_{\pi/3}^{5\pi/6} \sin(2\theta - 2\pi/3) \cos n\theta d\theta \quad (37)$$

and the result is

$$\tilde{\gamma}_n = \begin{cases} = -\frac{2 p_2}{\pi(4-n^2) p_0} \left[\cos \frac{5\pi n}{6} + \cos \frac{n\pi}{3} \right] & \forall n \neq 2 \\ = -\frac{\sqrt{3}}{8} \frac{p_2}{p_0} & \text{for } n = 2 \end{cases} \quad (38)$$

This is the type of load that will affect all the shell's modes of vibration. The values of \hat{I}_n , as given in Equation (27), are merely the above values of $\tilde{\gamma}_n$ in Equations (36) and (38), times the factor $-(\rho_1/\rho_2) k_{s_2}^2 a^2$. All the coefficients have now been evaluated, and we can proceed to display computed plots. We have developed computer codes^{5,6} that permit the evaluation of unloaded shell responses,⁸⁻¹⁰ viewed in the outer medium 1. We extended these codes to also compute the internally transmitted pressure fields into loaded shells as we have described it here. Additional codes were created to compute and graph the isobars (i.e., the loci of points exhibiting the same value of internal pressure) inside the shell, in various cases, and as function of all the problem parameters.

Figure 3 shows four successive stages of development of the internal isobaric fields inside the shell for arbitrary values of $k_3 a$ of 1, 3, 5, and 10. These patterns are computed for an unloaded steel shell using Equation (14') and (14). A point (r, θ) defines any location in medium 3, inside the shell. The allowable ranges are $0 < r < b$ and $0 < \theta < \pi$. The patterns are symmetric with respect to the centerline direction, $\theta = 0$. The incident wave of amplitude p_0 always hits the shell from the left. As we anticipated, the internal fields become more and more developed and complex as the $k_3 a$ -value is increased. (Note: $k_3 = \omega/c_3 = 2\pi f/c_3$, and c_3 is the sound speed in air). For $k_3 a = 10$ the pattern has already about eight noticeable caustics, while at $k_3 a = 5$, there are two noticeable ones on the centerline, at polar

coordinates of (0.3 , 0°) and (0.4, 180°). The radial coordinates have been nondimensionalized to r/b . The artificial irregularities in the computed patterns near their outer edges are numerically caused by the size of the step that separates consecutive isobars within each plot.

Figure 4 shows the same four isobaric contour plots inside the same shell, at the same values $k_3a = 1, 3, 5$ and 10 , now computed for a shell loaded with Load #1 (see Figure 1). The lower-frequency plots (i.e., $k_3a = 1$ and 3) are not too informative since hardly any caustic has had a chance to develop yet, but for $k_3a = 5$, and 10 we already see a fully developed isobaric set of contours not very different from those in Figure 3 for an unloaded shell at the same k_3a -values. For $k_3a = 5$, the same two caustics are observed at the centerline, at about the same places. The similarity between these plots and those for the unloaded shell in Figure 3 is undoubtedly due to the fact that Load #1 is a type of load that affects only a couple of the shell's vibrational modes and thus, it produces no overwhelming distortion of the pattern already present in the unloaded shell case. The plots are computed from Equation (21) with \tilde{q}_n as in Equation (18), and the integral within coefficient \tilde{A}_1^* as in Equation (36); in other words,

$$\tilde{A}_1^* = -\frac{\rho_1}{\rho_2} k_{s_2}^2 a^2 [J_n(k_1 a) + \left(\frac{\rho_2}{\rho_0}\right) * \begin{bmatrix} 1 \\ 1/8 \\ 0 \end{bmatrix}] \quad \begin{array}{l} \dots \text{for } n = 0 \\ \dots \text{for } n=6 \\ \dots \text{for any other } n. \end{array} \quad (39)$$

and where, in addition, we have assumed $\rho_2/\rho_0 = 1$ to generate the plots. This assumption was introduced to show that even when the amplitude of the surface load ρ_2 is comparable to that of the incident wave ρ_0 , its effect on the internal pressure field generated by the amplitude ρ_0 of the incident wave, is

minor. This is due to the peculiar symmetric nature of the surface load distribution of Load # 1.

Figure 5 exhibits the isobaric contours inside the shell, at non-dimensional frequencies of $k_3a = 3, 5, \text{ and } 10$, but now for a shell loaded with Load # 2 (see Figure 2). Fully developed internal isobaric fields start to be seen for $k_3a = 5$ and more so for $k_3a = 10$. Even though Load # 2 is a type of load that affects all the shell's vibrational modes, the caustic distribution inside the shell is quite similar to those of the unloaded shell (c/o Figure 3) at the same frequencies. The distortions are now greater than for Load # 1 (Figure 4), but the caustics remain more or less in the same places, although their local value changes somewhat. This is quite obvious at $k_3a = 10$, and less evident for $k_3a = 5$ where only the right caustic on the centerline remains in place, while the other seems to have migrated toward the left-most edge of the shell. This figure is computed just as Figure 4, but the coefficient \tilde{A}_1^* now is given by the expression

$$\tilde{A}_1^* = \begin{cases} - \frac{\rho_1}{\rho_2} k_{s2}^2 a^2 \left\{ J_n(k_1a) + \left(\frac{\rho_2}{\rho_0} \right) \frac{2}{\pi(4-n)} \left[\cos \frac{5\pi n}{6} + \cos \frac{n\pi}{3} \right] \right\} & \forall n \neq 2 \\ - \frac{\rho_1}{\rho_2} k_{s2}^2 a^2 \left\{ J_n(k_1a) + \left(\frac{\rho_2}{\rho_0} \right) \left(-\frac{\sqrt{3}}{8} \right) \right\} & , \quad \text{for } n = 2 . \end{cases} \quad (40)$$

We also chose $\rho_2/\rho_0 = 1$ to generate Figure 6 as we did in Figure 4.

It seems that $k_3a = 5$ is the (nondimensional) frequency value considered here at which the cleanest and easiest-to-interpret results are found. Higher k_3a -values clearly clutter the internal pattern too much for the extraction of simple conclusions. The generation of many of these graphs can be quite expensive.

We still have to consider the effect of the surface load alone on the internally transmitted pressure field. This can be done by the superposition principle and the results derived in Section 3. We still use $p_2/p_0 = 1$ to generate the results, which are obtained by means of Equation (30), with \hat{q}_n as given in Equation (26). The integral \hat{I}_n is given by

$$\hat{I}_n = -\frac{\rho_1}{\rho_2} k_{s2}^2 a^2 \bar{I}_n, \quad (41)$$

where \bar{I}_n is given in Equation (36) for Load #1, and in Equation (38) for Load #2. About 20 terms were added in the series of Equation (30). Figure 6 shows the result of this calculation for the single value of $k_3a = 5$ for both Load #1 (upper plot) and for Load #2 (bottom plot). Since only the load is acting (there is no incident wave now), the upper plot is symmetric about the origin, since it is caused by the axially symmetric Load #1. Four caustics are observed, one fully developed at the origin, and three more starting to grow around the shell's inner surface. The lower plot is asymmetric, since it is generated by the non-axially symmetric Load #2. The caustic at the origin, observable in the upper plot, has spread out to a wider region in the bottom plot.

We can now quantitatively address the question of the advantage of sensing transmitted fields inside the shell, in contrast to fields sensed outside it. Equation (31) gave the theoretical ratio P_R for this advantage.

The following discussion will be limited to the case $k_3a = 5$, for which all the ingredients have already been determined for both types of loads. The unloaded shell case and its isobaric contours were displayed in Figure 3. The denominator corresponds to the case of a surface-loaded shell without an

incident wave, a situation displayed in Figure 6 for Load #1 (upper plot) and for Load #2 (bottom graph). It does not make much sense to compute values for the ratio at every point inside the shell. It is more pertinent to consider the values of the P_R -ratio only at the locations of the caustics of its numerator (viz, those shown in Figure 3). The two caustics of Figure 3 are located at $(0.3, 0^\circ)$ and $(0.4, 180^\circ)$ and have values of about 1.3 and 1.2, respectively. For Load #1 the upper graph in Figure 6 shows values of about 0.18 and 0.38, respectively, at the above mentioned caustic locations. For load #2 the lower graph of Figure 6 shows values of 0.50 and 0.74, respectively at those two caustics. The advantage ratio P_R in all cases is summarized in Table 1.

TABLE 1. VALUES OF P_R [EQUATION (31)] for $k_3a = 5$

Caustic # Load #	Left Caustic ($0.4, 180^\circ$)	Right Caustic ($0.3, 0^\circ$)
Load # 1	$\frac{1.2}{0.18} = 6.66$ (16.5 dB)	$\frac{1.3}{0.38} = 3.42$ (10.7 dB)
Load #2	$\frac{1.2}{0.74} = 1.62$ (4.2 dB)	$\frac{1.3}{0.50} = 2.60$ (8.3 dB)

The values in decibels, shown in parenthesis in Table 1, are $20 \log$ of the value of the shown ratio in each case. It is clear that the ratios are larger than one in all cases, and depending on which load and which caustic one considers, Table 1 shows advantages ranging from 4 to about 16 dB. For the construction of the values in Table 1, we assumed that $p_0/p_2 = 1$. Had this

external "signal-to-noise" ratio been smaller, the advantages in Table 1 would have been even larger than shown there.

We can analyze the internal SPL as a function of frequency, at selected points inside the shell, for the various loaded or unloaded conditions we considered. We could also investigate the SPL as a function of radial location across a shell diameter, at selected values of the frequency, for all the loading/unloading conditions.

Figures 7a and 7b show the variation of the (normalized) internal SPL: (i.e., p_3/p_0) as a function of k_3a in the range $0 < k_3a < 10$, at 11 points in the upper half of the shell's interior. If (r, θ) are plane polar coordinates, these 11 points are, for Figures (7a): $(b, 0^\circ)$, $(b, 45^\circ)$, $(b, 90^\circ)$, $(b, 135^\circ)$ and $(b, 180^\circ)$ and for Figure (7b): $(0, 0^\circ)$, $(b/2, 0^\circ)$, $(b/2, 45^\circ)$, $(b/2, 90^\circ)$, $(b/2, 135^\circ)$ and $(b/2, 180^\circ)$. These results are for a cylindrical unloaded shell and they are evaluated by means of Equations (14') and (14). The significance of all these peaks can be given in terms of shell resonances. These resonances could be investigated, one mode at the time, at a later date. As k_3a is increased, the normalized SPL, $|p_3/p_0|$, is basically zero until a shell resonance is excited and a peak is generated. These peaks are seen to be very steep and at any one of them the value of p_3 can be ten or even one hundred times larger than the incident wave amplitude p_0 . Thus, it follows that sound transmission into the shell can only occur through narrow spectral windows centered at the shell's modal resonances, and that the amplitude of the transmitted fields can be so large that the shell can behave as a very effective sound concentrator. It is not simple to analytically extract these conclusions from all the (11) points shown in Figure 7, but it is relatively simple to show them for the point at the center of the shell

($r=0$), where the only two peaks that are present occur at values of $k_3a = 3.8$ and 7.0 , which are the first two roots of $J_0'(k_3a) = 0$ in the considered range. This will be demonstrated toward the end of this section.

Figures 8a and 8b show the same frequency-dependent plots evaluated at the same 11 points inside the shell but now for a shell loaded with Load #1. The shell is excited by both surface load and incident wave. The coordinates of the 11 interior points are given above and the pertinent formulas used in the calculation are given in Equations (32), (14), and (26). We assumed that $p_2/p_0 = 1$ to generate these plots. The coefficients \hat{I}_n appearing in Equation (26) are given in Equations (41) and (36). Comparisons of the corresponding portions of Figures 7 and 8 show that in both cases the resonance peaks appear approximately at the same locations with small changes in amplitude and with the occasional emergence of an additional peak. All these differences are minor and can be attributed to the central symmetry of Load #1, which we saw was of the type affecting only a couple of the shell's modes. Therefore, it is not expected that these will change very drastically the response of the unloaded shell to the incident wave. We now understand better the reason for the similarity between Figures 7 and 8.

Figures 9a and 9b exhibit the same plots shown in Figure 8, but now they are computed for the case where the shell is loaded with Load #2. The formulas required to generate these plots are the same as for Figure 8, but now the load-dependent coefficients \hat{I}_n are given by Equations (41) and (38). Figure 9 is computed at the same eleven internal points as Figures 7 and 8. The two resonance spikes at the center of the shell ($r = 0$) mentioned in Figure 7, remain at the same places but their amplitudes seem to have changed. For most of the other ten points, the spectra shown in Figure 9

contain more (and different) resonance peaks than those shown in Figure 7 for the unloaded shell case. Load #2 is the type of load that affects all the shell modes, and it is not surprising that the same ten internal points now show more complicated pressure spectra, containing more resonance peaks than before. These additional peaks are clearly due to the nature of the surface load. The information in these plots already permits the identification of which of the resonance peaks at which of the internal points is caused by the surface load, and which ones by the incident wave. Future, more detailed studies will allow us to evaluate the distorting effect of the surface load on the shell's modal resonances as excited by the incident wave, for values of the external "signal-to-noise" ratio, p_0/p_2 , different than unity. This ratio was also assumed unity in the figures that follow.

Figure 10 begins a study of the monopole (i.e., $n = 0$) mode of vibration of the shell when it is unloaded. For this symmetrically breathing mode, we plot the contribution of the $n = 0$ partial-wave or normal mode to the (normalized) internal SPL, $|p_3/p_0|$, versus k_3a , at six radial locations ($r = 0, 0.2b, 0.4b, 0.6b, 0.8b$, and b) along any radius. The result is the same in all directions because for $n = 0$, $\cos n\theta \equiv 1$, for all θ . This is a plot of the first (i.e., the $n = 0$) term in the series in Equation (14'). The two peaks already observed before at $k_3a \approx 3.8$ and 7.0 in Figure 7 are present at all radial locations with an amplitude somewhat different for each radial location. At $r = 0$, the two peak amplitudes are the same as those already seen in Figure 7b, and for other locations they change as shown. All the peaks at $k_3a \approx 3.8$ and 7.0 seen in all the plots of Figure 7a (for $r = b$) are caused by this monopole ($n = 0$) mode, as can be easily seen in the top graph of Figure 10.

Figure 11 is the counterpart of Figure 10, but now for the case of a shell loaded with Load #1. Figure 11 displays plots of the first (i.e., $n = 0$) term of Equation (32) versus k_3a . Here \hat{q}_n, \hat{q}_n are given by Equations (14) and (26) and where the only remaining \hat{I}_n coefficient is $\hat{I}_0 = (-\rho_1/\rho_2) k_{s_2}^2 a^2$. The same two resonance peaks present in Figure 10 still persist in Figure 11 but with quite different amplitudes than before. We recall that Load #1 affects only a couple of the modes, but the monopole mode ($n = 0$) is one of them, and this explains the substantial amplitude difference seen between the resonance peaks of Figures 10 and 11.

Figure 12 displays the same results as Figure 11 but now for the shell loaded with the substantially different Load #2. The formulas used in the calculations are as in the above paragraph except that now $\hat{I}_0 = (-\rho_1/\rho_2) k_{s_2}^2 a^2 / \pi$. We note that the same persistent peaks appearing before at $k_3a \approx 3.8$ and 7.0 continue to be present for all radii but now with amplitudes quite different from those in Figure 10, and of course, from those in Figure 11.

The effect of the monopole resonances is very persistent and strong.¹⁷ All the computed plots of the summed interior SPL consistently exhibit those two strong narrow peaks at the mentioned pair of spectral locations. Peaks at other frequencies are caused by other higher modes. At values of k_3a away from those resonance values, the (otherwise strong) monopole contribution to the fields, disappears and the fields become mixtures of (weaker) higher-order modes. We see now, for example, that all the isobaric contour plots shown in Figures 3 to 6 and computed for arbitrarily chosen values of the non dimensional frequency of $k_3a = 1, 3, 5,$ and 10, have all missed the monopole resonance contributions which occur within narrow bands around 3.8 and 7.0.

This merely means that the internal fields and values of the advantage ratio P_R computed earlier, could be considerably enhanced if they were recomputed at the preferred k_{3a} -values of 3.8 and 7.0. Therefore, the natural filter and lens-like or sound concentrating effect of the shell can be enhanced beyond the values shown earlier (i.e., in Table 1), by operating near these two resonances of the monopole mode contained within the original broad band ($0 < k_{3a} < 10$) considered.

The monopole mode contribution to the internal fields can also be studied by computing its radial variation for various values of k_{3a} . Figures 13 to 15 summarize this effect and its radial dependence just as Figures 10 to 12 studied it for its frequency dependence. Figure 13 is a plot of the internal pressure associated with the first (i.e., $n = 0$) term of the series in Equation (14') for an unloaded shell displayed versus radial coordinate r in the range $0 < r/b < 1$, at the usual four arbitrary values of k_{3a} (viz., $k_{3a} = 1, 3, 5$ and 10) that we have chosen to span the band $0 < k_{3a} < 10$. Figure 14 is analogous to 13 and it exhibits the first (i.e., $n = 0$) term of Equation (32), for Load #1. The coefficient \hat{I}_0 here is $(-\rho_1/\rho_2) k_{s_2}^2 a^2$ as we found for Figure 11, and we have assumed $p_2/p_0 = 1$. Figure 15 displays the first term of the series in Equation (32), now for Load #2. In this case the coefficient \hat{I}_0 is $(-\rho_1/\rho_2) k_{s_2}^2 a^2 / \pi$ as it was for Figure 12, and we still assume $p_2/p_0 = 1$. When we compare the plots in these three figures for corresponding values of k_{3a} , we see that the transmitted sound pressure amplitudes vary quite substantially as we go from Figure 13 (unloaded case), to Figure 14 (Load #1) to finally Figure 15 (Load #2). Both these loads affect the monopole ($n = 0$) mode and this explains the variations in corresponding internal pressure amplitudes observed between these three figures. It is quite noticeable that

the nulls present in these plots at each k_3a -value do not change their radial locations as we go from Figures 13 to 15. Closer inspection shows that in the range of the figures (i.e., $0 < k_3a < 10$), the nulls seen in Figure 13 are all manifestations of the first three zeroes of $J_0(k_3r)$, which are known to occur at $k_3r = 2.40, 5.52,$ and 8.65 . Since $k_3a = 10$ for, say, the top graph in Figure 13, division of these zeroes by ten yields r/a -values of $0.24, 0.55$ and 0.86 . These r/a -values are undistinguishable from the r/b -values shown as the abscissas of the nulls in that plot because the a/b -value for this shell is very close to unity (viz, 1.0112). For the second plot in Figure 13, calculated for $k_3a = 5$, division of the three roots by five eventually yields: $r/b \approx 0.48, 1.10,$ and 1.73 . Only the first of these appears in the range (i.e., $0 < r/b < 1$) where the plot was computed. Analogous results are found for all other plots of Figure 13 and for those in Figures 14 and 15. It follows that these nulls in the monopole contribution to the internal field are controlled by the zeroes of $J_0(k_3r)$ since this factor is indeed all that remains in Equation (14'), for the monopole (i.e., $n = 0$) case.

It remains to formally demonstrate that at the center of the shell (i.e., $r = 0$) the resonance peaks appearing in the spectral plots are controlled by the resonance conditions $J_0'(k_3a) = 0$. Since the 6×6 determinants involved here were so complicated, it was unexpected to find such a simple condition. This result was already anticipated when we discussed Figure 7.

For $r = 0$ all the terms in the series shown in Equation (14') vanish except for the $n = 0$ term. This is so because all the Bessel functions of zero argument vanish except $J_0(0)$ which takes on value unity. The $n = 0$ term reduces to coefficient q_0 . Using the entries in Appendix A this coefficient takes the form

$$q_0 = \frac{\frac{\rho_1}{\rho_2} k_{s2}^2 a^2 J_0(k_1 a) D_{16}^0 + k_1 a J_0'(k_1 a) D_{26}^0}{\frac{\rho_3}{\rho_2} k_{s2}^2 b^2 J_0(k_3 b) D_{46}^0 + k_3 b J_0'(k_3 b) D_{56}^0} \quad (42)$$

where D_{16}^0 , D_{26}^0 , ... are the 5 x 5 minor determinants of the elements d_{16} , d_{26} , ... listed in Appendix A, all evaluated for $n = 0$. Resonances in the SPL are associated with the vanishing of the denominators of the series. For this single term in Equation (42), resonances are associated with the vanishing of its denominator. Since the inner fluid (air) has a density ρ_3 very tenuous compared to that of the steel shell (i.e., $\rho_3 \ll \rho_2$), it follows that unless the shell is extremely thin, the first term in the denominator of Equation (42) is negligible compared to the second, and that second one immediately yields the condition $J_0'(k_3 b) = 0$. Since the b/a -ratio for this shell is very close to unity, this condition is undistinguishable from $J_0'(k_3 a) = 0$, which yields the results observed in Figure 7, and which we wanted to formally demonstrate here for this air-filled thin steel shell.

Basic explanations for the origin of the internal caustics at the higher $k_3 a$ - values, for which the internally transmitted fields are more developed, can be given in terms of creeping waves as we did earlier for coated cylindrical shells,⁶ and for fluid-filled cavities within elastic media.¹⁸ It is well known that transmission of sound through (curved) shells differs significantly from sound transmission through flat plates only at the low-end of the frequency spectrum (i.e., in the Rayleigh region and in a portion of the resonance region). The previously mentioned cut-off value of about $k_3 a = 20$, where the numerical instabilities and the slowness of the series

convergence begin to prevent the possibilities of computation, seems to be the natural upper bound for the spectral region beyond which sound transmission through shells could well be modeled by means of flat plate theories. All our sound structure interaction work that we have quoted above (as well as other references not mentioned here) was summarized in another (updated) review of the Resonance Scattering Theory (RST) that appeared in 1982.¹⁹

We conclude this sub-section with a statement of the version of the Fourier theorem that permits the decomposition of the arbitrary load acting on the shell given in Equation (16).

Theorem: Let $f(\theta)$ be a function satisfying Dirichlet boundary conditions on $0 < \theta < a$, and let

$$\bar{f}_c(n) = \int_0^a f(\theta) \cos \frac{n\pi\theta}{a} d\theta \quad (43a)$$

be its Fourier finite-cosine transform. Then $f(\theta)$ admits the representation

$$f(\theta) = \frac{1}{a} \sum_{n=0}^{\infty} \epsilon_n \bar{f}_c(n) \cos \frac{n\pi\theta}{a} \quad (43b)$$

at each point of $(0,a)$ where $f(\theta)$ is continuous.

Corollary: Let $a = \pi$, then at each point of $(0, \pi)$ the above finite transform pair is

$$\bar{f}_c(n) = \int_0^{\pi} f(\theta) \cos n\theta d\theta \quad (44a)$$

$$f(\theta) = \frac{1}{\pi} \sum_{n=0}^{\infty} \epsilon_n \bar{f}_c(n) \cos n\theta. \quad (44b)$$

SECTION 5
SHELL THICKNESS AND MATERIAL COMPOSITION EFFECTS

This section presents a detailed study of the effects of shell thickness and material composition on the pressure fields transmitted inside the doubly excited shell. The computed displays presented up to this point pertain only to thin shells of a single thickness and composition. Those results will now be extended to include thicknesses as high as 20 percent, and compositions including aluminum and steel. Both an incident plane wave and an external surface excitation act on the outer surface of the submerged shell.

For the reasons described earlier, we will select a fixed nondimensional frequency such that $k_3a=5.0$. For this frequency, it follows that $\lambda=a$, which means that one is at the edge of the resonance region. For any other selected frequency the calculations follow a similar pattern, although at high frequencies, both analysis and computations are harder to carry on. It is of interest to first study the isobaric contour plots of the insonified shell in the absence of surface loads and later to recompute them when the submerged shell is additionally excited by Loads #1 and #2.

Figure 16 shows the isobaric contours of the internal SPL when the submerged shell is insonified but subject to no surface excitation. The shell material is steel, the frequency is such that $k_3a=5.0$, and the thicknesses are such that $b/a=0.80, 0.85, 0.90$ and 0.95 . The calculations are performed by means of Equations (14') and (14). The thicker the shell is, the smaller the local maxima that are observed at the various corresponding caustic

locations. This merely means that away from resonances, thicker shells allow for the transmission of smaller amounts of sound energy into its internal points. The caustic locations shift with thickness but in a slow fashion that easily permits the tracing of a given caustic as the shell thickness is changed.

Figure 17 shows analogous contour plots for a steel-shell subjected to the incident pressure wave and to the surface excitation generated by Load #1. The nondimensional frequency is still $k_3a=5.0$, and the same four shell thicknesses (i.e., $b/a=0.80, 0.85, 0.90,$ and 0.95) are displayed. These plots are not too different from the corresponding ones in Figure 16, particularly for the thinner shells. These contours are computed using Equations (21), (18), (20), and (36). The similarity between corresponding plots in Figures 16 and 17 can be explained because, as we have seen, Load #1 merely affects a couple of the shell modes.

Figure 18 displays the same information contained in Figure 17 but now the outer shell's surface is excited with Load #2. The differences between Figures 18 and 16 are more pronounced than between Figures 17 and 16 because Load #2 affects all the shell modes.

The information exhibited in Figures 16 to 18 for $k_3a=5$ is given in Figures 19 to 21 for $k_3a=7.0$. In Figure 19 the shell is insonified but there is no surface load; in Figure 20 the shell is excited with Load #1; and in Figure 21 it is excited with Load #2. At higher frequencies one observes more caustics that are more developed than at lower frequencies.

Steel and aluminum do not behave in the same fashion, and the differences are displayed in Figures 22 to 27. These six figures display information about the internally transmitted SPL analogous to that shown in Figures 16

to 21, but now for an aluminum shell. Figure 22 shows the internal SPL contours for the usual four thicknesses, at the fixed nondimensional frequency of $k_3a=5$ for an unloaded aluminum shell. The aluminum properties used in these plots are : $\rho_2 = 2.70 \text{ g/cm}^3$, $c_{d2} = 6.374 \times 10^5 \text{ cm/sec}$, and $c_{s2} = 3.111 \times 10^5 \text{ cm/sec}$. The calculations are performed using Equations (14) and (14'). Figure 23 displays similar results when the insonified shell is excited by the outer surface Load #1. In this case, the calculations are done by means of Equations (21), (18), (20), and (36). Figure 24 exhibits the corresponding results for the case of Load #2, in which case, the calculations are made by means of Equations (21), (18), (20), and (38). Figure 25 deals with the insonified but otherwise unloaded aluminum shell in water at $k_3a=7.0$. The differences in transmissibility due to steel and aluminum emerge from the comparison of Figures 19 and 25. Aluminum being a "softer," more penetrable material allows the transmission of stronger internal SPL's than steel, at about the same internal points, and for corresponding shell thicknesses.

Figure 26 corresponds to the aluminum shell at $k_3a=7.0$ when the shell's surface is excited with the symmetric Load #1. Figure 27 displays analogous information when the Load #2 is the one exciting the outer surface of the insonified aluminum shell. Comparing Figures 27 and 21 for aluminum and steel, respectively, shows that for the same thicknesses, the stiffer steel shell permits the transmissibility of a weaker internal pressure field than aluminum, at about the same spatial points. Very lengthy quantitative comparisons could be extracted from the detailed comparisons of all the cases displayed in all these figures. We have just stated the most salient global

features which are most evidently noticeable from a quick inspection of the displayed results.

The effect of the isolated surface excitation (either Load #1 or #2) on a steel or aluminum shell, is shown in Figures 28 to 31. By means of the superposition principle and the analysis of the doubly excited shell in Section 3, it is possible to study the effect of the surface load in the absence of the incident wave. The calculations are performed by means of Equations (30), (26), and either Equation (36) for Load #1 or Equation (38) for Load #2. Figure 28 displays the internally transmitted pressure contours due to the isolated surface excitation of Load #1 acting on the steel shell. Figure 29 exhibits the same information for solely Load #2 acting on the steel shell. Figure 30 pertains to Load #1 acting alone on the outer surface of the aluminum shell. Figure 31 exhibits the same information when the shell excitation is caused by Load #2. All these plots are computed for the usual four shell thicknesses (viz, $b/a=0.80, 0.85, 0.90, \text{ and } 0.95$) at the fixed non-dimensional frequency of $k_3a=5.0$. These results are the ones needed to compute the sum appearing in the denominator of Equation (31), which yields the advantage ratio P_R . A summary of results for all the thicknesses, loads, and shell compositions is given in Table 2. This table also shows the results of computing the advantage ratio P_R in all cases, just as we did it earlier in Table 1. The ratio P_R almost always comes out to be greater than one, and thus, it follows that for these material compositions and shell thicknesses, under the shown conditions of insonification and external excitation, it still appears to be more advantageous to sense pressure fields inside rather than outside the shell. Ideal spatial locations have been identified by means of the caustics generated by the overall lense-like action of the shell.

TABLE 2. VALUES OF P_R FOR VARIOUS SHELL-THICKNESSES AND COMPOSITIONS

The advantage ratio P_R for various shell thicknesses and compositions. From Eq. (31), using $k_3a=5.0$. Steel above, aluminum, below.

	b/a=	LOAD #	LEFT CAUSTIC ON AXIS	RIGHT CAUSTIC ON AXIS	
STEEL	0.80	LOAD 1	$\frac{0.18}{0.18} = 1.0$ (0dB)	$\frac{0.22}{0.12} = 1.8$ (5.3 dB)	
		LOAD 2	$\frac{0.18}{0.15} = 1.2$ (1.6dB)	$\frac{0.22}{0.15} = 1.5$ (3.4dB)	
	0.85	LOAD 1	$\frac{0.275}{0.025} = 11$ (20.8dB)	$\frac{0.30}{0.04} = 7.5$ (17.6dB)	
		LOAD 2	$\frac{0.275}{55} = 0.005$	$\frac{0.30}{40} = 0.008$	
	0.90	LOAD 1	$\frac{0.275}{0.060} = 4.6$ (13.2dB)	$\frac{0.225}{0.050} = 4.5$ (13.0dB)	
		LOAD 2	$\frac{0.275}{0.10} = 2.75$ (8.8dB)	$\frac{0.225}{0.10} = 2.25$ (7.0dB)	
	0.95	LOAD 1	$\frac{0.55}{0.10} = 5.5$ (14.8dB)	$\frac{0.50}{0.07} = 7.1$ (17.1dB)	
		LOAD 2	$\frac{0.55}{0.25} = 2.2$ (6.8dB)	$\frac{0.50}{0.25} = 2.0$ (6.0dB)	
		b/a=	LOAD #	LEFT CAUSTIC	RIGHT CAUSTIC
	ALUMINUM	0.80	LOAD 1	$\frac{0.35}{0.10} = 3.5$ (10.9dB)	$\frac{0.45}{0.20} = 2.25$ (7.0dB)
LOAD 2			$\frac{0.35}{0.35} = 1.0$ (0dB)	$\frac{0.45}{0.45} = 1.0$ (0dB)	
0.85		LOAD 1	$\frac{5.0}{0.125} = 40$ (32dB)	$\frac{5.0}{0.125} = 40$ (32dB)	
		LOAD 2	$\frac{5.0}{24} = 0.2$	$\frac{5.0}{24} = 0.2$	
0.90		LOAD 1	$\frac{0.55}{0.15} = 3.7$ (11.3dB)	$\frac{0.55}{0.125} = 4.4$ (12.9dB)	
		LOAD 2	$\frac{0.55}{8.0} = 0.07$	$\frac{0.55}{8.0} = 0.07$	
0.95		LOAD 1	$\frac{0.75}{0.15} = 5.0$ (14dB)	$\frac{0.75}{0.30} = 2.5$ (8dB)	
		LOAD 2	$\frac{0.75}{0.50} = 1.5$ (3.5dB)	$\frac{0.75}{0.50} = 1.5$ (3.5dB)	

Note: For steel, all numerators come from Fig. 16, and all denominators come from Figs. 28 and 29 for Loads 1 and 2, respectively.

For aluminum, all numerators come from Fig. 22, and all denominators from Fig. 30 (Load 1) and 31 (Load 2). The numbers in parentheses are 20 log the value of the ratio, next to them.

It remains to exhibit the spectral values of the normalized pressure $|p_3/p_0|$ amplitudes at selected points within the shell. These are shown in Figures 32 to 35 for seven internal points located in the upper-half of the shell's interior. The coordinates of these seven points are $(0,0^0)$, $(b,0^0)$, $(b,90^0)$, $(b,180^0)$, $(b/2,0^0)$, $(b/2, 90^0)$, and $(b/2, 180^0)$. The peaks observed in the spectral band which we have displayed (i.e., $0 < k_3 a < 10$) correspond to shell-resonances. Figure 32 corresponds to an unloaded steel shell of thickness $b/a=0.80$. Figures 33, 34 and 35 correspond to an unloaded steel shell of thickness $b/a=0.85$, 0.90 , and 0.95 , respectively. All these plots are computed from Equations (14) and (14'). The only set of resonances displayed in these plots which admits an immediate simple interpretation are the two seen in the graph for the shell's center $(0,0^0)$. These resonances can be shown to correspond to the first two roots of $J_0'(k_3 b)=0$, since it is the inner radius b that bounds the approximately rigid enclosure around the internal air-filled space. The first two such roots are 3.83 and 7.06, and they have to be divided by the value of the respective b/a -ratio in each one of the graphs. For example, in Figure 32, this pair of peaks are seen to occur at $k_3 a=3.83/0.80=4.78$ and $7.06/0.80=8.82$ just as it is theoretically predicted. Analogous situations are observed in Figures 33 to 35.

Figures 36 to 39 are the counterparts of the previous four figures, but now the insonified steel shell is externally excited by surface Load #1. They are computed at the same seven internal points within the band $0 < k_3 a < 10$, by means of Equations (30), (26), and (36), and they are plotted versus $k_3 a$. The persistent pair of resonances observable at the plot for the shell's center $(0, 0^0)$ are slightly shifted downwards from the corresponding values they had in Figures 32 to 35 due to the fact that now the shell is excited by Load

#1. The shift is small since Load #1 just affects a couple of the shell modes. For any of the other six considered points, the resulting peaks correspond to numerically computed shell resonances, which are not easily obtainable or identifiable by analytical methods. Each one of these four figures corresponds to each one of the four shell thicknesses used.

Figures 40-43 are the counterparts of Figures 36 to 39, but now for the steel shell externally excited with Load #2. The computations of the spectra are carried on at the same seven internal points by means of Equations (30), (26), and (38), and they are plotted versus k_3a . The only set of resonances admitting quick and easy interpretations is the strong pair in the plot for the shell's center $(0, 0^0)$. These resonances are seen to shift downwards from the values they had in Figures 32 to 35, since now the shell is excited by Load #2. These spectral plots show the locations of the resonance peaks in the k_3a -domain for all the considered shell-thicknesses. All the peaks correspond to numerically computed modal shell resonances, since now they are not roots of easily tractable analytic expressions. All these modal fundamentals and overtones quantitatively display the way resonances change from one internal point to another. This completes the description of the figures.

SECTION 6
CONCLUSIONS

We have developed the exact formulation required to analytically and computationally model the transmission of plane acoustic waves into submerged, elastic, air-filled, cylindrical shells subjected to arbitrary loads on their outer surface. We have generated the codes required to calculate these interior fields in a variety of pertinent cases. The surface loads were Fourier-decomposed, and in view of the linearity of the system of partial differential equations governing this problem, we were able to use the superposition principle to separate the effect of the incident wave from the effect of the surface loads on the internally transmitted pressure fields. Modal shell resonances were caused by both types of excitations and we presented a study of their interplay as they influenced the interior fields. The exact full equations of (2-D) elastodynamics were used to describe the shell motions, thus going beyond any description that could possibly be provided by any (approximate) shell theory. We used the separated contributions to the internal field caused by the surface load and by the incident wave, to compute an advantage ratio which measured the gains that resulted from sensing the internally transmitted fields rather than the pressure fields outside the shell on its external surface. This ratio showed gains: (1) that were always larger than one, (2) that at the internal caustics, present at any frequency, were many times larger than one (see Tables 1 and 2) , and (3) that in the vicinity of certain prominent and

persistent shell resonance-frequencies, could exceed many times over, the results shown in Tables 1 or 2. The internal fields were displayed by means of isobaric contours that clearly depicted the development of the internal field and of its caustics as the k_3a values were increased. Special codes were developed to generate these isobaric contour plots for all the pertinent cases (i.e., Figures 3 to 6) which included: (1) the surface loads alone acting on the shell, (2) the incident wave acting alone on the shell and, (3) the surface loads and the incident wave both acting on the shell. Two specific types of surface loads were considered which were harmonic in time and symmetric about the direction of the incident wave. Load #1 acted on the entire outer surface of the shell and had central symmetry. Load #2 acted only on a portion of the shell's surface and had no such symmetry. In all cases and for all loads we generated a succession of plots for four increasing k_3a values in the band $0 < k_3a < 10$. The internal SPL was also studied, computed, and displayed at (several) points inside the upper half of the shell, as a function of k_3a . These spectral plots were produced for various loaded and unloaded, insonified or silent combination of conditions. At all the locations, these spectral plots, which accounted for all the modal contributions to the internal field, quantitatively showed (viz., Figures 7 to 9) the distorting effect the surface loads had on the spectral characteristics of the internal part of the field caused by the incident wave. The isolated effect of the monopole mode ($n = 0$) was studied separately (Figures 10 to 15) for the three possible combinations of loading and insonification conditions. The internal SPL was plotted for that $n = 0$ mode alone as a function of k_3a at various internal points (Figures 10 to 12), or as a function of radial coordinate at fixed values of k_3a (Figures 13 to

15). In many cases we showed which resonance peaks were caused by which type of excitation mechanism. In some cases we demonstrated that the locations of certain resonance peaks or resonance nulls were governed by very simple resonance conditions that one may have expected to remain veiled behind the rather formidable general and exact formulation presented here. This was particularly striking for the peaks in the total pressure spectrum at the center ($r = 0$) of the shell, displayed in Figure 7, and for the nulls in the radial dependence of the monopole contribution shown in Figures 13 to 15. These welcomed results served as natural check points. In all the results presented here, the surface loads had amplitudes no larger than that of the incident wave. This meant that the external "signal-to-noise" ratios considered here were never less than unity. The preceding systematic investigation of the fields transmitted inside loaded shells at low-to-medium frequencies showed clearly the filtering and focusing effects of the shell in the frequency and the spatial domains, respectively. Thus, for not too overpowering surface loads, the thin air-filled shell studied here acted as a very effective sound concentrator, particularly within certain narrow spectral windows determined by the resonances of the monopole vibrational mode. Furthermore, the resulting caustics within the displayed isobaric contours did not seem to migrate too much from their locations in the unloaded configuration, by the distorting action of either type of surface load. This permanence of the caustic locations at a given frequency, under various types of external loads, is a very encouraging result.

The final section studied the effects of shell thickness and material composition on sound transmissibility into the structure. Four shell thicknesses spanning a wide range of interest were used, as well as a couple

of pertinent structural materials. For a fixed, relatively low frequency of the incident wave, for which the internally transmitted pressure-field already showed sufficient development, we generated the contour plots of the internal SPL for all shell thicknesses and materials. This was done for the insonified but otherwise unloaded shell in Figures 16 and 22. When the shell was externally excited in addition by Load #1, the results were shown in Figures 17 and 23. The case of the submerged shell loaded by the unsymmetric Load #2 was studied in Figures 18 and 24. For a higher frequency value of $k_3a=7$, which coincides very closely with the k_3a -value corresponding to the spectral monopole resonance of the shell at its center, we repeated the above calculations. The results were shown in Figures 19 to 21 and 25 to 27.

Internal SPL for shells that are excited by the external loads but not by the incident wave, were generated via the superposition principle and displayed in Figures 28 to 31 for all relevant shell-thicknesses and compositions. These figures and also Figures 16 and 22 permit the computation of the advantage ratio, P_R , defined in Equation (31), for all shell thicknesses and loading conditions as shown in Table 2. Spectral responses of the internal field at selected inner points and for the four shell-thicknesses in question, were computed and displayed in the final set of 12 graphs. The first four figures of that set (i.e., Figures 32 to 35) are for the unloaded shell. The next four (i.e., Figures 36 to 39) are for the shell excited by Load #1 and the final four (i.e., Figures 40 to 43) are for the shell excited by Load #2. This analysis of shell thicknesses and composition effects on the internally transmitted fields shows that under the conditions of the study, the earlier conclusions continue to hold. Therefore, in view of the lens-like sound-concentrating effect of the shell in space and of its filtering action

in frequency, it appears more advantageous to sense internal rather than external fields for all the shell thicknesses and compositions considered here. Ideal locations to perform the internal sensing have been determined by means of the local maxima (i.e., the caustics) that we have extensively computed in this idealized model to quantitatively illustrate and demonstrate the concept.

For most cases where this analysis will be of practical value, the assumptions used here seem to be all justified. The incident waveform usually has a fixed frequency relative to the target size. This frequency is usually low. When the incident frequency is high, the internal fields are very complicated but then, other mechanisms enter into play and this type of study loses its urgency. The incident wave and the surface excitations both induce target eigenfrequencies whose effects become manifest in the plots of the internally transmitted fields. These resonance features became obvious when plots are generated versus frequency or in the space domain by means of the contour plots. It is well known and amply documented in the literature of the RST¹⁹⁻²⁴ that analogous resonance features manifest themselves in the scattered fields present in the outer medium. The external "signal-to-noise" ratios are generally high and never fall below unity. The shell vibrations are sufficiently small to be correctly modeled by the linear equations of two-dimensional axisymmetric elastodynamics. Finally, although surface excitations caused by flow are extremely complicated, time-varying, and in some instances, probabilistic in their description, in specific cases they can be modeled by the simple types of symmetric or asymmetric loads displayed in Figures 1 and 2.

Portions of this work were presented at a Professional Society Meeting,²⁵ and highlights of the most salient features were published in a Journal Article.²⁶ Conversations with the sponsors at ONR (Code 432) were particularly enlightening and we acknowledge them here.

$$\begin{cases} r = 4 \\ s = 6 \end{cases}$$

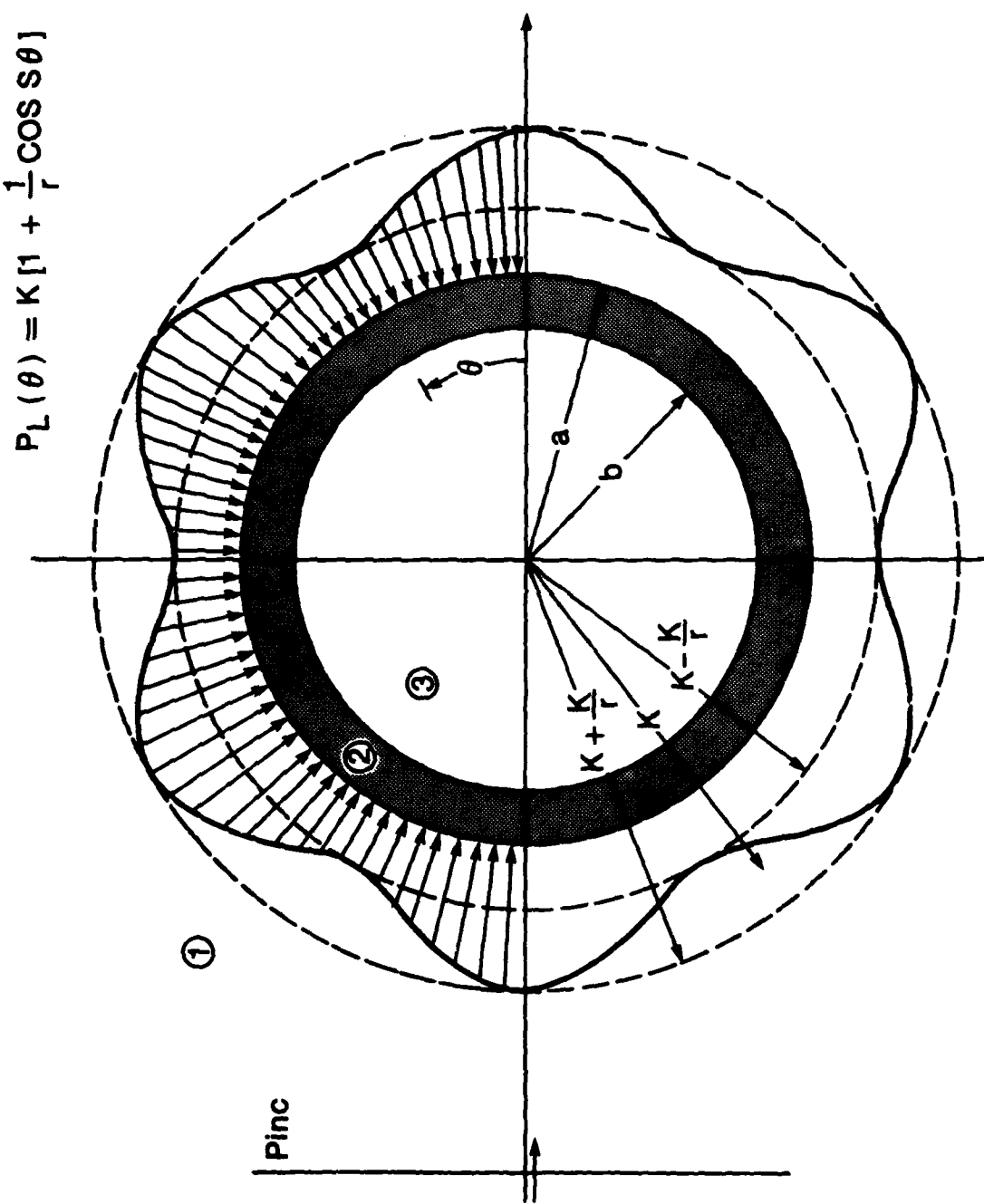


FIGURE 1. THE CYLINDRICAL SHELL, WITH LOAD NO. 1 ACTING ON ITS ENTIRE OUTER SURFACE, AS IT INTERACTS WITH THE INCIDENT SOUND WAVE OF AMPLITUDE P_0

$$P_L(\theta) = \begin{cases} 0 & \dots\dots\dots 0 < \theta < \frac{\pi}{3} \\ \sin(2\theta - \frac{2\pi}{3}) & \dots\dots\dots \frac{\pi}{3} < \theta < \frac{5\pi}{6} \\ 0 & \dots\dots\dots \frac{5\pi}{6} < \theta < \pi \end{cases}$$

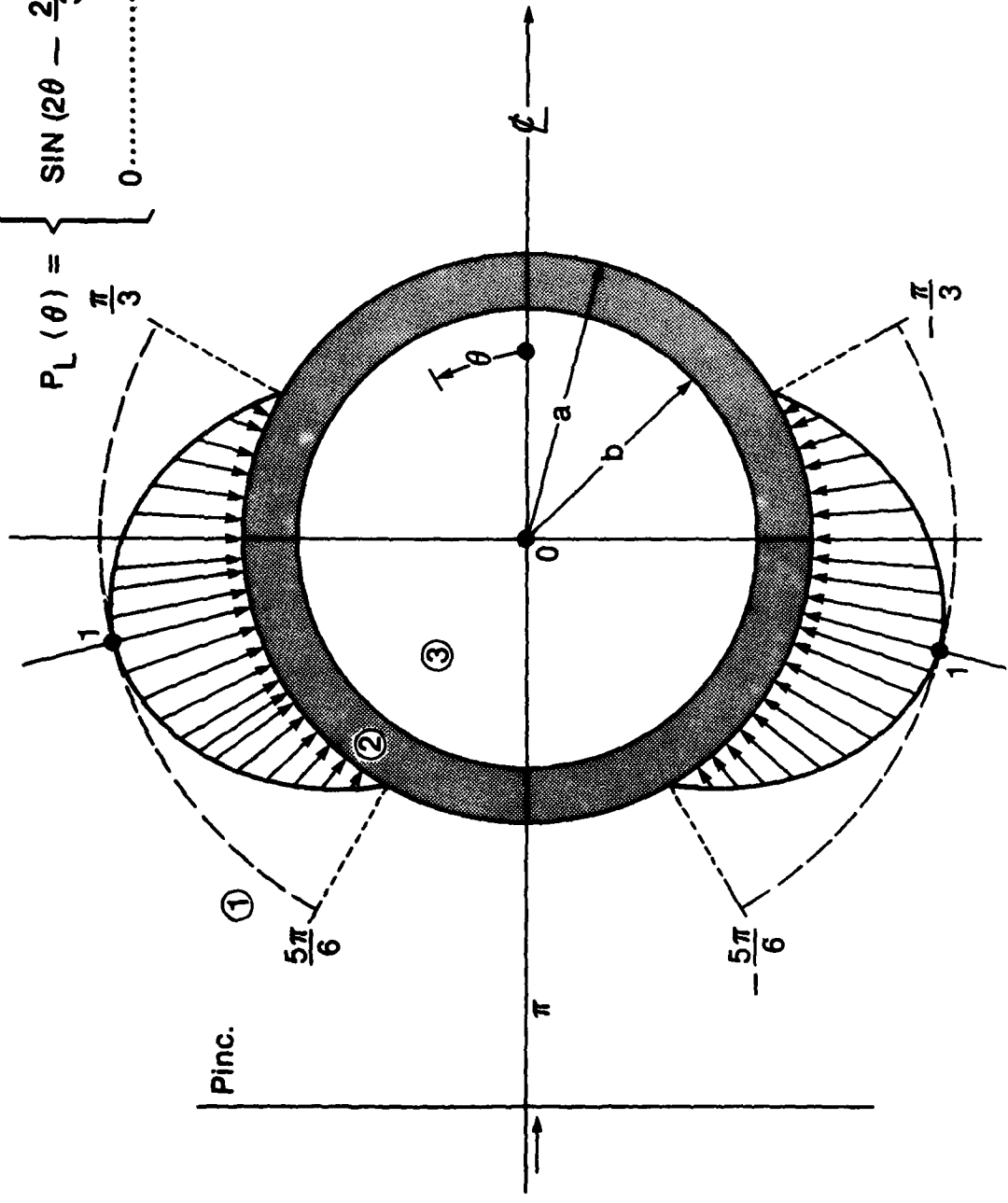


FIGURE 2. THE CYLINDRICAL SHELL WITH LOAD NO. 2 ACTING ON PORTION OF ITS OUTER SURFACE. THE INCIDENT SOUND WAVE TRAVELS FROM LEFT TO RIGHT AND IT IS TRANSMITTED INTO THE LOADED SHELL'S INTERIOR

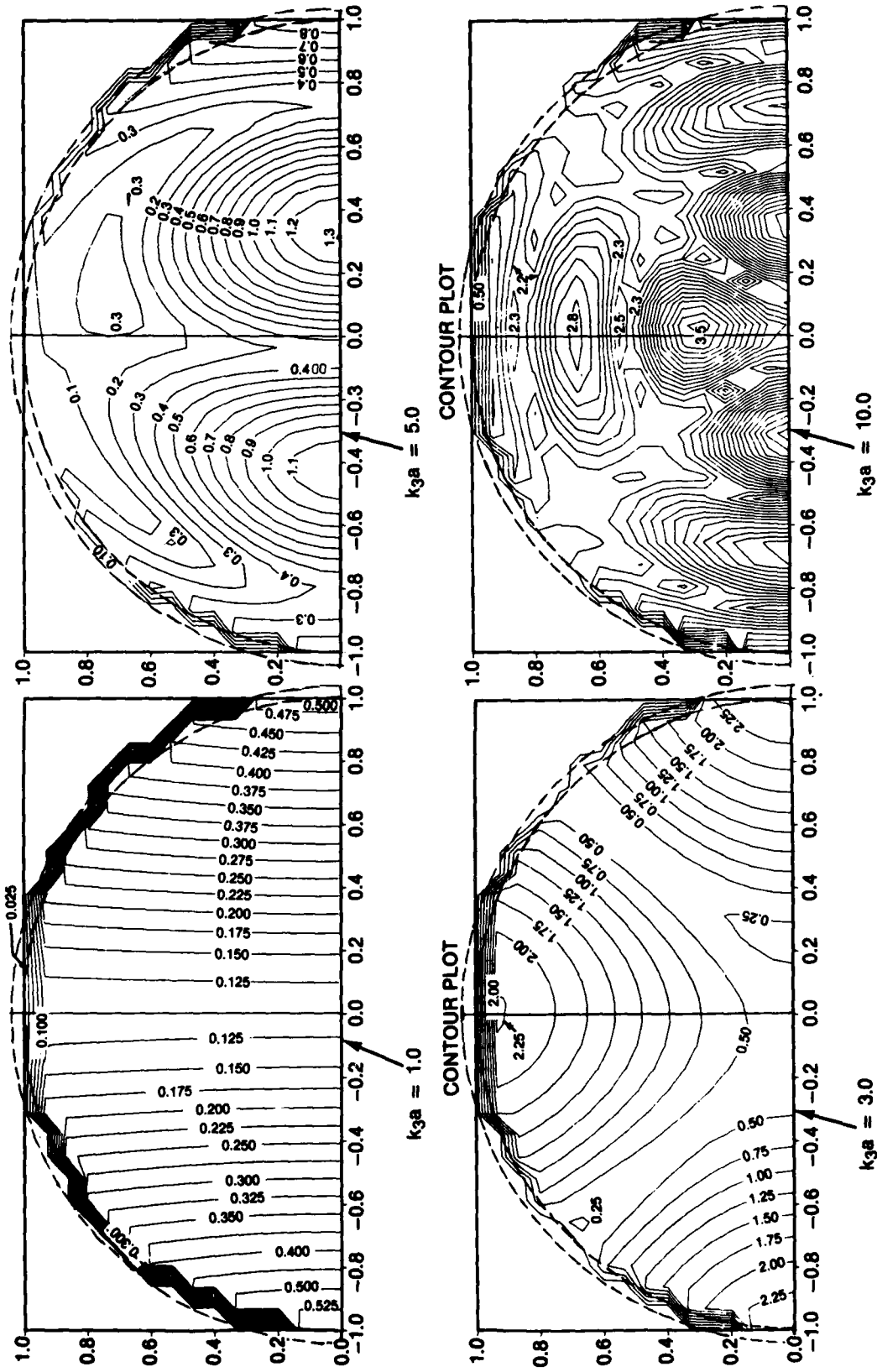


FIGURE 3. INTERNALLY TRANSMITTED ISOBARIC CONTOUR PLOTS OF AN UNLOADED STEEL CYLINDRICAL SHELL INTERACTING WITH A PLANE MONOCHROMATIC INCIDENT SOUND WAVE OF AMPLITUDE p_0 , FOR FOUR VALUES OF k_{3a} ($= 1, 3, 5$ AND 10)

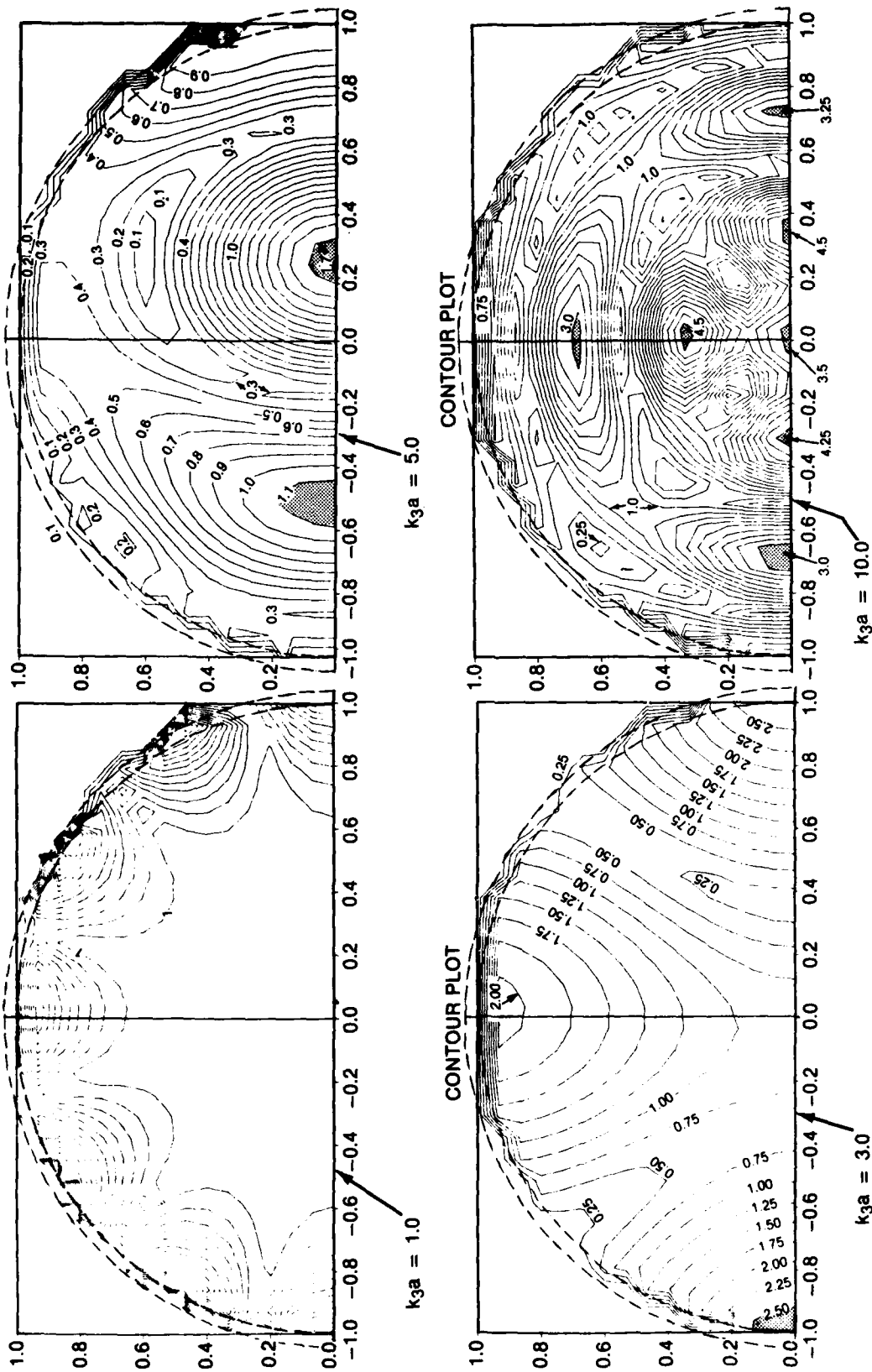


FIGURE 4. INTERNALLY TRANSMITTED ISOBARIC CONTOUR PLOTS OF AN AIR-FILLED CYLINDRICAL STEEL SHELL, LOADED WITH LOAD NO. 1, WHICH INTERACTS WITH A PLANE INCIDENT ACOUSTIC WAVE AT FREQUENCIES SUCH THAT $k_{3a} = 1, 3, 5$ AND 10

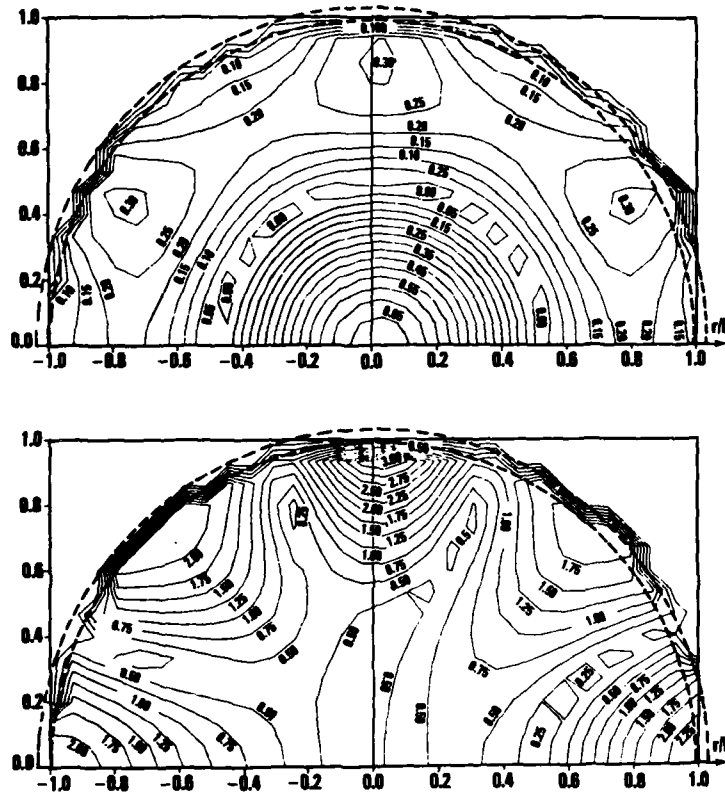


FIGURE 6. INTERNALLY TRANSMITTED ISOBARIC CONTOUR PLOTS FOR A SUBMERGED, AIR-FILLED, CYLINDRICAL SHELL, LOADED WITH LOAD NO. 1 (UPPER PLOT), OR WITH LOAD NO. 2 (LOWER PLOT), BOTH FOR $k_3 a = 5$. NO INCIDENT WAVE INTERACTS WITH THE SHELL HERE

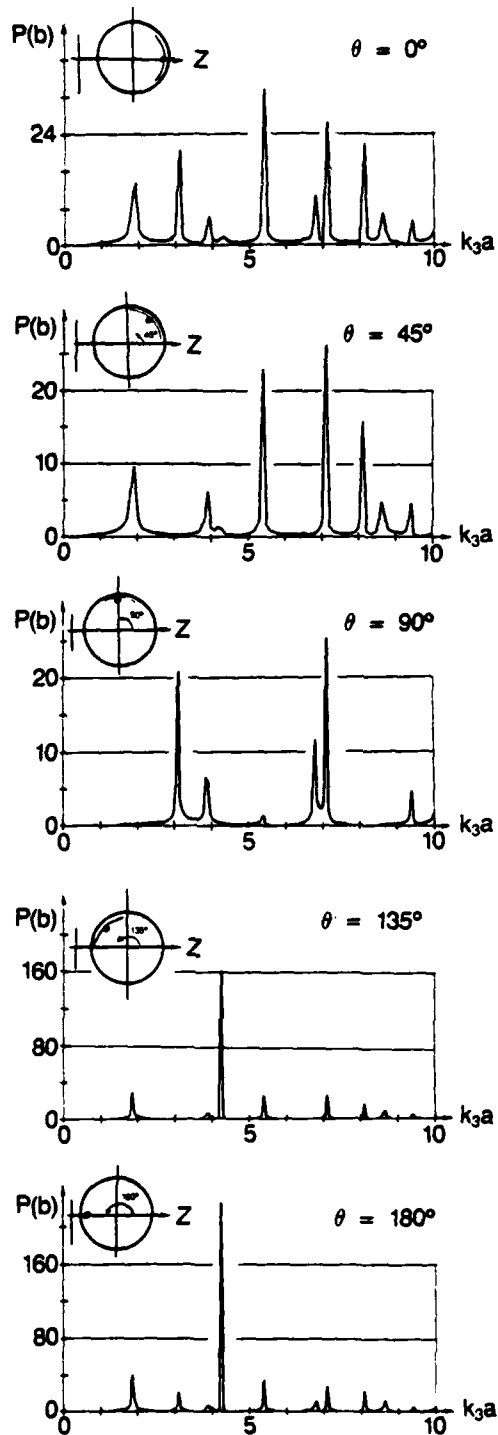


FIGURE 7a. INTERIOR PRESSURE LEVELS, $|P_3/P_0|$, VERSUS $k_3 a$, AT FIVE (OF ELEVEN) LOCATIONS INSIDE AN UNLOADED CYLINDRICAL SHELL IN WATER INSONIFIED BY AN INCIDENT PLANE WAVE

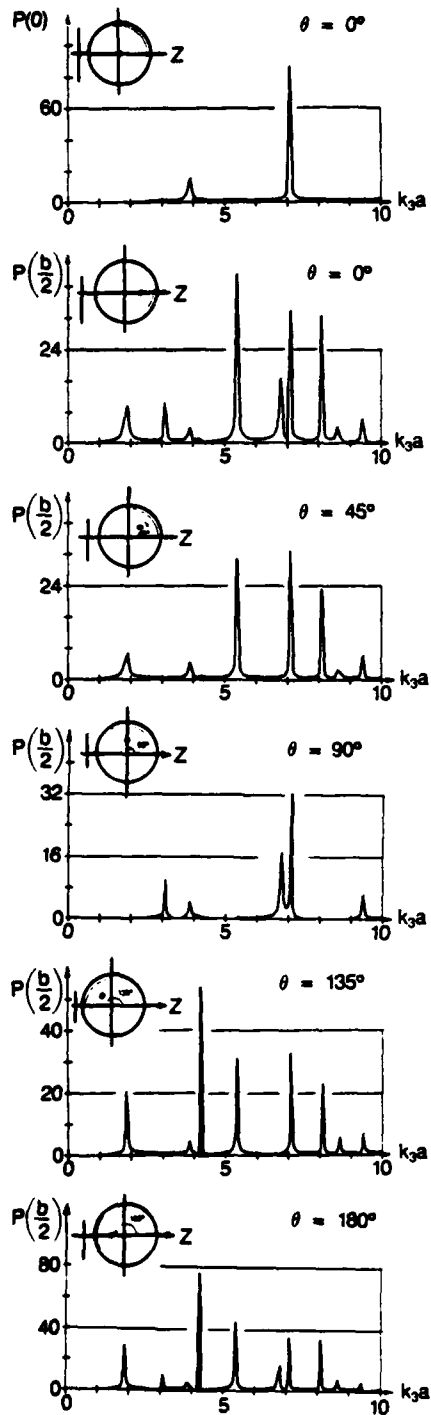


FIGURE 7b. INTERIOR PRESSURE LEVELS, $|p_3/p_0|$, VERSUS $k_3 a$, AT SIX ADDITIONAL (OF ELEVEN) POINTS INSIDE AN UNLOADED SHELL IN WATER INSONIFIED BY AN INCIDENT PLANE WAVE

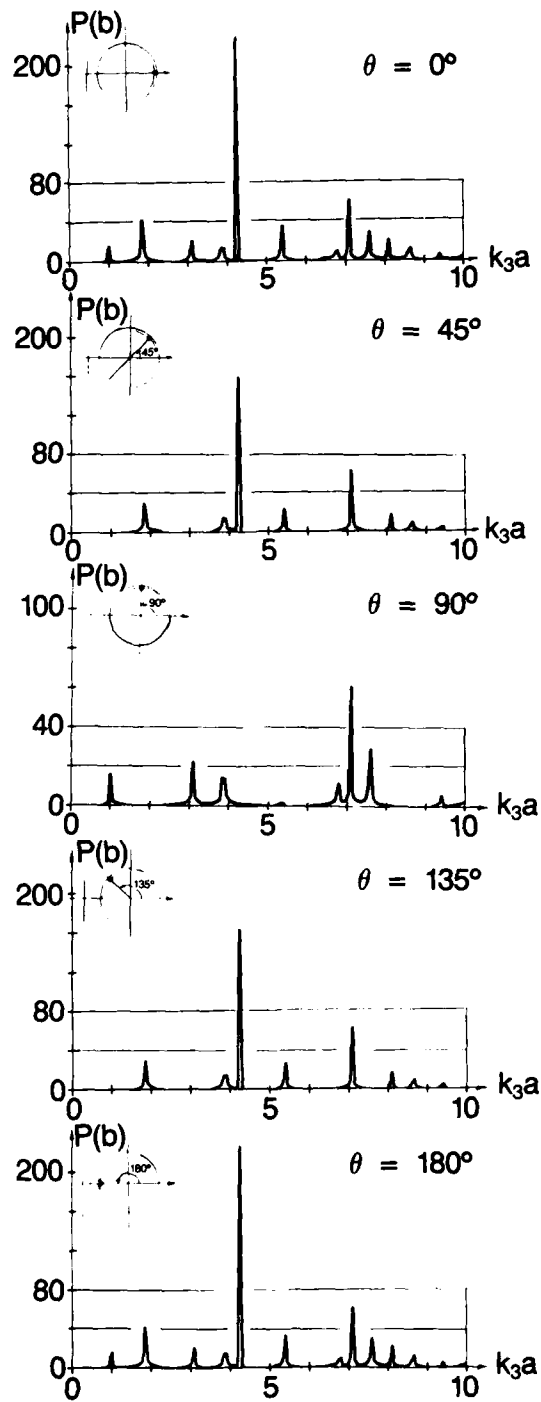


FIGURE 8a. INTERIOR PRESSURE LEVELS, $|p_3/p_0|$, VERSUS k_3a , AT FIVE (OF ELEVEN) POINTS INSIDE A SUBMERGED CYLINDRICAL SHELL LOADED WITH LOAD NO. 1, AND INSONIFIED BY AN INCIDENT PLANE WAVE

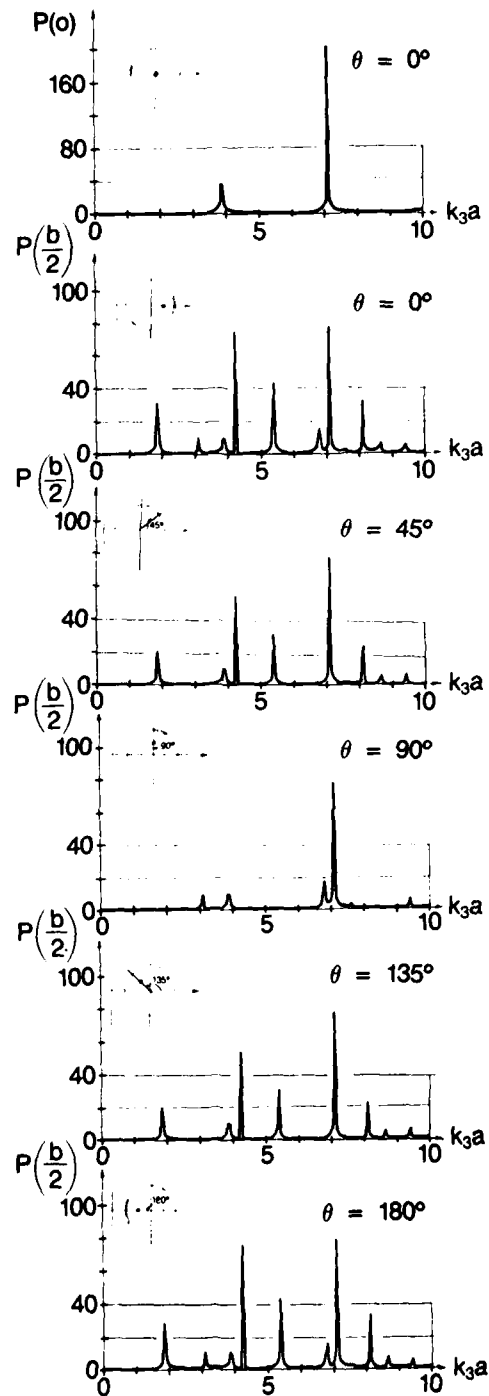


FIGURE 8b. INTERIOR PRESSURE LEVELS, $|p_3/p_0|$, VERSUS k_3a , AT FIVE (OF ELEVEN) POINTS INSIDE A SUBMERGED CYLINDRICAL SHELL LOADED WITH LOAD NO. 1, AND INSONIFIED BY AN INCIDENT PLANE WAVE

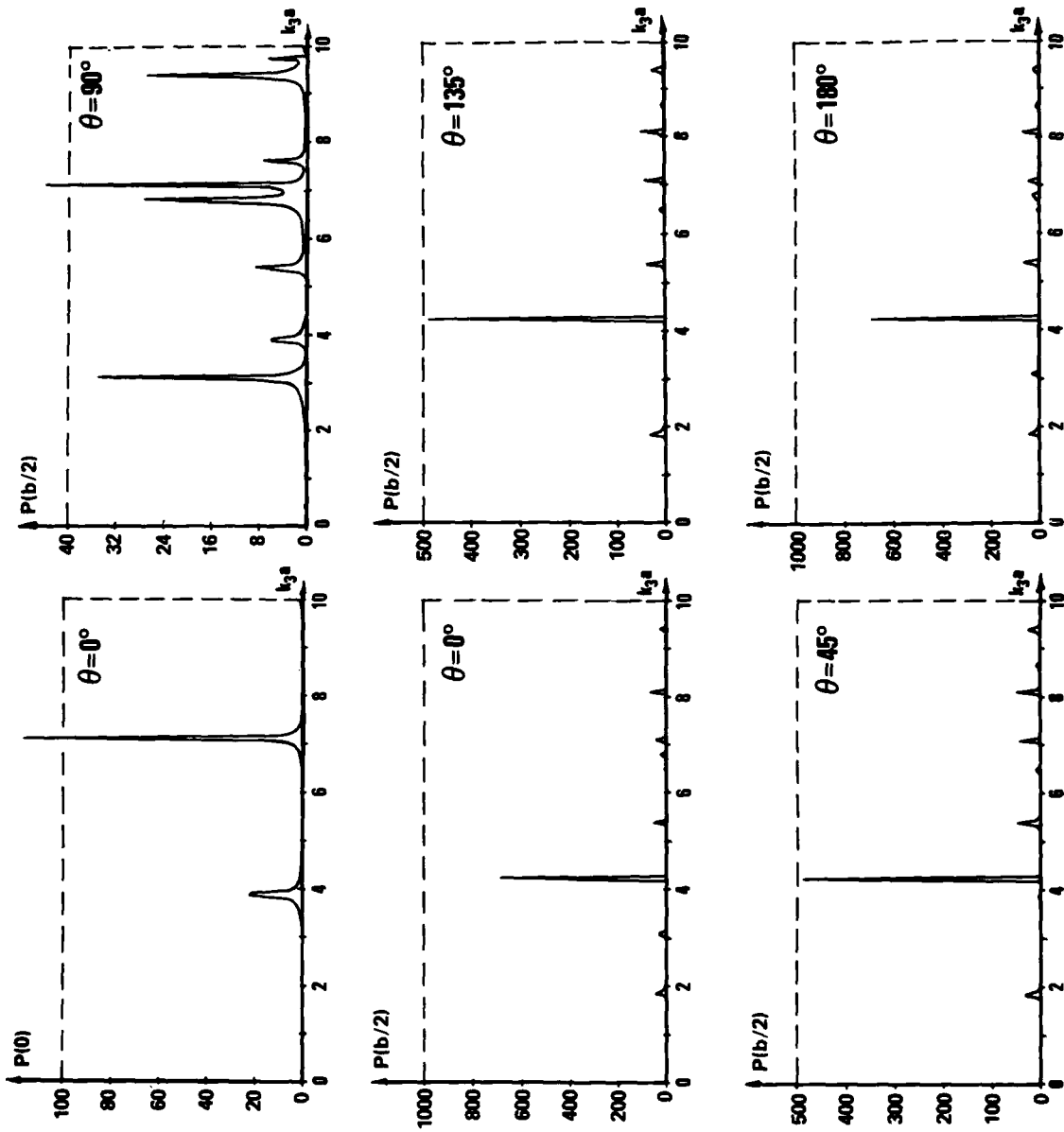


FIGURE 9a. INTERIOR PRESSURE LEVELS P_3/P_0 VERSUS $k_3 a$ AT SIX (OF ELEVEN) POINTS INSIDE A SUBMERGED CYLINDRICAL SHELL, LOADED WITH LOAD NO. 2, AND INSONIFIED BY AN INCIDENT PLANE WAVE

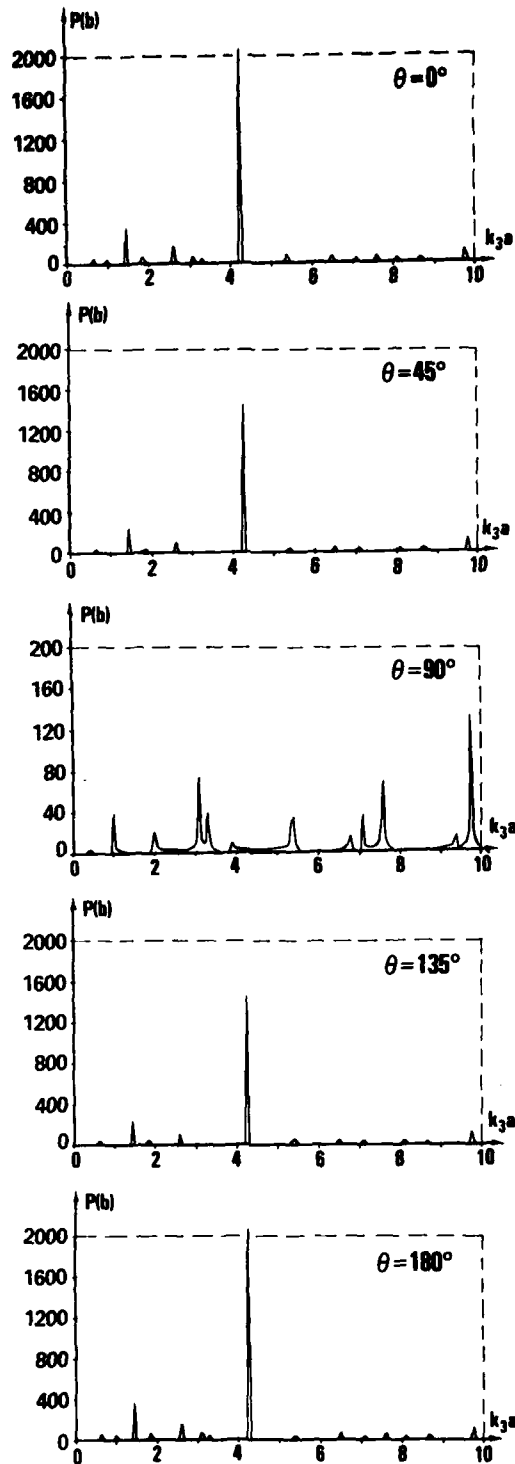


FIGURE 9b. INTERIOR PRESSURE LEVELS P_3/P_0 VERSUS $k_3 a$ AT SIX (OF ELEVEN) POINTS INSIDE A SUBMERGED CYLINDRICAL SHELL, LOADED WITH LOAD NO. 2, AND INSONIFIED BY AN INCIDENT PLANE WAVE

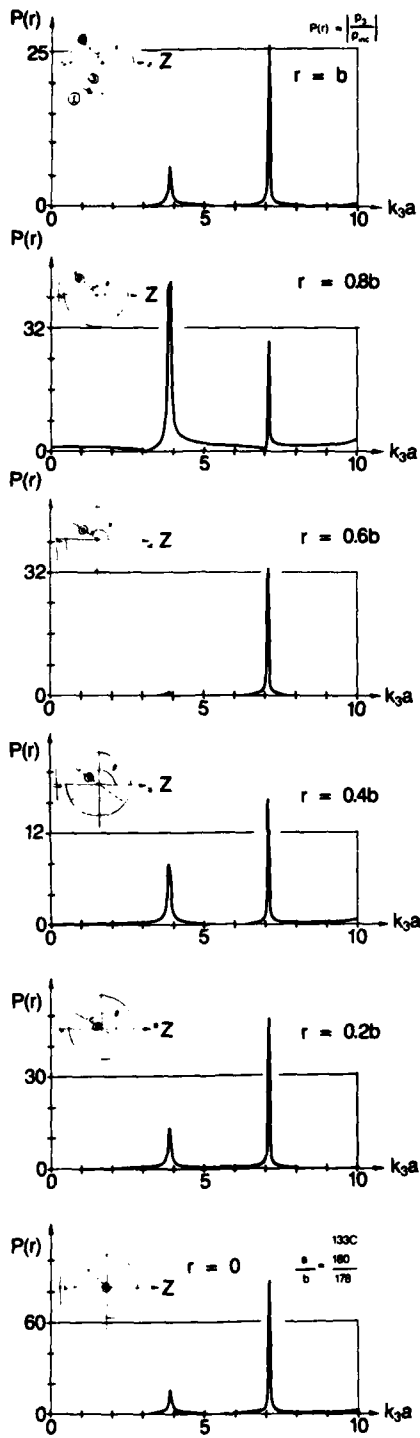


FIGURE 10. INTERIOR SPL, $\left| \frac{P_3}{P_0} \right|$, VERSUS k_3a , COMPUTED AT SIX RADIAL LOCATIONS INSIDE AN UNLOADED CYLINDRICAL SHELL, FOR ITS MONOPOLE ($n = 0$) MODE

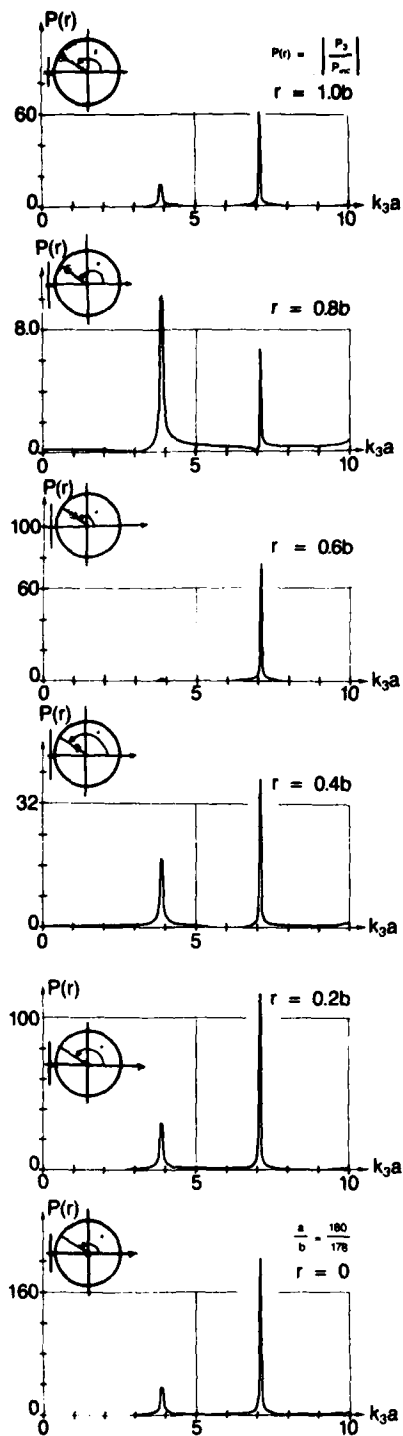


FIGURE 11. INTERIOR SPL, $\left| \frac{P_3}{P_0} \right|$, VERSUS k_3a , COMPUTED AT SIX RADIAL LOCATIONS INSIDE A CYLINDRICAL SHELL LOADED WITH LOAD NO. 1, FOR ITS MONOPOLE ($n = 0$) MODE

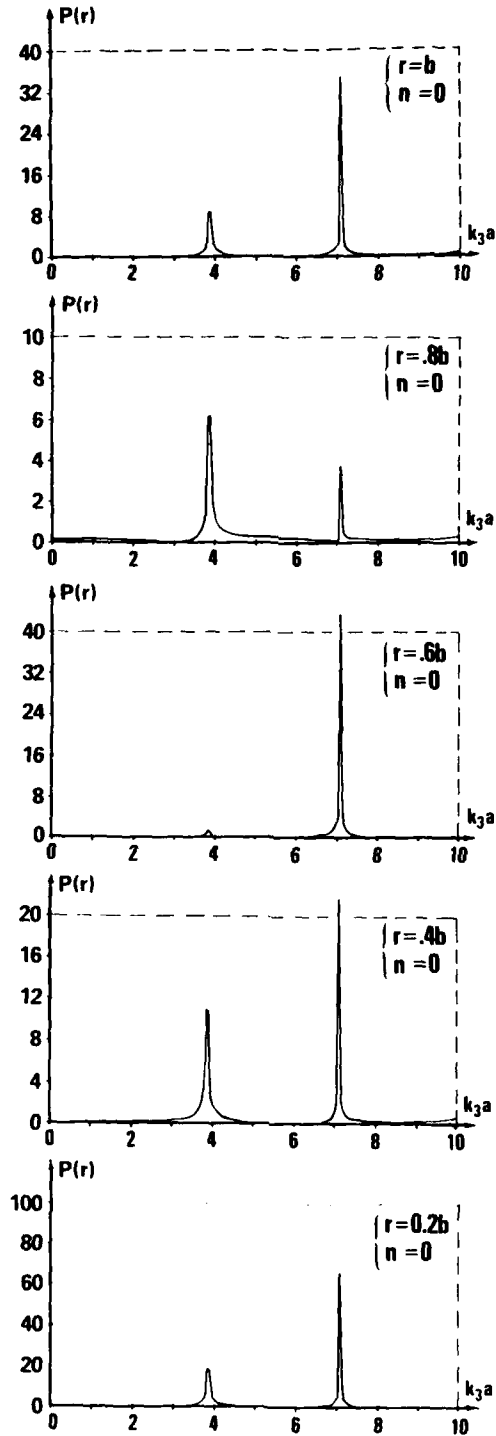


FIGURE 12. INTERIOR SPL, $|P_3/P_0|$, VERSUS k_3a , AT FIVE RADIAL LOCATIONS INSIDE A CYLINDRICAL SHELL LOADED WITH LOAD NO. 2, FOR ITS MONOPOLE ($n=0$) MODE

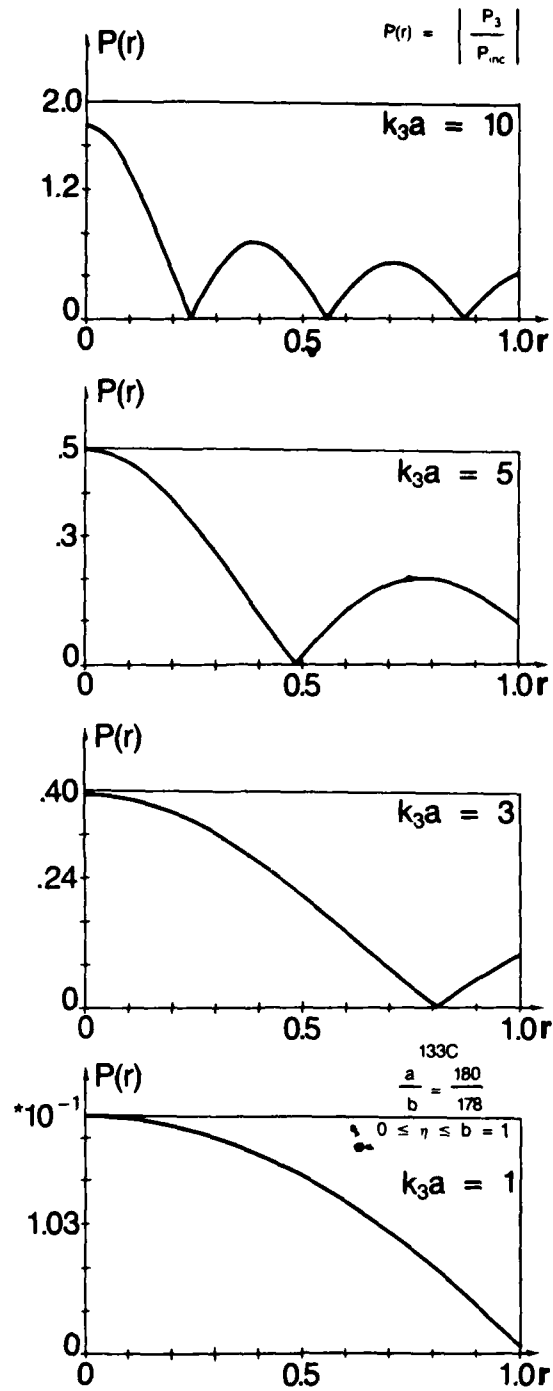


FIGURE 13. RADIAL DEPENDENCE OF THE INTERNAL SPL, $|P_3/P_0|$, FOR THE MONOPOLE ($n = 0$) MODE OF AN UNLOADED CYLINDRICAL SHELL AT FOUR FREQUENCIES SUCH THAT $k_3 a = 1, 3, 5$ AND 10

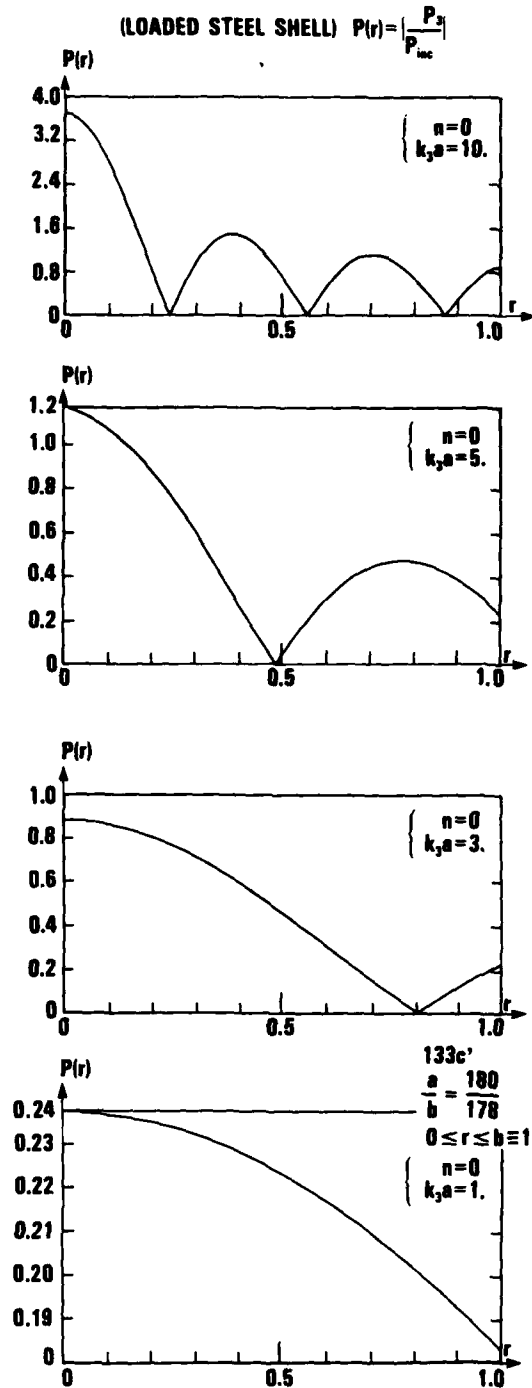


FIGURE 14. RADIAL DEPENDENCE OF THE INTERNAL SPL, $\left| \frac{P_3}{P_0} \right|$, FOR THE MONOPOLE ($n=0$) MODE OF A CYLINDRICAL SHELL LOADED WITH LOAD NO. 1, AT FOUR FREQUENCIES SUCH THAT $k_3 a = 1, 3, 5$ AND 10

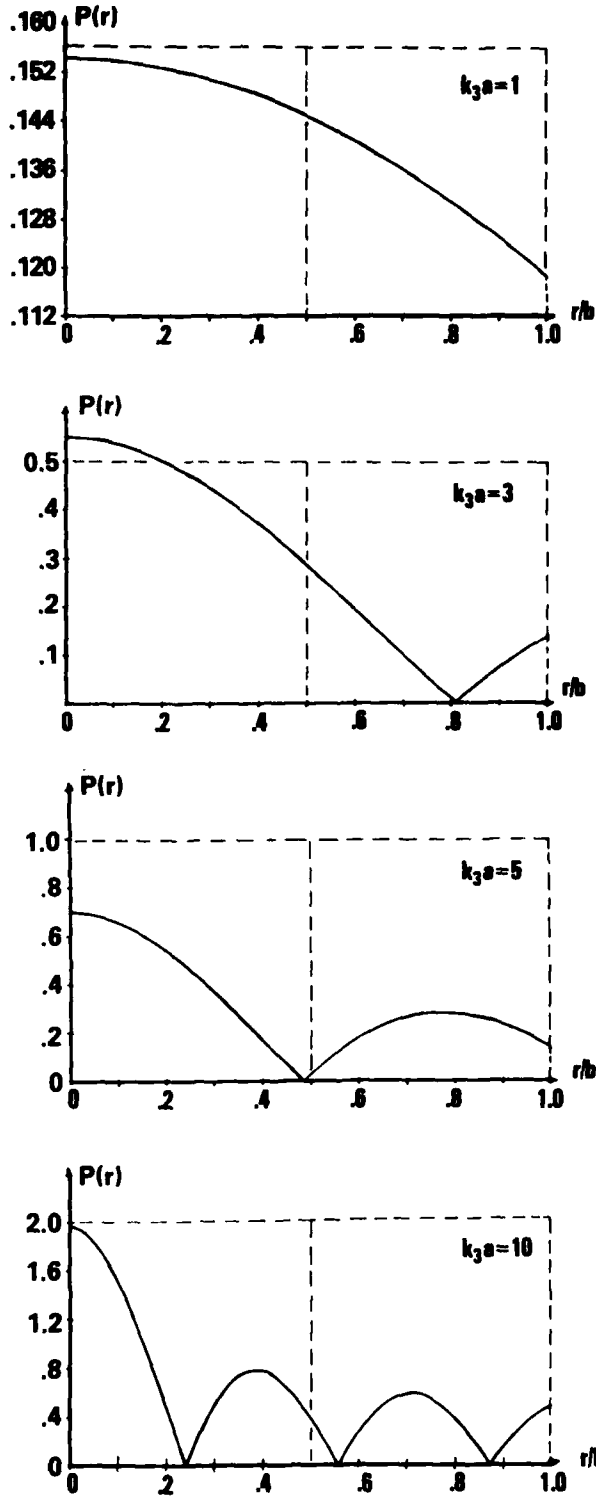


FIGURE 15. RADIAL DEPENDENCE OF THE INTERNAL SPL, $|p_3/p_0|$, FOR THE MONOPOLE ($n = 0$) MODE OF A CYLINDRICAL SHELL LOADED WITH LOAD NO. 2, AT FOUR FREQUENCIES SUCH THAT $k_3a = 1, 3, 5$ AND 10

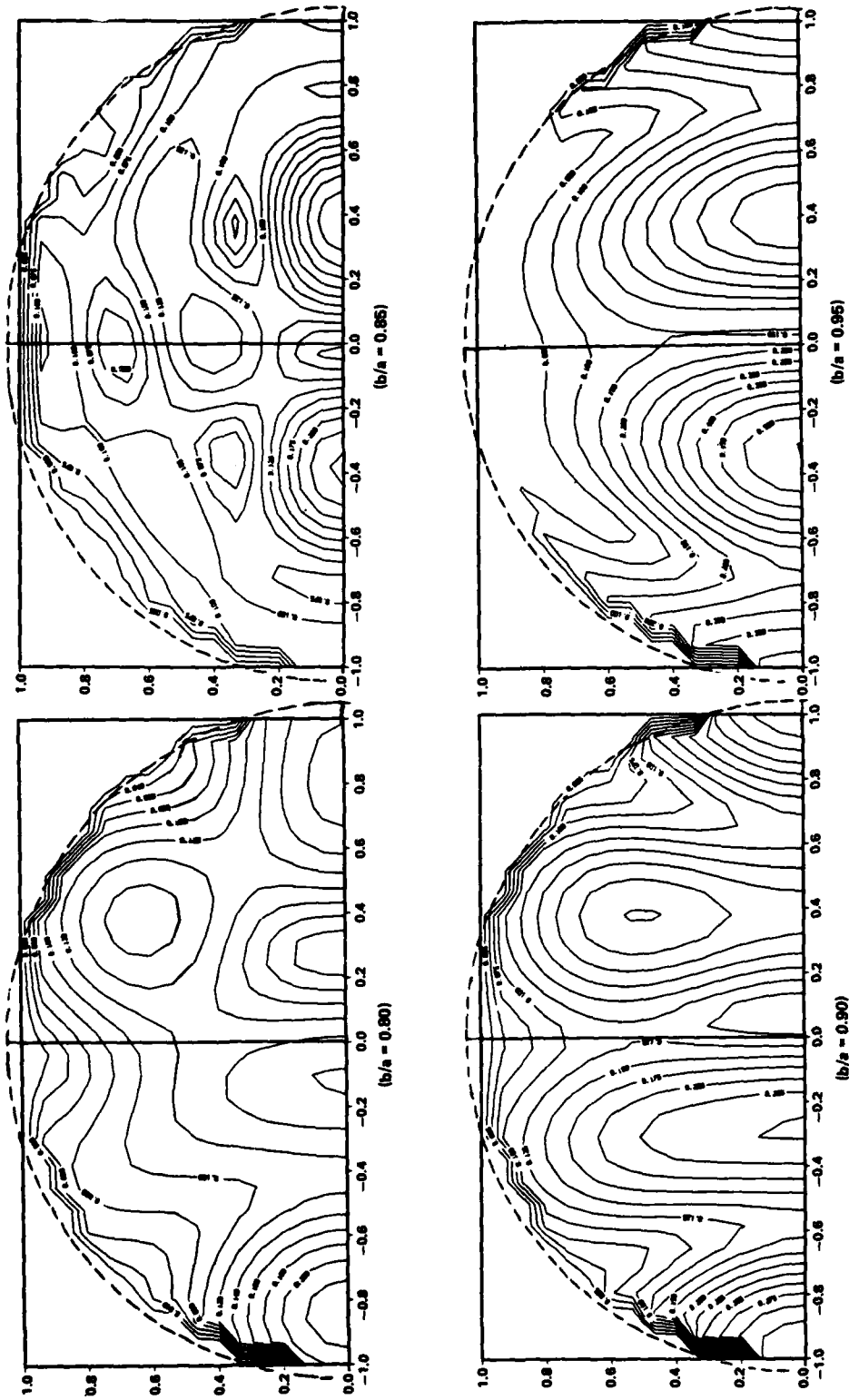


FIGURE 16. ISOBARIC CONTOUR PLOTS FOR THE INTERNALLY TRANSMITTED SOUND PRESSURE LEVELS INSIDE AN UNLOADED STEEL SHELL IN WATER AT $k_3a = 5$ FOR FOUR SHELL-THICKNESSES (i.e., $b/a = 0.80, 0.85, 0.90$ AND 0.95). THE LOCATIONS OF THE CAUSTICS ARE DETERMINED

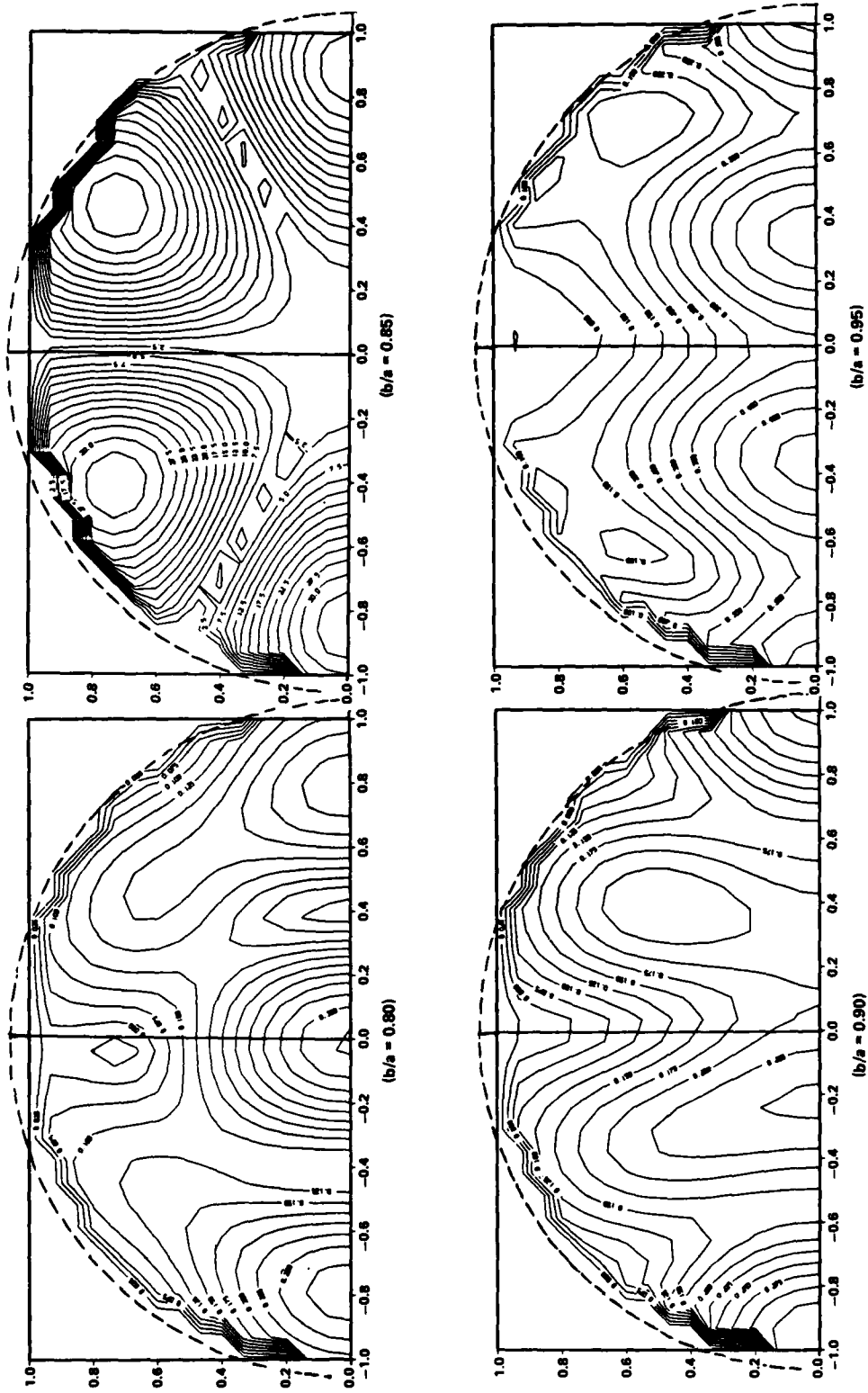


FIGURE 17. ISOBARIC CONTOUR PLOTS FOR THE INTERNALLY TRANSMITTED SOUND PRESSURE LEVELS INSIDE A STEEL SHELL IN WATER LOADED WITH LOAD NO. 1 AT $k_{3a} = 5$, FOR FOUR SHELL-THICKNESSES (i.e., $b/a = 0.80, 0.85, 0.90$ AND 0.95)

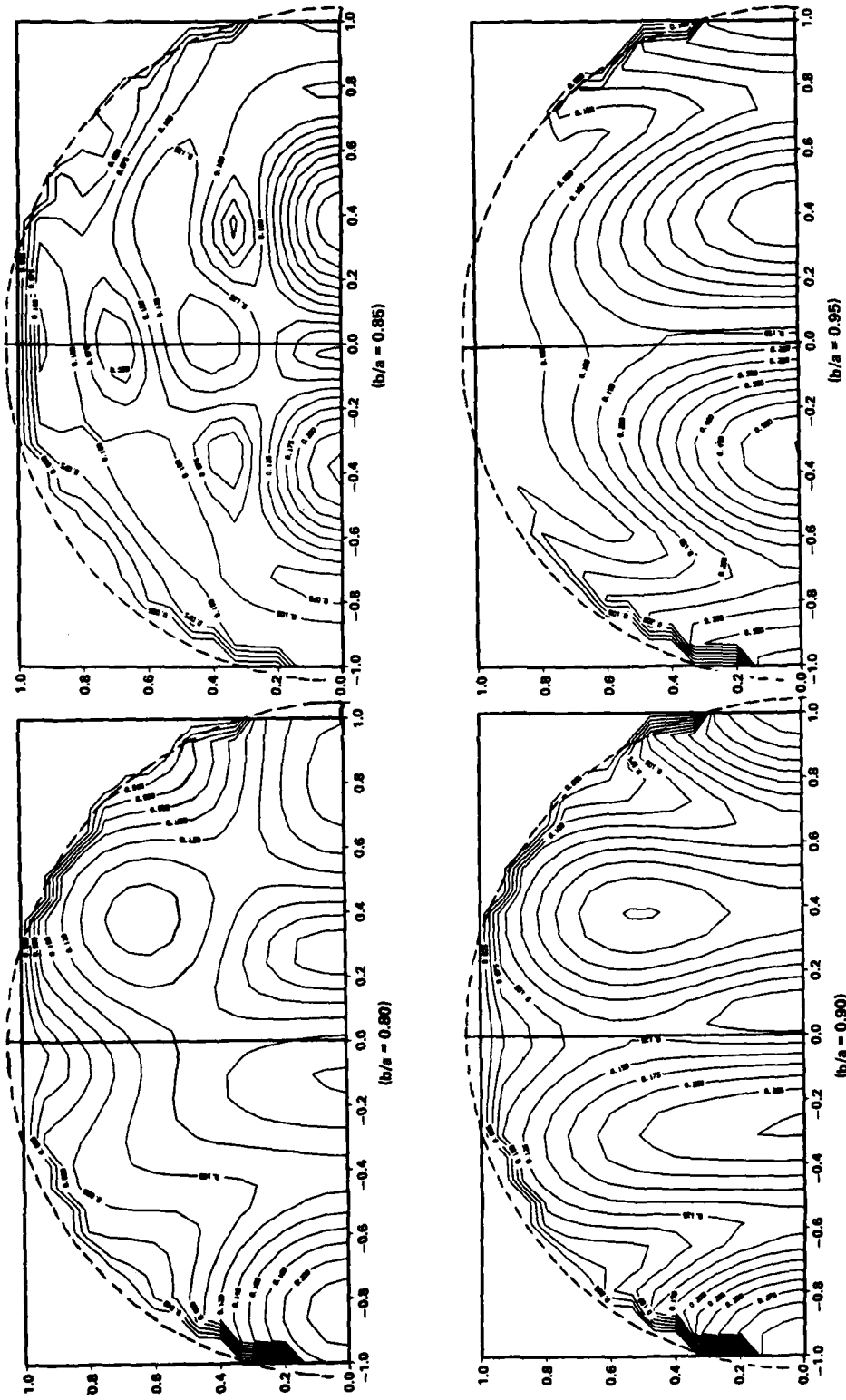


FIGURE 16. ISOBARIC CONTOUR PLOTS FOR THE INTERNALLY TRANSMITTED SOUND PRESSURE LEVELS INSIDE AN UNLOADED STEEL SHELL IN WATER AT $k_2 a = 5$ FOR FOUR SHELL-THICKNESSES (i.e., $b/a = 0.80, 0.85, 0.90$ AND 0.95). THE LOCATIONS OF THE CAUSTICS ARE DETERMINED

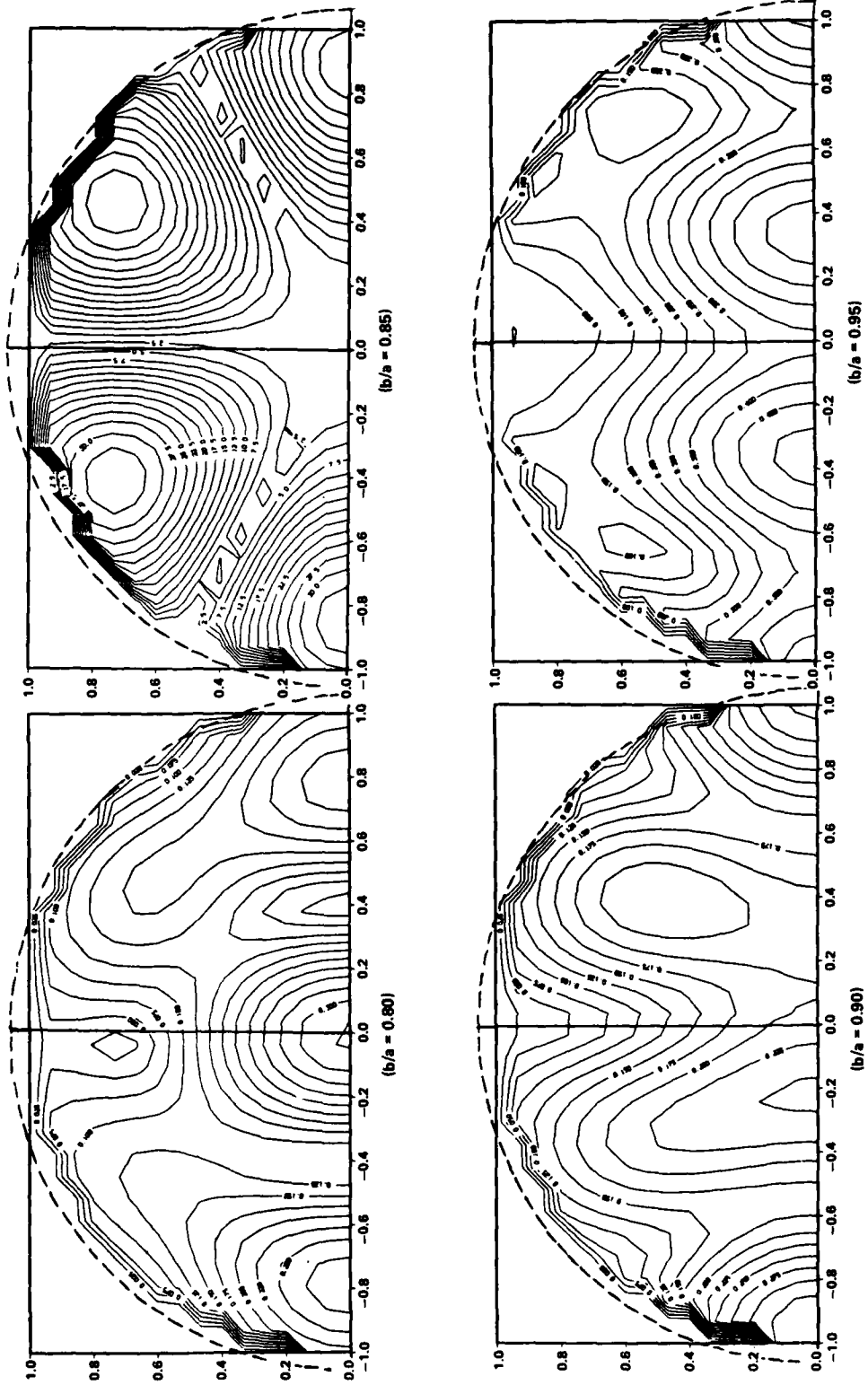


FIGURE 17. ISOBARIC CONTOUR PLOTS FOR THE INTERNALLY TRANSMITTED SOUND PRESSURE LEVELS INSIDE A STEEL SHELL IN WATER LOADED WITH LOAD NO. 1 AT $k_{3a} = 5$, FOR FOUR SHELL-THICKNESSES (i.e., $b/a = 0.80, 0.85, 0.90$ AND 0.95)

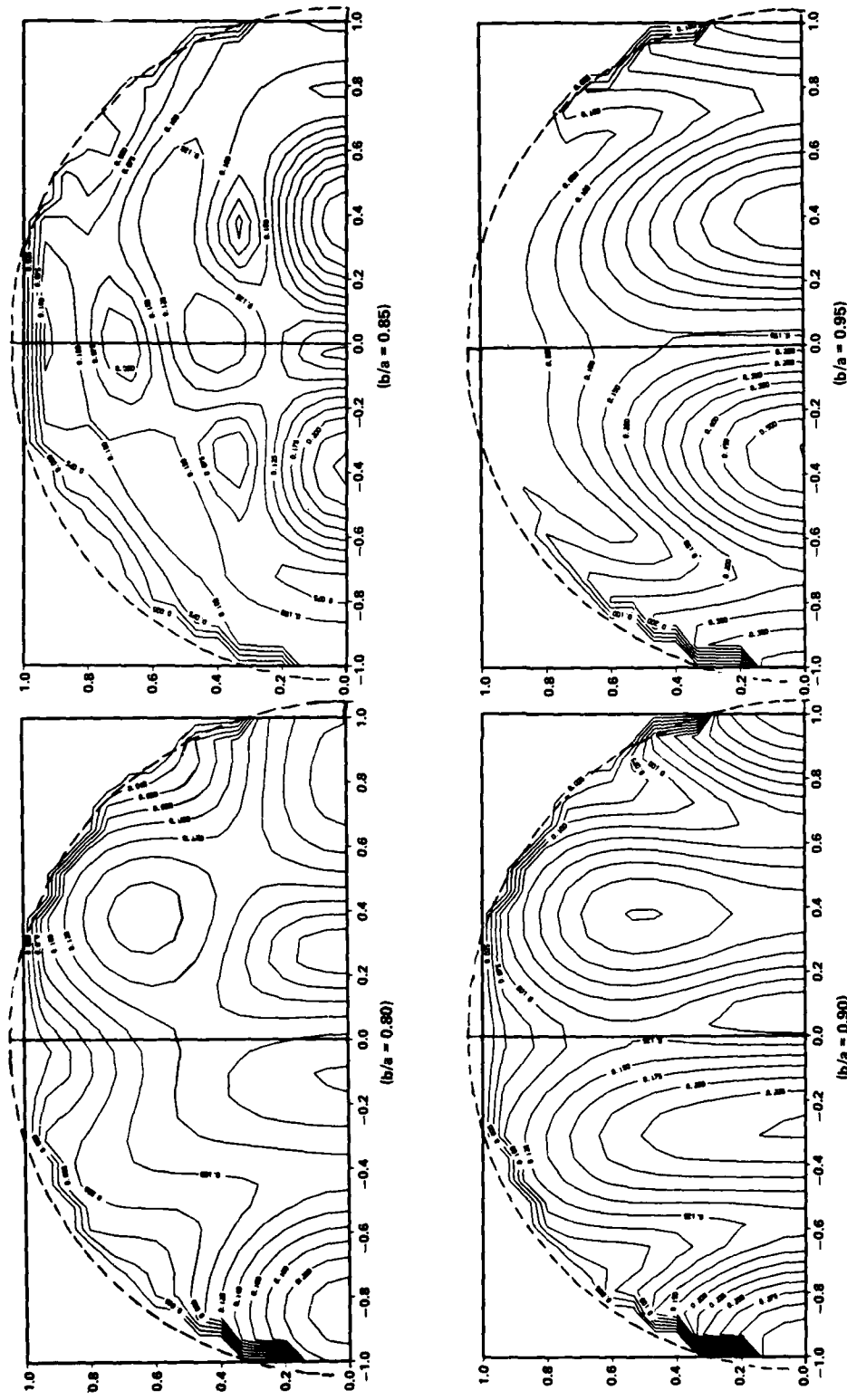


FIGURE 16. ISOBARIC CONTOUR PLOTS FOR THE INTERNALLY TRANSMITTED SOUND PRESSURE LEVELS INSIDE AN UNLOADED STEEL SHELL IN WATER AT $k_3a = 5$ FOR FOUR SHELL-THICKNESSES (i.e., $b/a = 0.80, 0.85, 0.90$ AND 0.95). THE LOCATIONS OF THE CAUSTICS ARE DETERMINED

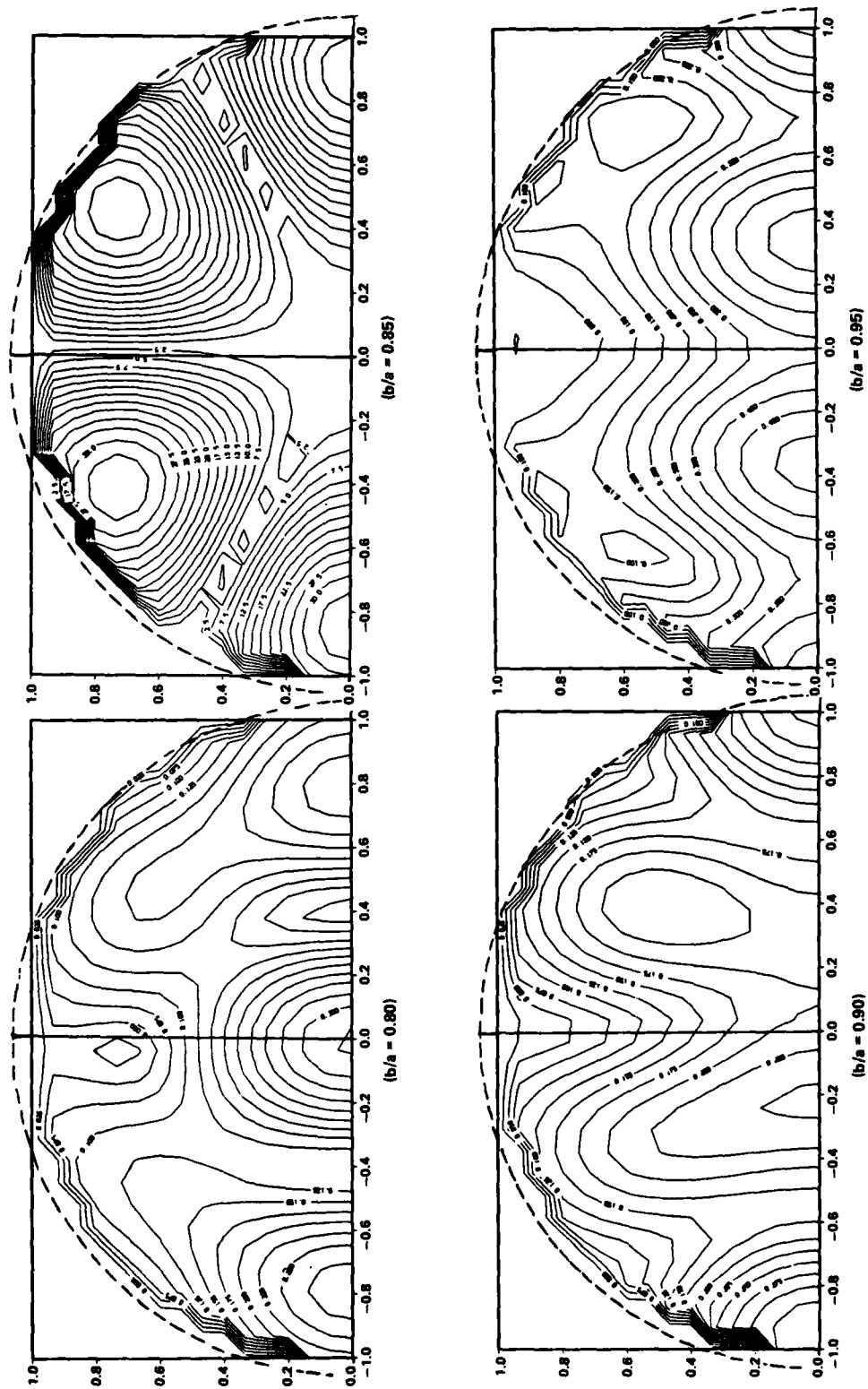


FIGURE 17. ISOBARIC CONTOUR PLOTS FOR THE INTERNALLY TRANSMITTED SOUND PRESSURE LEVELS INSIDE A STEEL SHELL IN WATER LOADED WITH LOAD NO. 1 AT $k_3a = 5$, FOR FOUR SHELL-THICKNESSES (i.e., $b/a = 0.80, 0.85, 0.90$ AND 0.95)

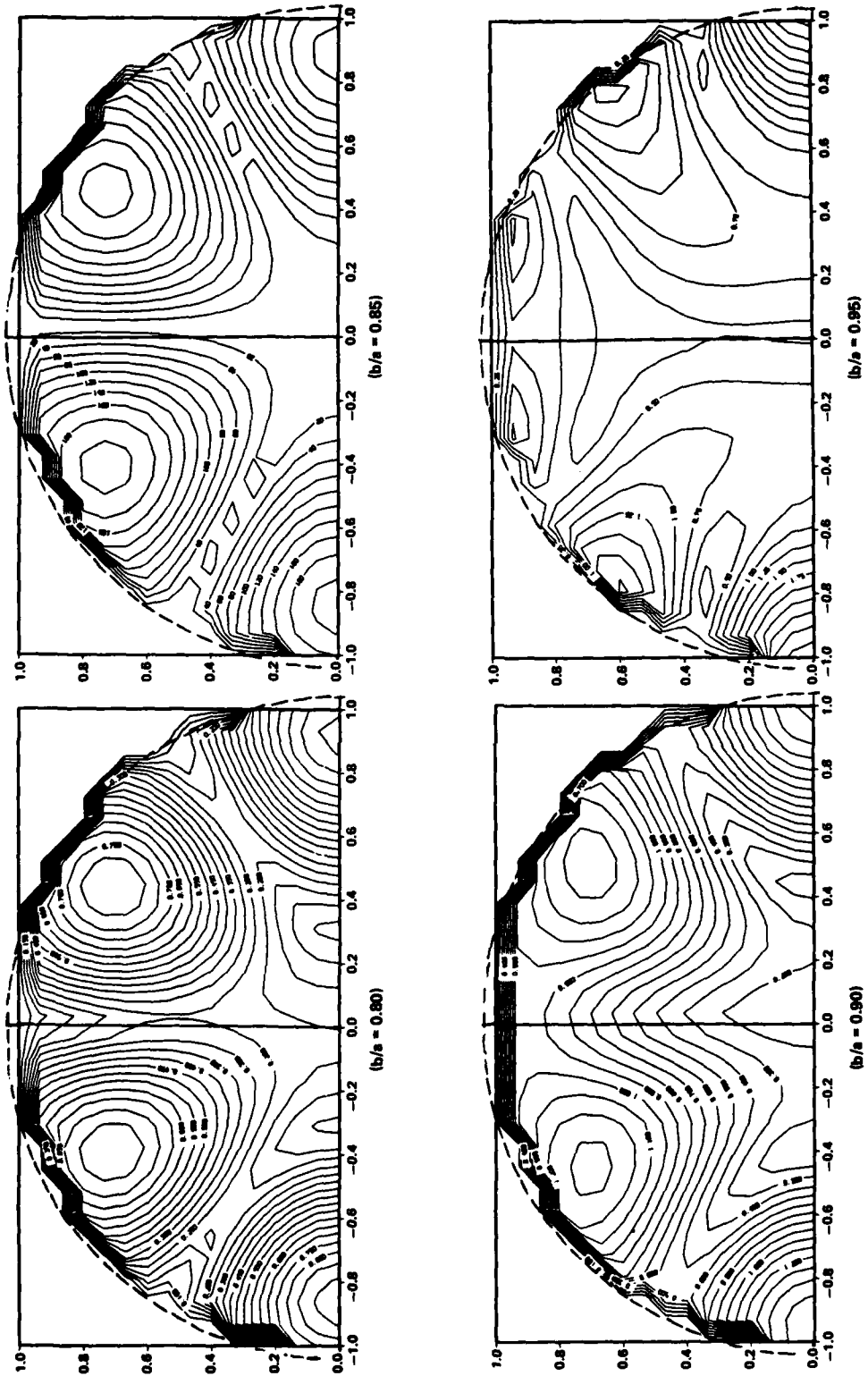


FIGURE 18. ISOBARIC CONTOUR PLOTS FOR THE INTERNALLY TRANSMITTED SOUND PRESSURE LEVELS INSIDE A STEEL SHELL IN WATER LOADED WITH LOAD NO. 2 AT $k_3 a = 5$, FOR FOUR SHELL-THICKNESSES (i.e., $b/a = 0.80, 0.85, 0.90$ AND 0.95)

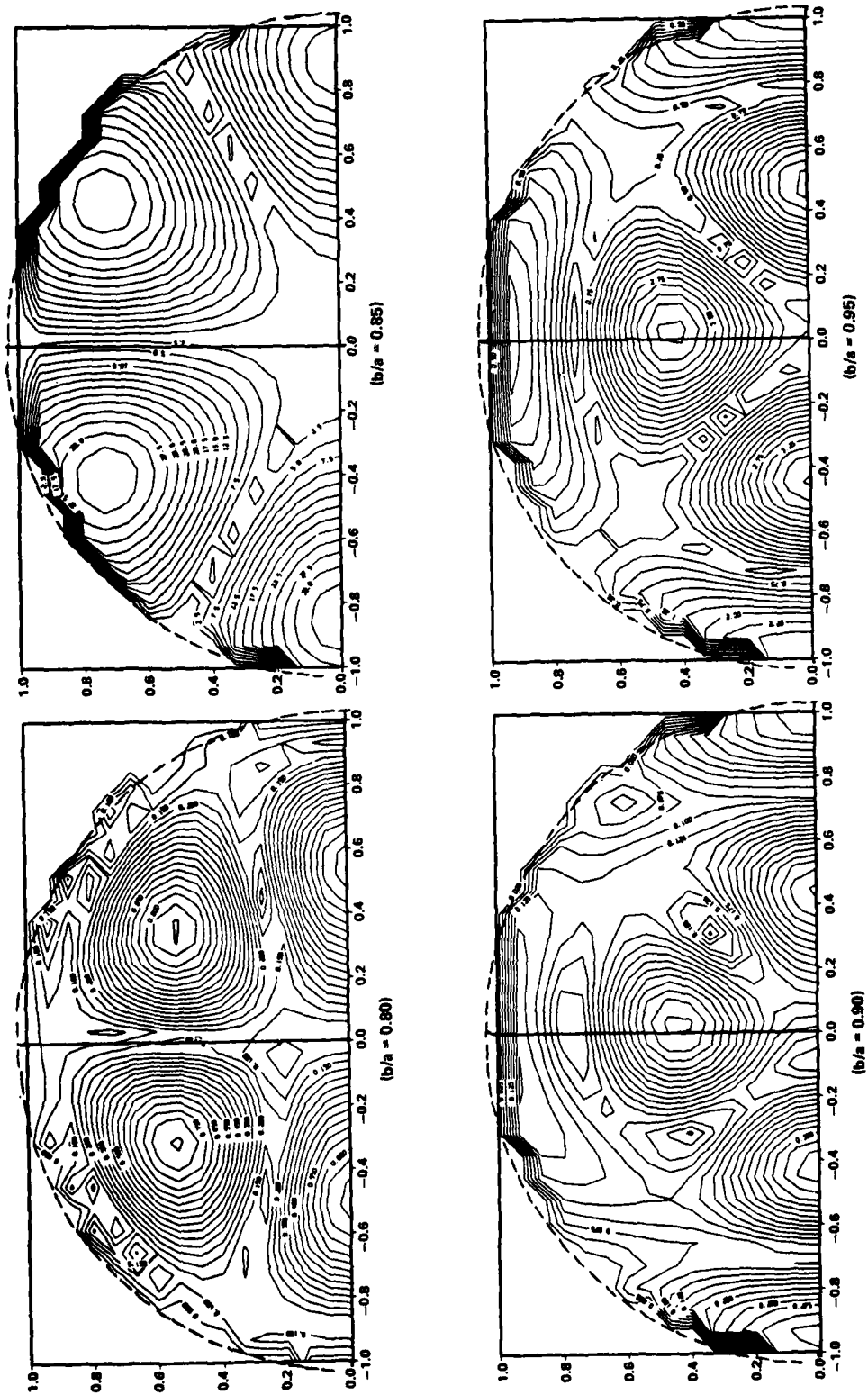


FIGURE 19. ISOBARIC CONTOUR PLOTS FOR THE INTERNALLY TRANSMITTED SOUND PRESSURE LEVELS INSIDE AN UNLOADED STEEL SHELL IN WATER AT $k_3a = 7.0$, FOR FOUR SHELL-THICKNESSES (i.e., $b/a = 0.80, 0.85, 0.90$ AND 0.95). THE LOCATIONS OF THE CAUSTICS ARE DETERMINED

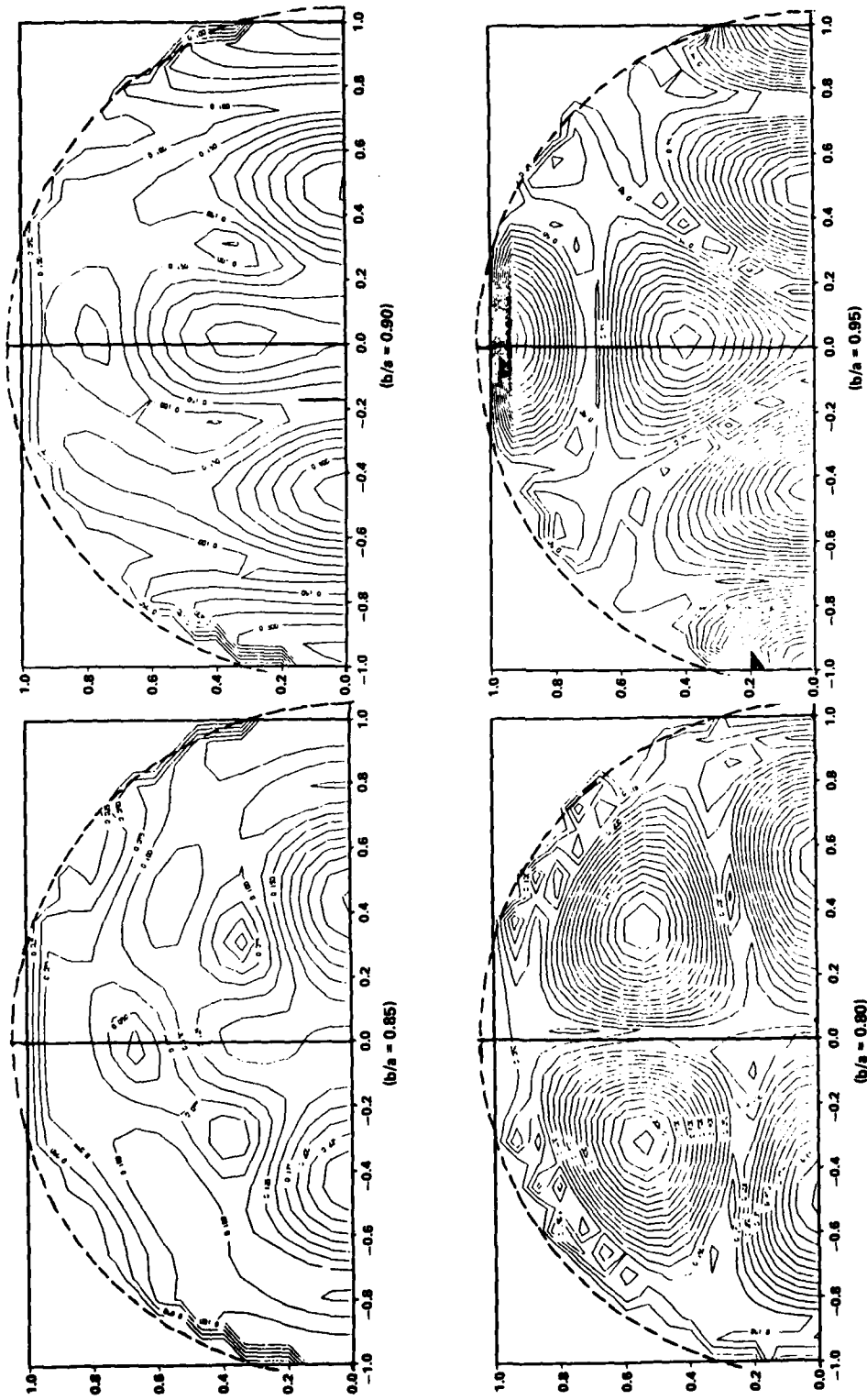


FIGURE 20. ISOBARIC CONTOUR PLOTS FOR THE INTERNALLY TRANSMITTED SOUND PRESSURE LEVELS INSIDE A STEEL SHELL IN WATER LOADED WITH LOAD NO. 1, AT $k_3 a = 7.0$, FOR FOUR SHELL-THICKNESSES (i.e., $b/a = 0.80, 0.85, 0.90$ AND 0.95)

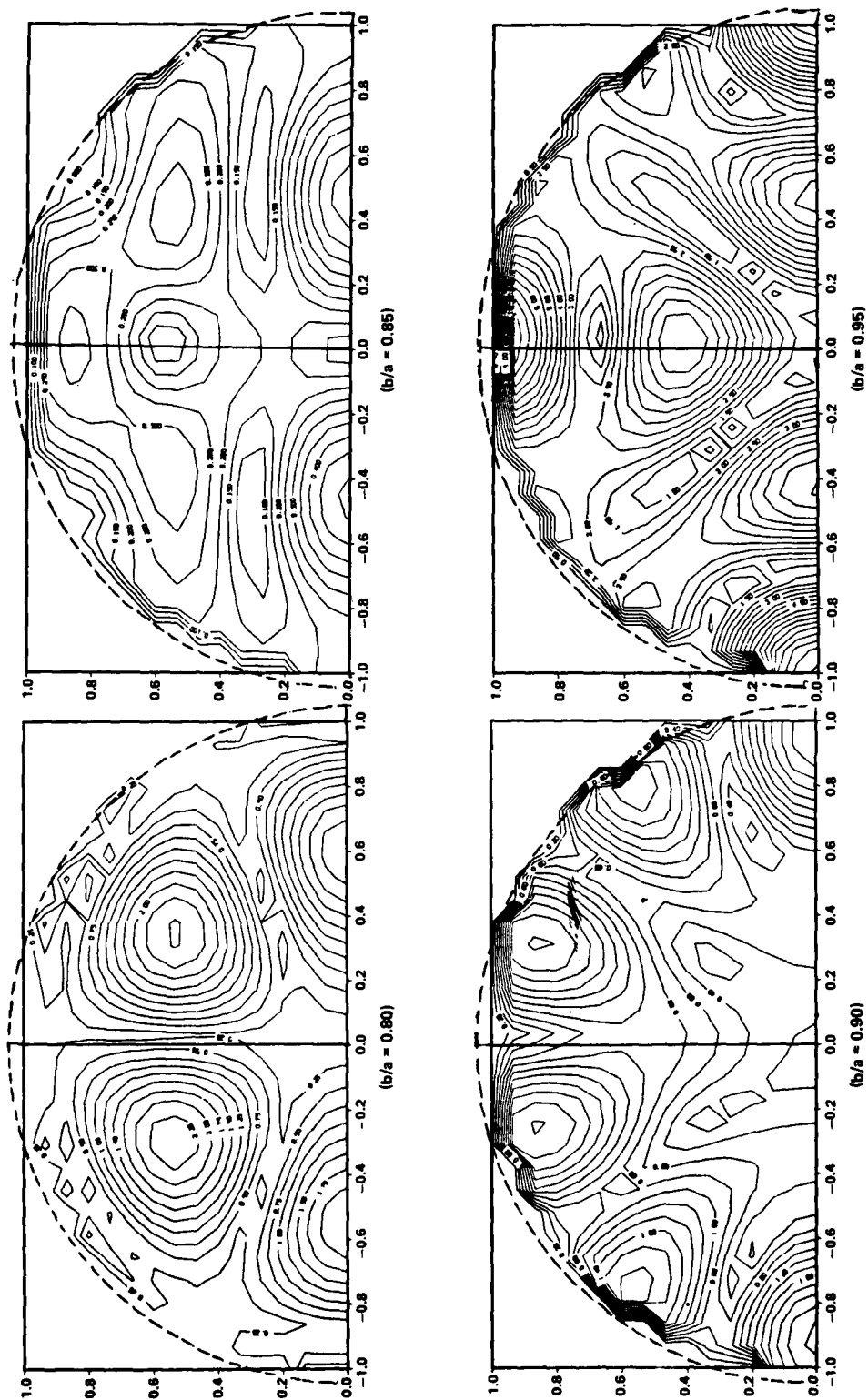


FIGURE 21. ISOBARIC CONTOUR PLOTS FOR THE INTERNALLY TRANSMITTED SOUND PRESSURE LEVELS INSIDE A STEEL SHELL IN WATER LOADED WITH LOAD NO. 2 AT $k_3 a = 7.0$, FOR FOUR SHELL-THICKNESSES (i.e., $b/a = 0.80, 0.85, 0.90$ AND 0.95)

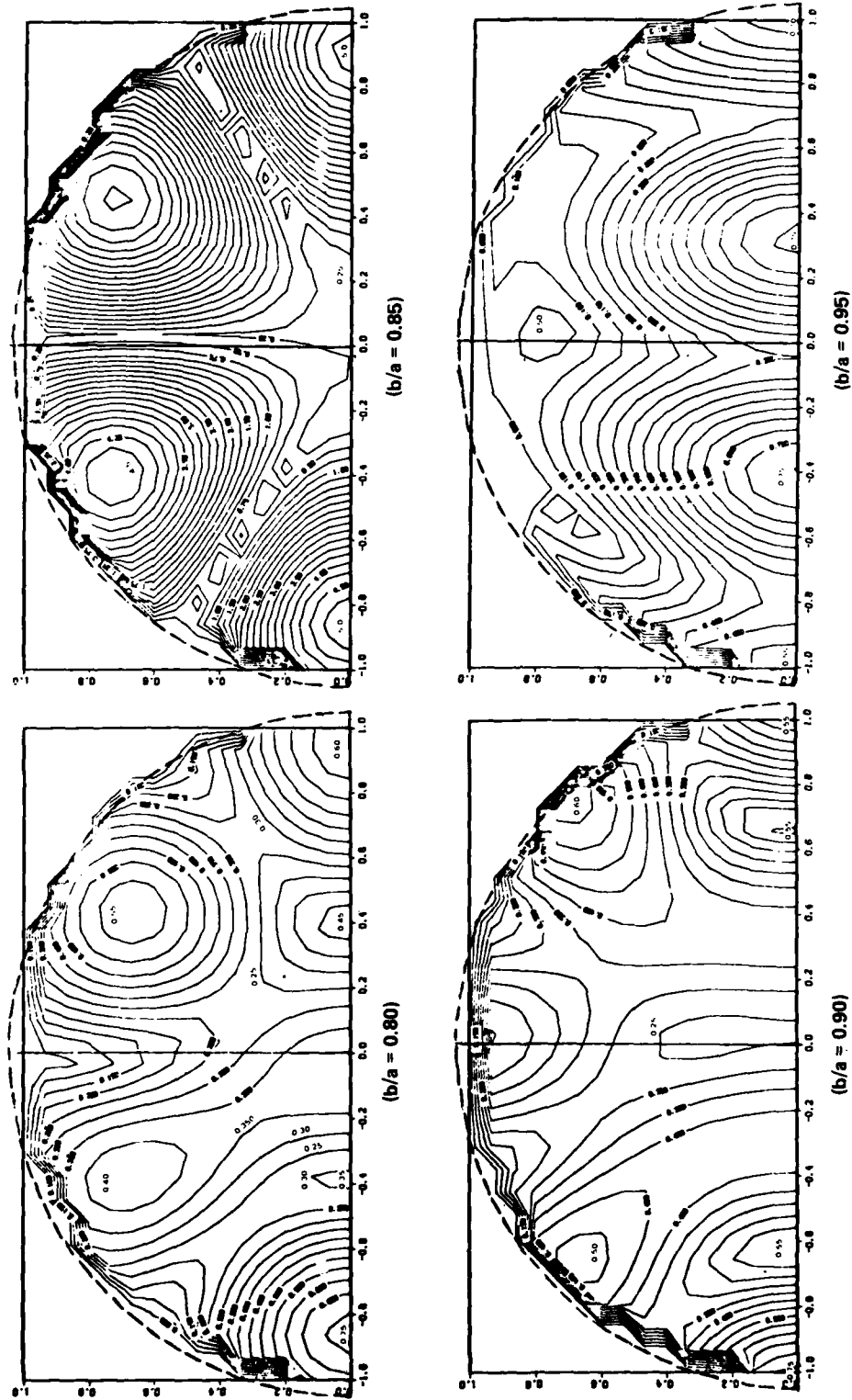


FIGURE 22. ISOBARIC CONTOUR PLOTS FOR THE INTERNALLY TRANSMITTED SOUND PRESSURE LEVELS INSIDE AN UNLOADED ALUMINUM SHELL IN WATER AT $k_0a = 5$, FOR FOUR SHELL THICKNESSES (i.e., $b/a = 0.80, 0.85, 0.90$ AND 0.95) THE LOCATIONS OF THE CAUSTICS ARE DETERMINED

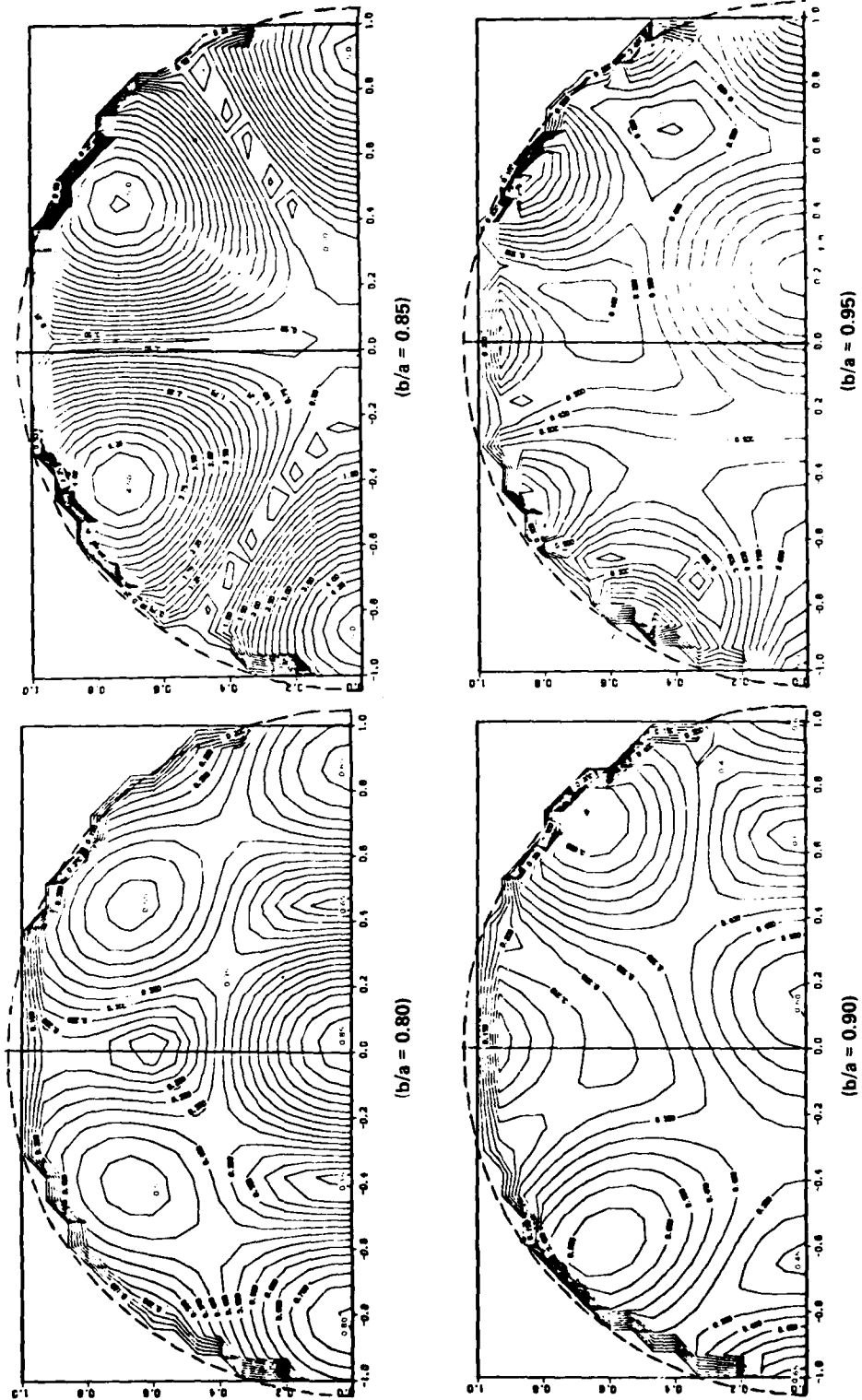
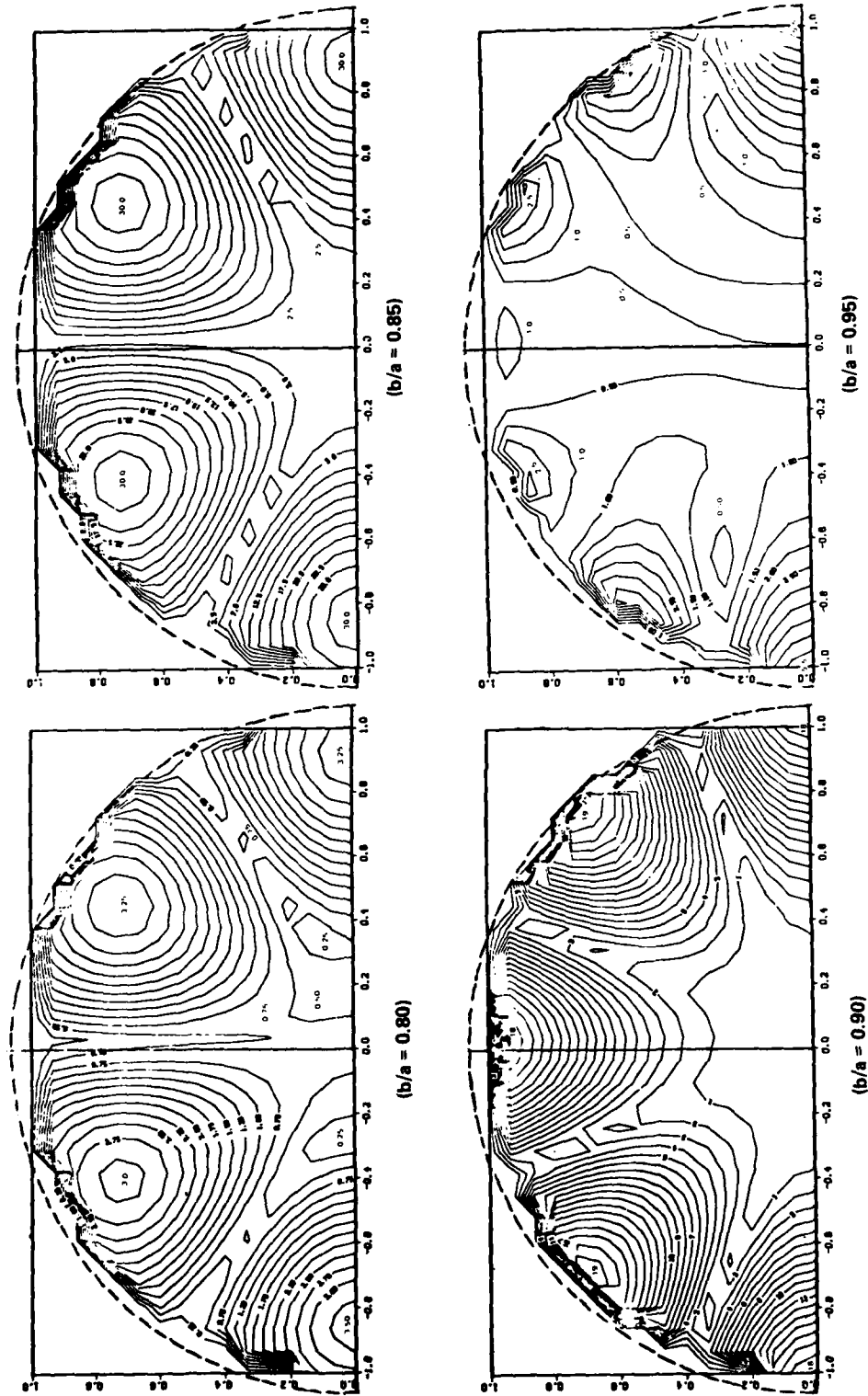


FIGURE 23. ISOBARIC CONTOUR PLOTS FOR THE INTERNALLY TRANSMITTED SOUND PRESSURE LEVELS INSIDE AN ALUMINUM SHELL IN WATER LOADED WITH LOAD NO. 1 AT $k_3 a = 5$, FOR FOUR SHELL-THICKNESSES (i.e., $b/a = 0.80, 0.85, 0.90$ AND 0.95)



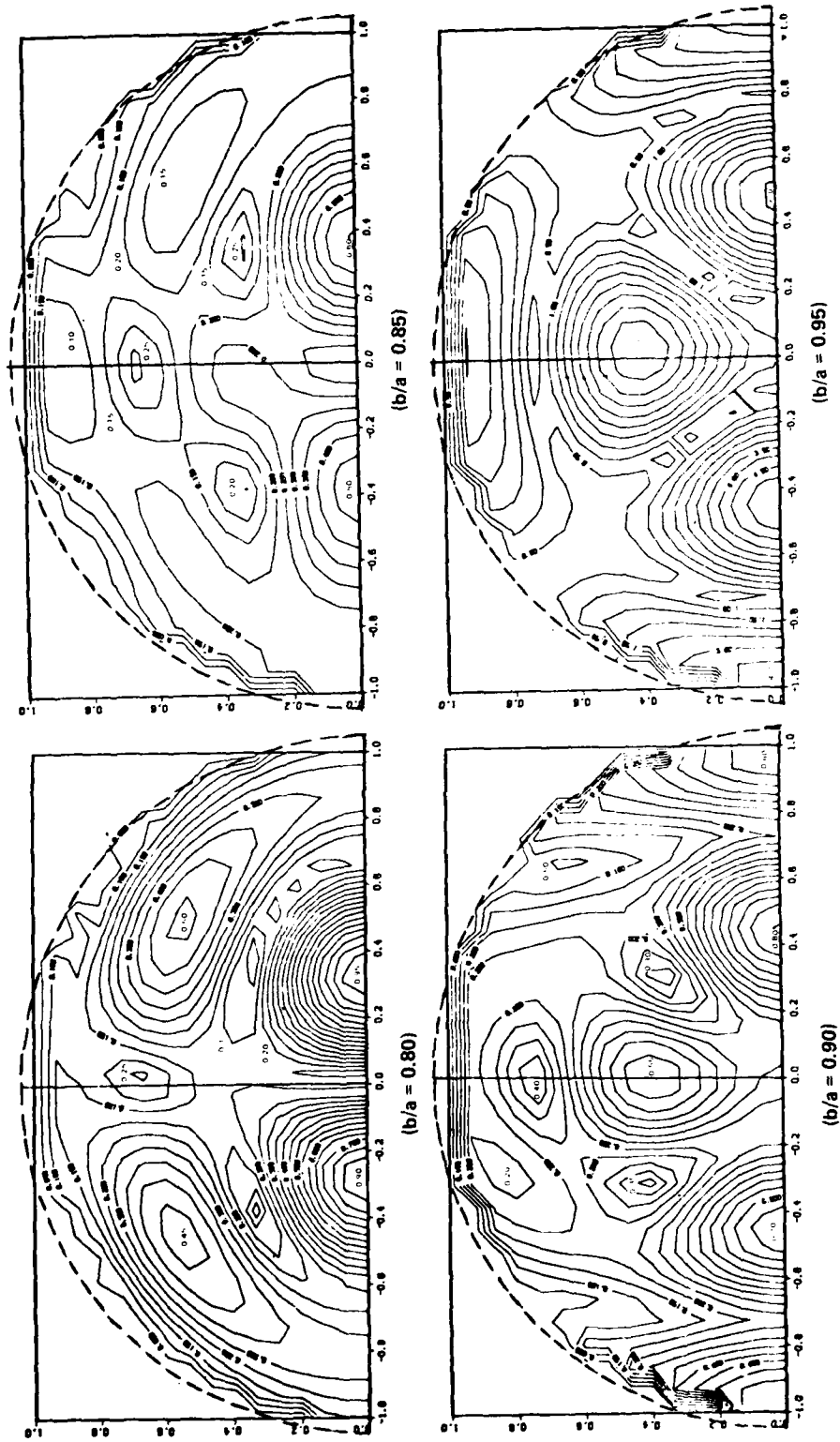


FIGURE 25. ISOBARIC CONTOUR PLOTS FOR THE INTERNALLY TRANSMITTED SOUND PRESSURE LEVELS INSIDE AN UNLOADED ALUMINUM SHELL IN WATER AT $k_0 a = 7.0$, FOR FOUR SHELL THICKNESSES (i.e., $b/a = 0.80, 0.85, 0.90$ AND 0.95). THE LOCATIONS OF THE CAUSTICS ARE DETERMINED

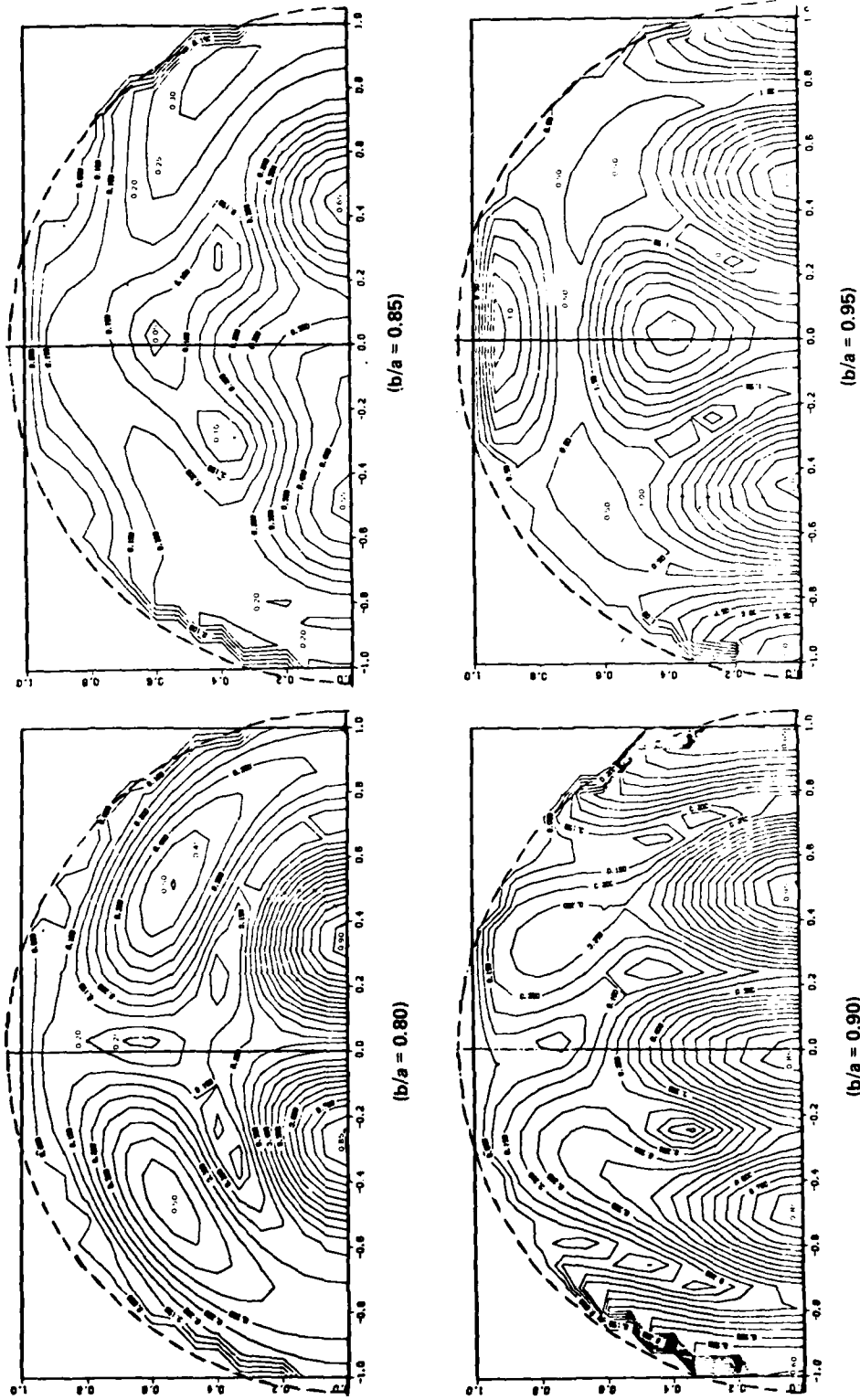


FIGURE 26. ISOBARIC CONTOUR PLOTS FOR THE INTERNALLY TRANSMITTED SOUND PRESSURE LEVELS INSIDE AN ALUMINUM SHELL IN WATER LOADED WITH LOAD NO. 1 AT $k_3a = 7.0$, FOR FOUR SHELL-THICKNESSES (i.e., $b/a = 0.80, 0.85, 0.90$ AND 0.95)

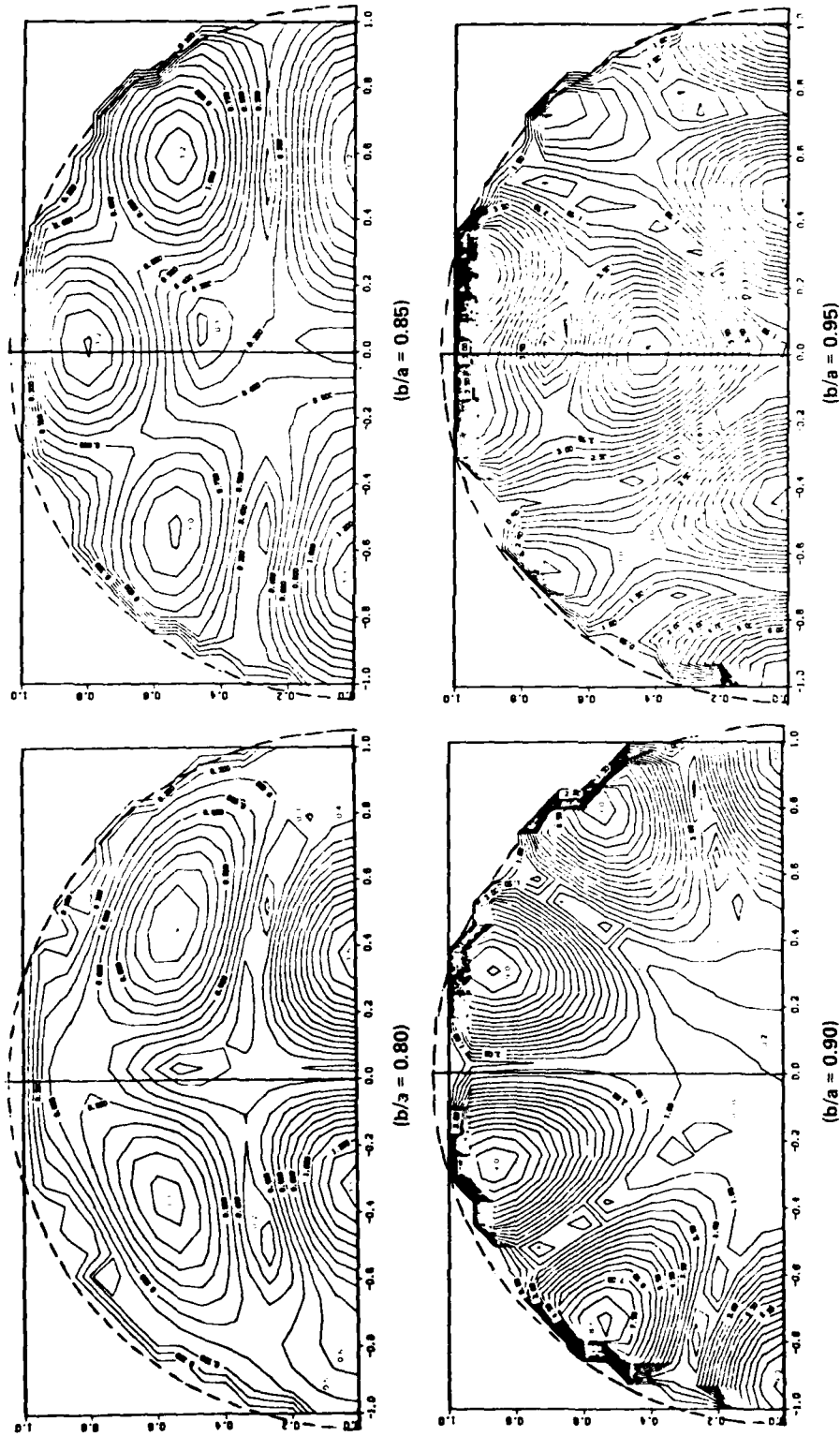


FIGURE 27. ISOBARIC CONTOUR PLOTS FOR THE INTERNALLY TRANSMITTED SOUND PRESSURE LEVELS INSIDE AN ALUMINUM SHELL IN WATER LOADED WITH LOAD NO. 2 AT $k_3 a = 7.0$, FOR FOUR SHELL-THICKNESSES (i.e., $b/a = 0.80, 0.85, 0.90$ AND 0.95)

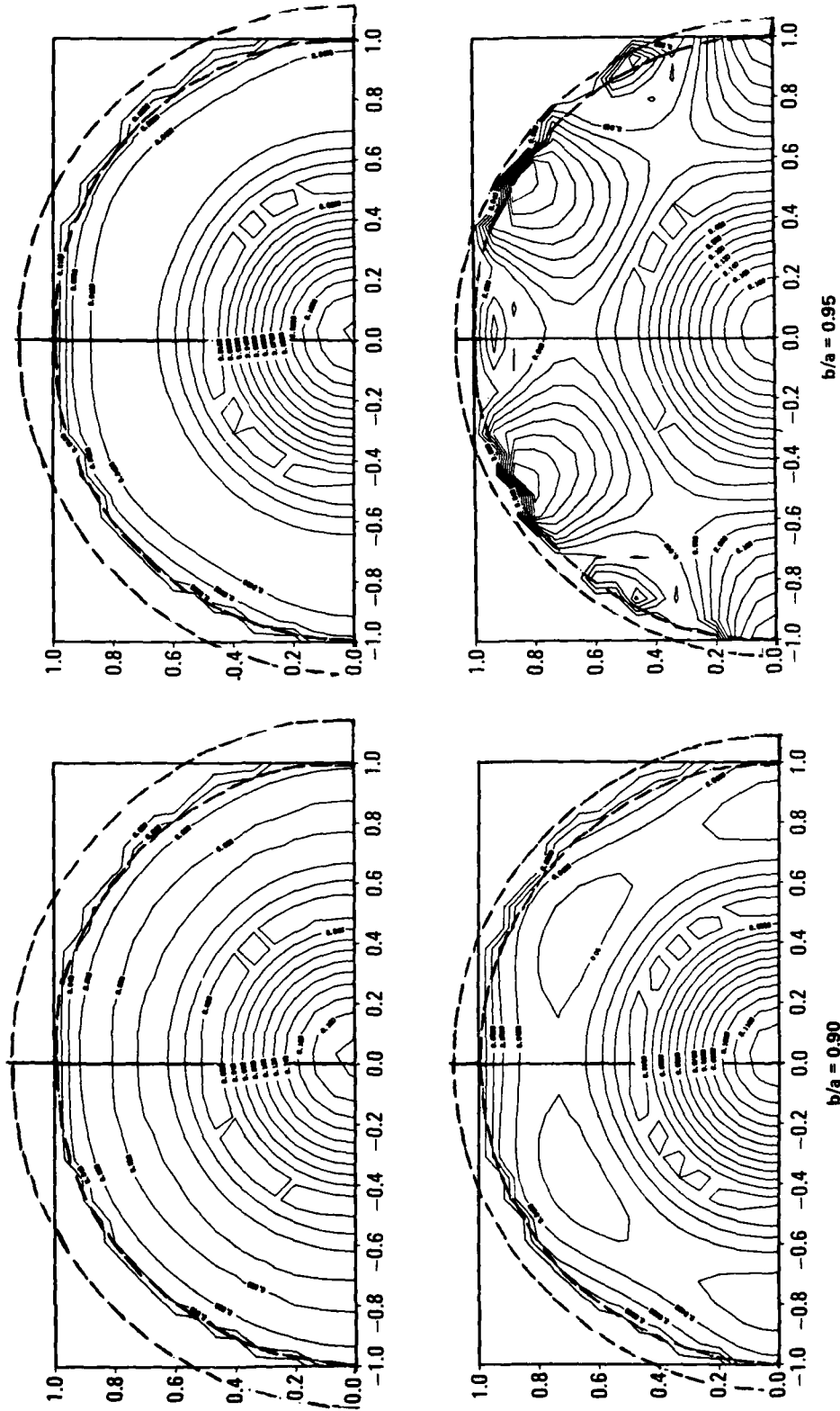


FIGURE 28. INTERNALLY TRANSMITTED ISOBARIC CONTOUR PLOTS FOR A SUBMERGED, AIR-FILLED STEEL CYLINDRICAL SHELL IN WATER. THE SYMMETRIC LOAD NO. 1 IS ACTING ON THE OUTER SURFACE OF THE SHELL. NO INCIDENT WAVE IS PRESENT HERE. FOUR SHELL THICKNESSES ARE DISPLAYED HERE: $b/a = 0.80, 0.86, 0.90, \text{ AND } 0.95$. ALL CALCULATIONS ARE DONE FOR $k_3 a = 5.0$. THIS IS THE EFFECT OF THE SURFACE LOAD ALONE AS GIVEN IN EQUATIONS (30) AND (26)

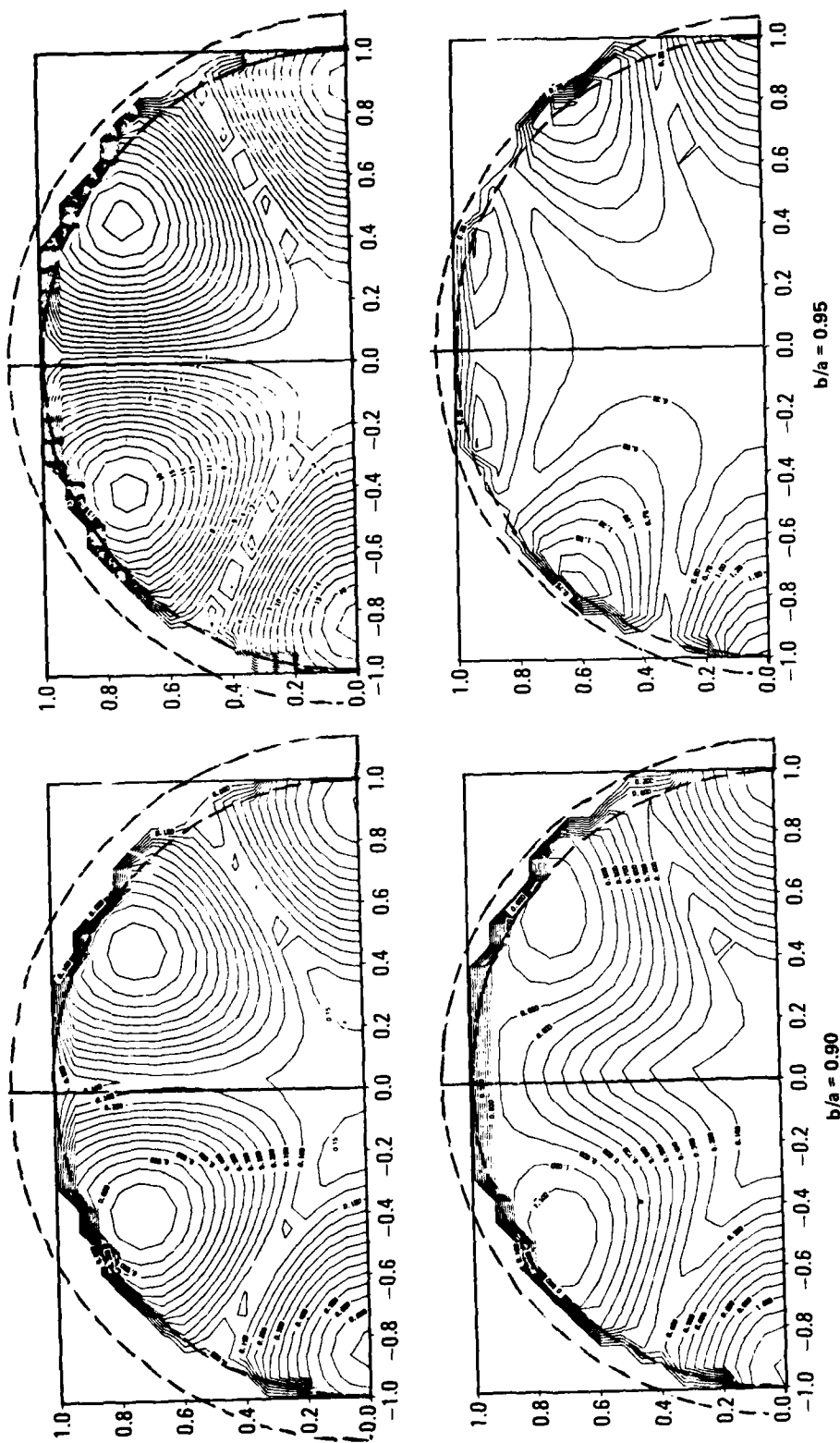


FIGURE 29. INTERNALLY TRANSMITTED ISOBARIC CONTOUR PLOTS FOR A SUBMERGED, AIR-FILLED STEEL CYLINDRICAL SHELL IN WATER. THE ASYMMETRIC LOAD NO. 2 IS ACTING ON THE STEEL SHELL. NO INCIDENT WAVE IS PRESENT HERE. FOUR SHELL-THICKNESSES ARE DISPLAYED HERE: $b/a = 0.80, 0.85, 0.90, \text{ AND } 0.95$. ALL CALCULATIONS ARE DONE FOR $k_2 a = 5.0$. THIS IS THE EFFECT OF THE SURFACE LOAD ALONE AS GIVEN IN EQUATIONS (30) AND (26)

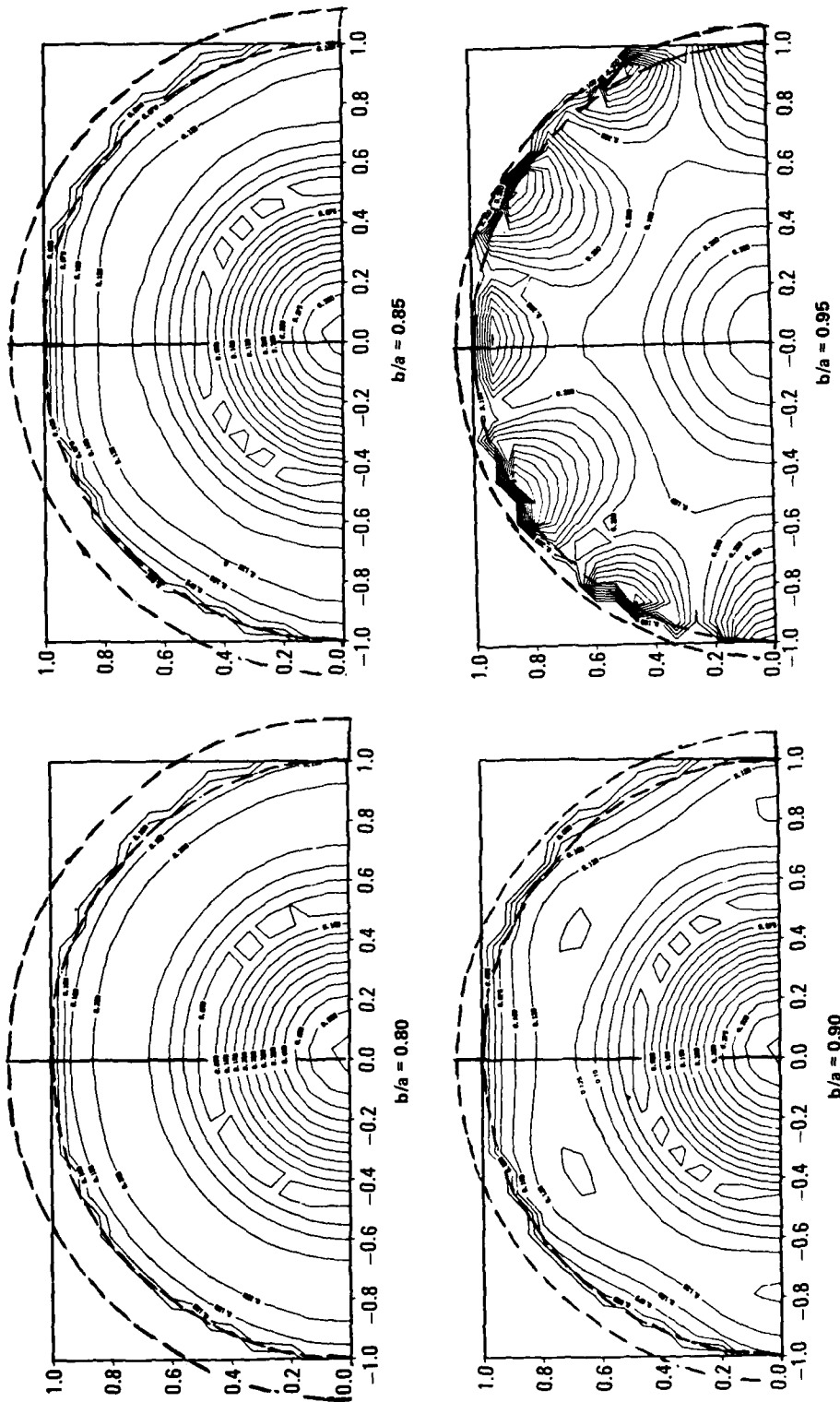


FIGURE 30. INTERNALLY TRANSMITTED ISOBARIC CONTOUR PLOTS FOR A SUBMERGED, AIR-FILLED ALUMINUM SHELL EXTERNALLY EXCITED BY LOAD NO. 1, AT $k_3 a = 5.0$. NO INCIDENT WAVE IS PRESENT HERE. FOUR SHELL-THICKNESSES ARE DISPLAYED HERE: $b/a = 0.80, 0.85, 0.90$ AND 0.95 . THIS IS THE EFFECT OF THE SURFACE LOAD ALONE AS GIVEN IN EQUATIONS (30) AND (26)

AD-A159 936

SOUND TRANSMISSION INTO SHELLS DOUBLY EXCITED BY
INCIDENT WAVES AND BY AR. (U) NAVAL SURFACE WEAPONS
CENTER SILVER SPRING MD G C GAUNAURD ET AL. 15 JAN 85

2/2

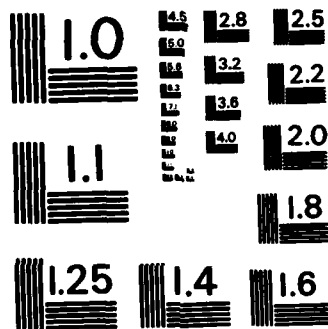
UNCLASSIFIED

NSMC/TR-85-42

F/G 28/1

NL

										END			
										FORMED			
										DTIC			



MICROCOPY RESOLUTION TEST CHART
NATIONAL BUREAU OF STANDARDS-1963-A

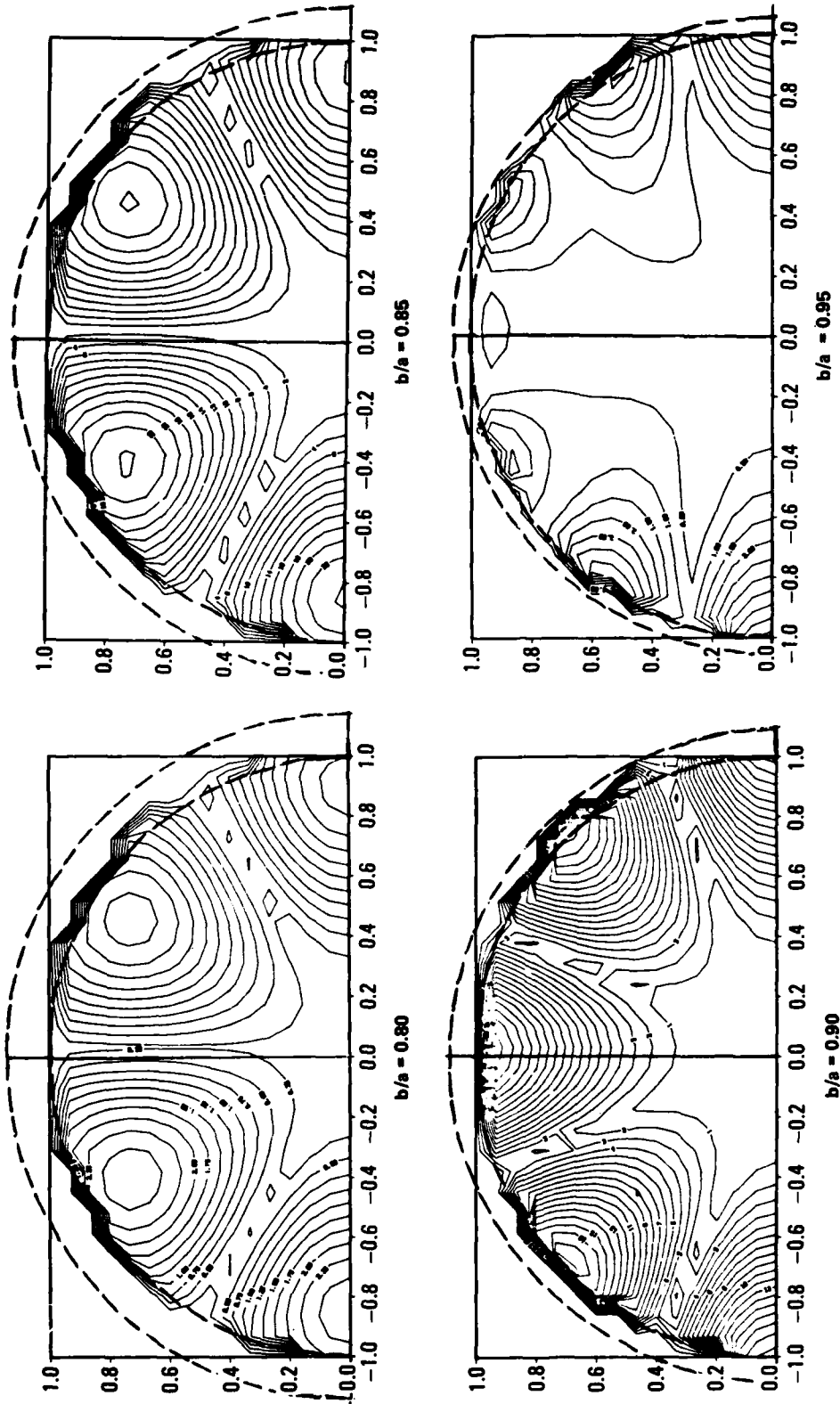


FIGURE 31. INTERNALLY TRANSMITTED ISOBARIC CONTOUR PLOTS FOR A SUBMERGED, AIR-FILLED ALUMINUM SHELL EXTERNALLY EXCITED BY LOAD NO. 2, AT $k_3 a = 5.0$. NO INCIDENT WAVE IS PRESENT HERE. FOUR SHELL-THICKNESSES ARE DISPLAYED HERE: $b/a = 0.80, 0.85, 0.90$ AND 0.95 . THIS IS THE EFFECT ON THE SURFACE LOAD ALONE AS GIVEN IN EQUATIONS (30) AND (26)

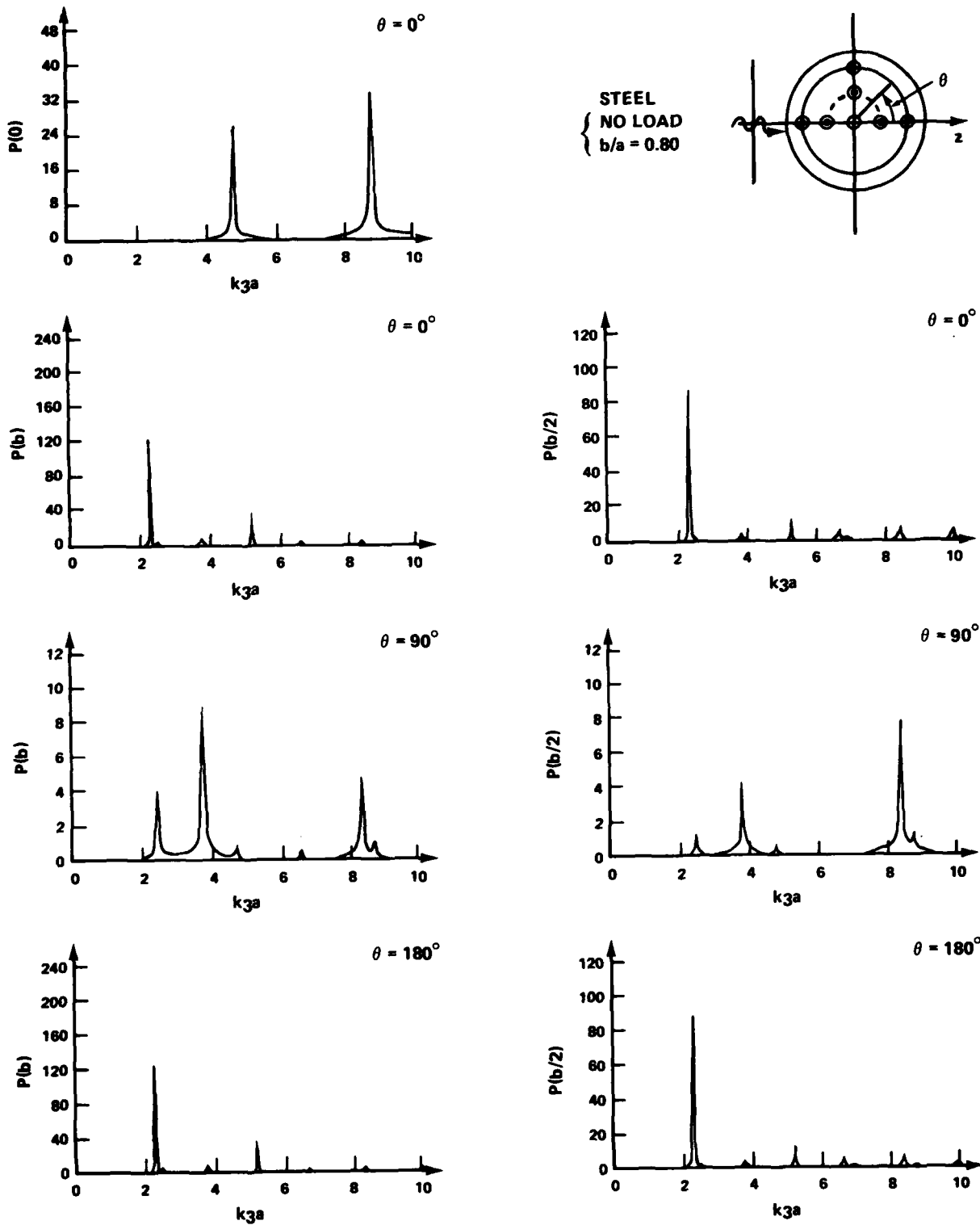


FIGURE 32. INTERIOR PRESSURE LEVELS $|p_3/p_0|$ AT SEVEN POINTS INSIDE AN UNLOADED STEEL SHELL IN WATER INSONIFIED BY A PLANE WAVE, VS. $k_3 a$. THE RELATIVE SHELL-THICKNESS IS $b/a = 0.80$

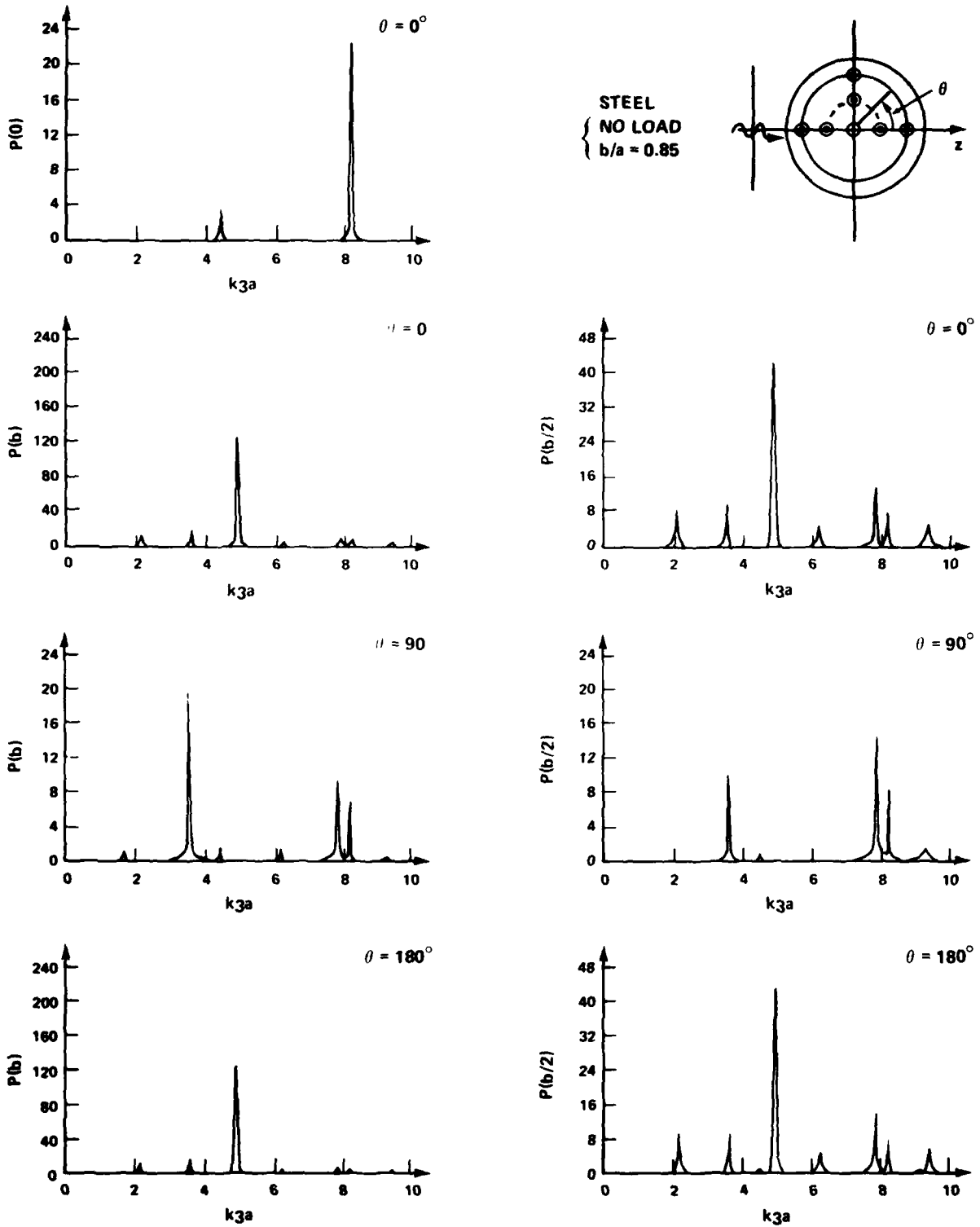


FIGURE 33. INTERIOR PRESSURE LEVELS $|p_3/p_0|$ AT SEVEN POINTS INSIDE AN UNLOADED STEEL SHELL IN WATER INSONIFIED BY A PLANE WAVE, VS. k_3a . THE RELATIVE SHELL-THICKNESS IS $b/a = 0.85$

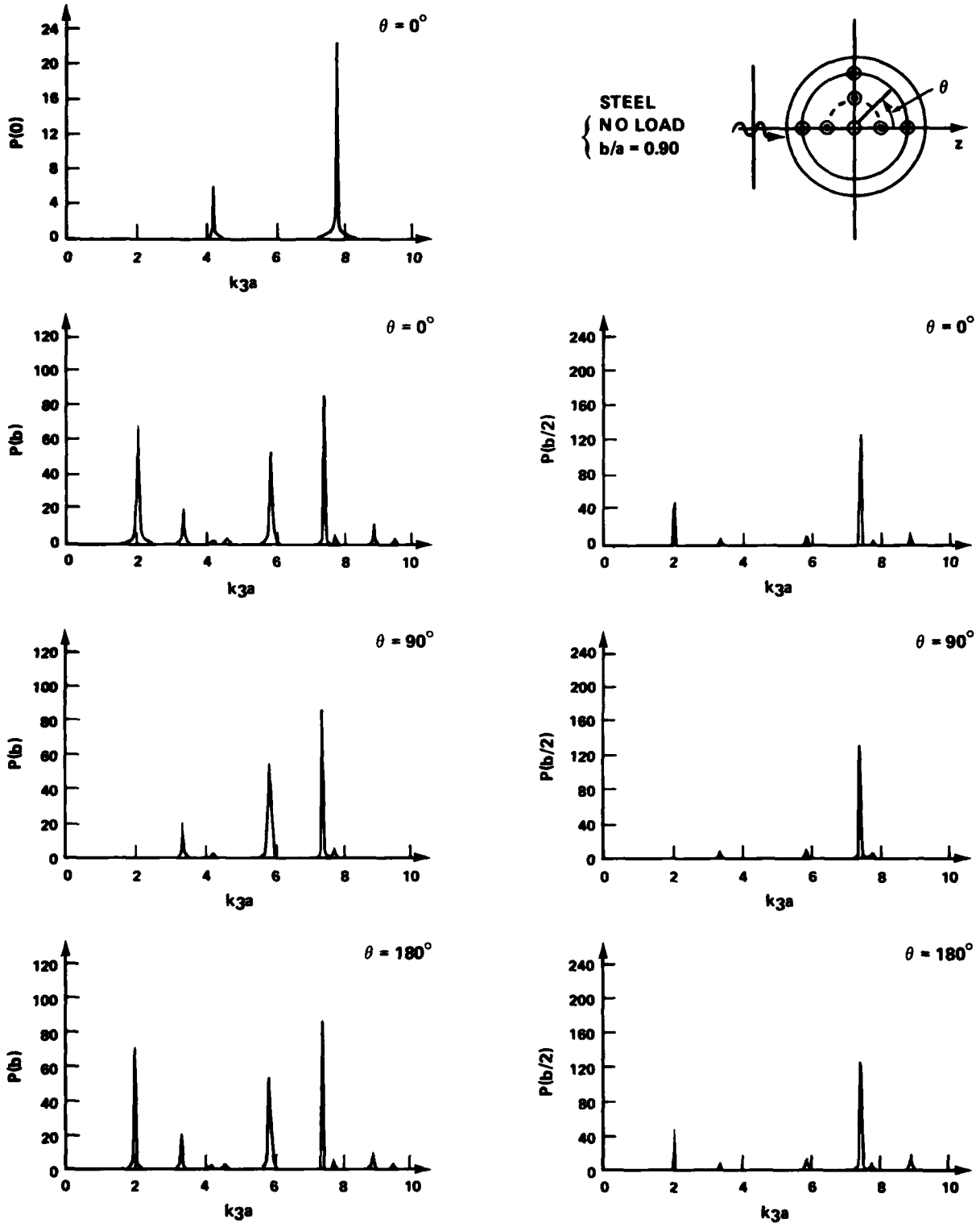


FIGURE 34. INTERIOR PRESSURE LEVELS $|p_3/p_0|$ AT SEVEN POINTS INSIDE AN UNLOADED STEEL SHELL IN WATER INSONIFIED BY A PLANE WAVE, VS. k_3a . THE RELATIVE SHELL-THICKNESS IS $b/a = 0.90$

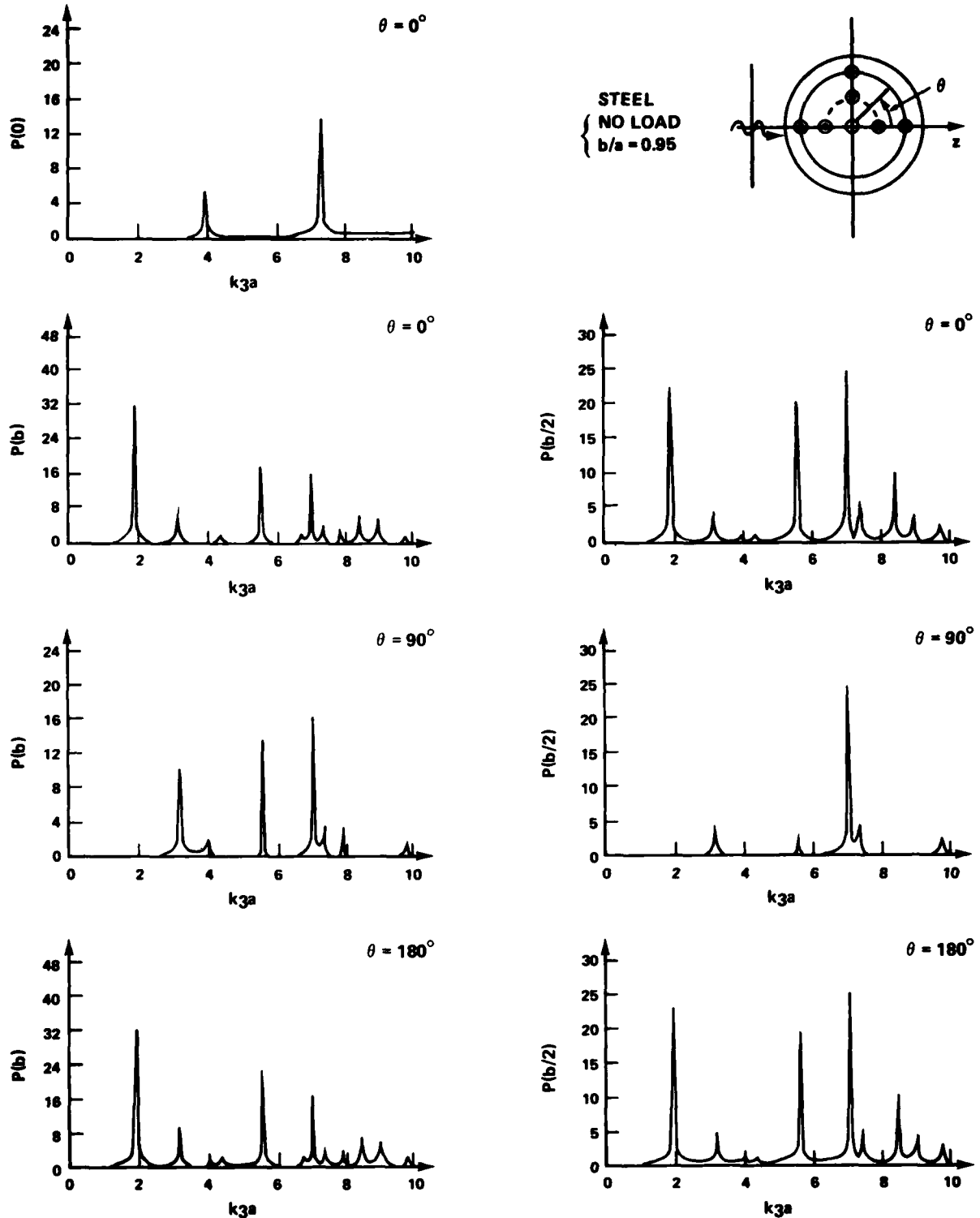


FIGURE 35. INTERIOR PRESSURE LEVELS $|p_3/p_0|$ AT SEVEN POINTS INSIDE AN UNLOADED STEEL SHELL IN WATER INSONIFIED BY A PLANE WAVE, VS. k_3a . THE RELATIVE SHELL THICKNESS IS $b/a = 0.95$

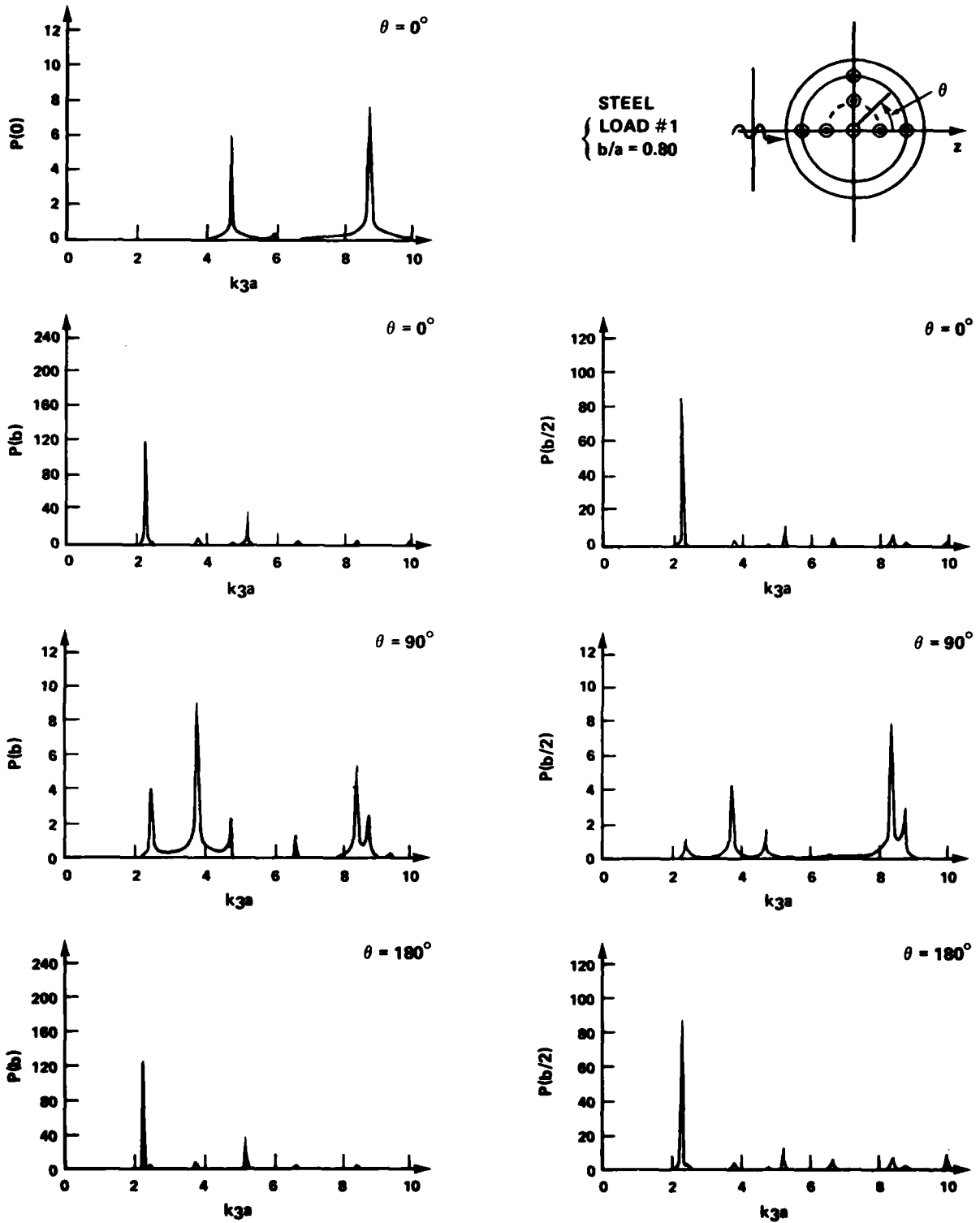


FIGURE 36. INTERIOR PRESSURE LEVELS $|p_3/p_0|$ AT SEVEN POINTS INSIDE A STEEL SHELL IN WATER LOADED WITH LOAD NO. 1, AND INSONIFIED BY A PLANE WAVE, VS. k_3a . THE RELATIVE SHELL THICKNESS IS $b/a = 0.80$

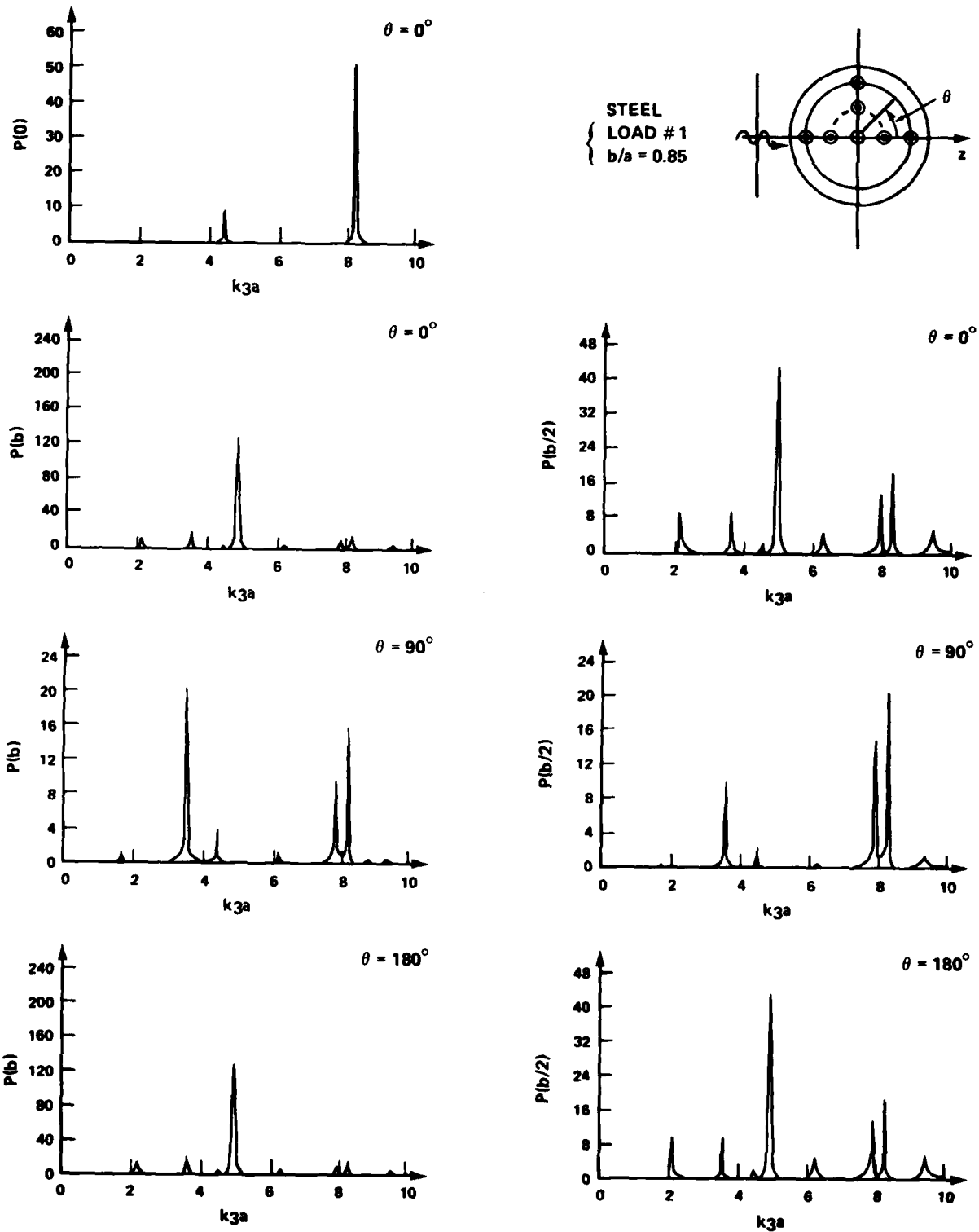


FIGURE 37. INTERIOR PRESSURE LEVELS $|p_3/p_0|$ AT SEVEN POINTS INSIDE A STEEL SHELL IN WATER LOADED WITH LOAD NO. 1, AND INSONIFIED BY A PLANE WAVE, VS. k_3a . THE RELATIVE SHELL THICKNESS IS $b/a = 0.85$

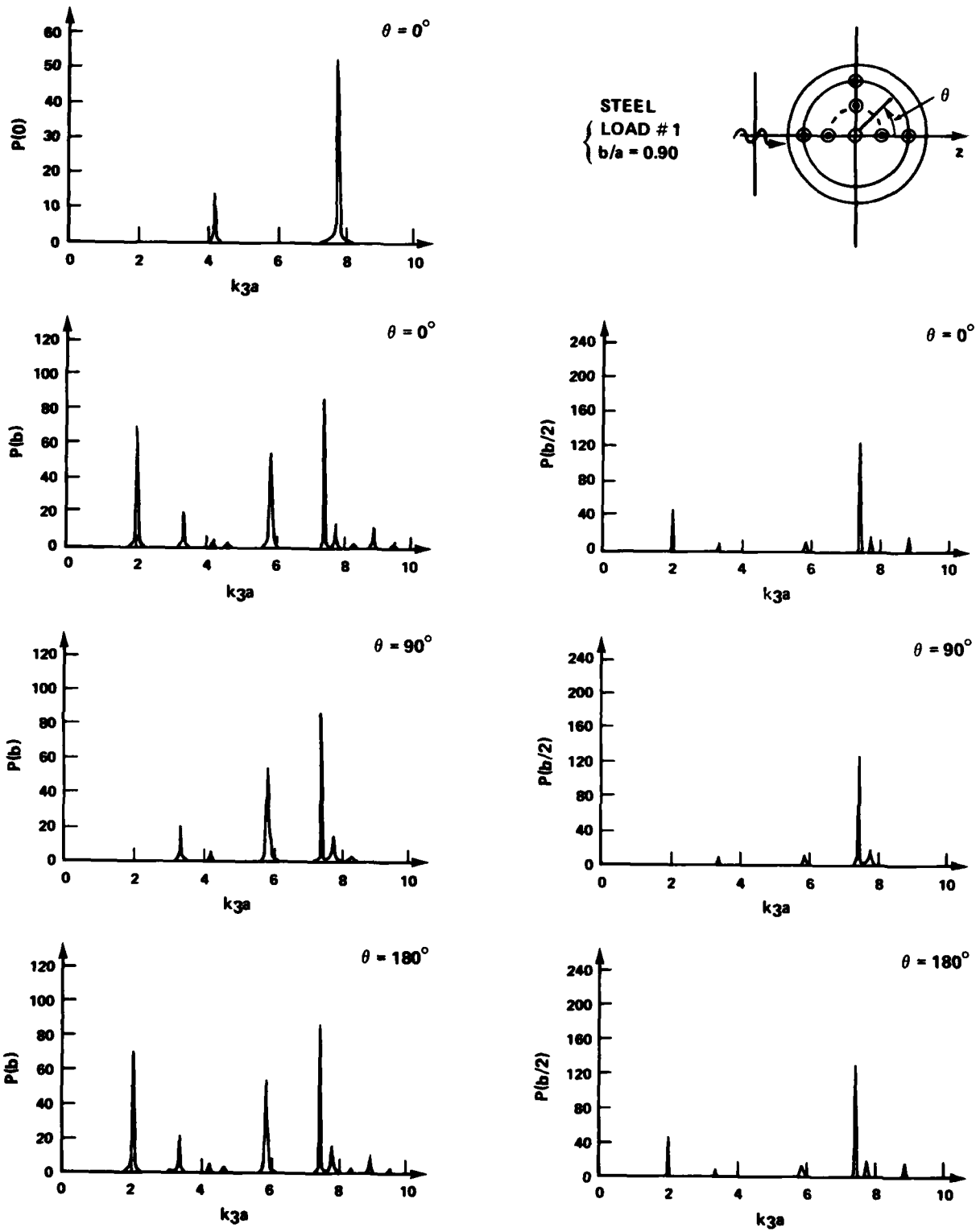


FIGURE 38. INTERIOR PRESSURE LEVELS $|P_3/P_0|$ AT SEVEN POINTS INSIDE A STEEL SHELL IN WATER LOADED WITH LOAD NO. 1, AND INSONIFIED BY A PLANE WAVE VS. k_{3a} . THE RELATIVE SHELL-THICKNESS IS $b/a = 0.90$

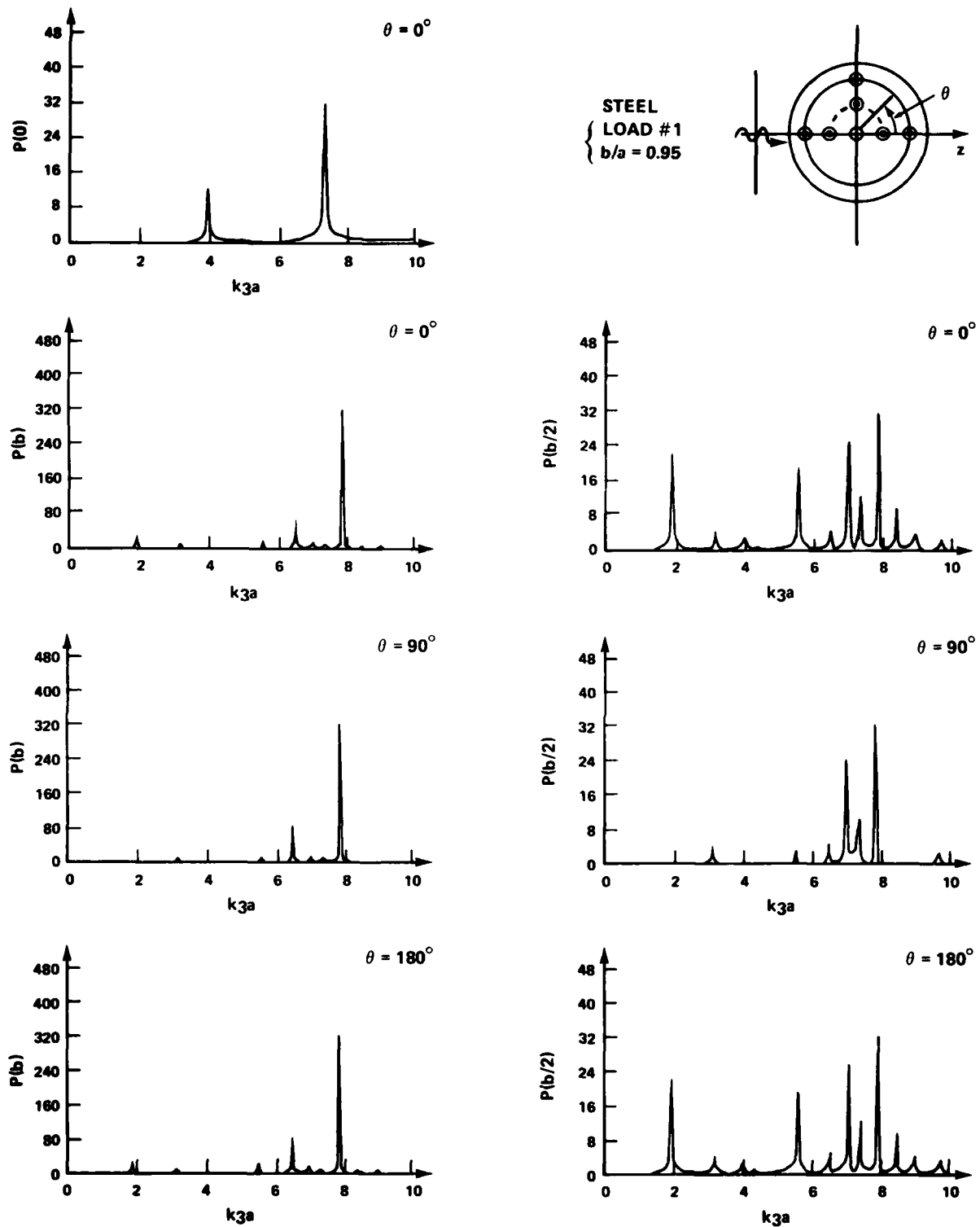


FIGURE 39. INTERIOR PRESSURE LEVELS $|p_3/p_0|$ AT SEVEN POINTS INSIDE A STEEL SHELL IN WATER LOADED WITH LOAD NO. 1, AND INSONIFIED BY A PLANE WAVE VS. k_3a . THE RELATIVE SHELL THICKNESS IS $b/a = 0.95$

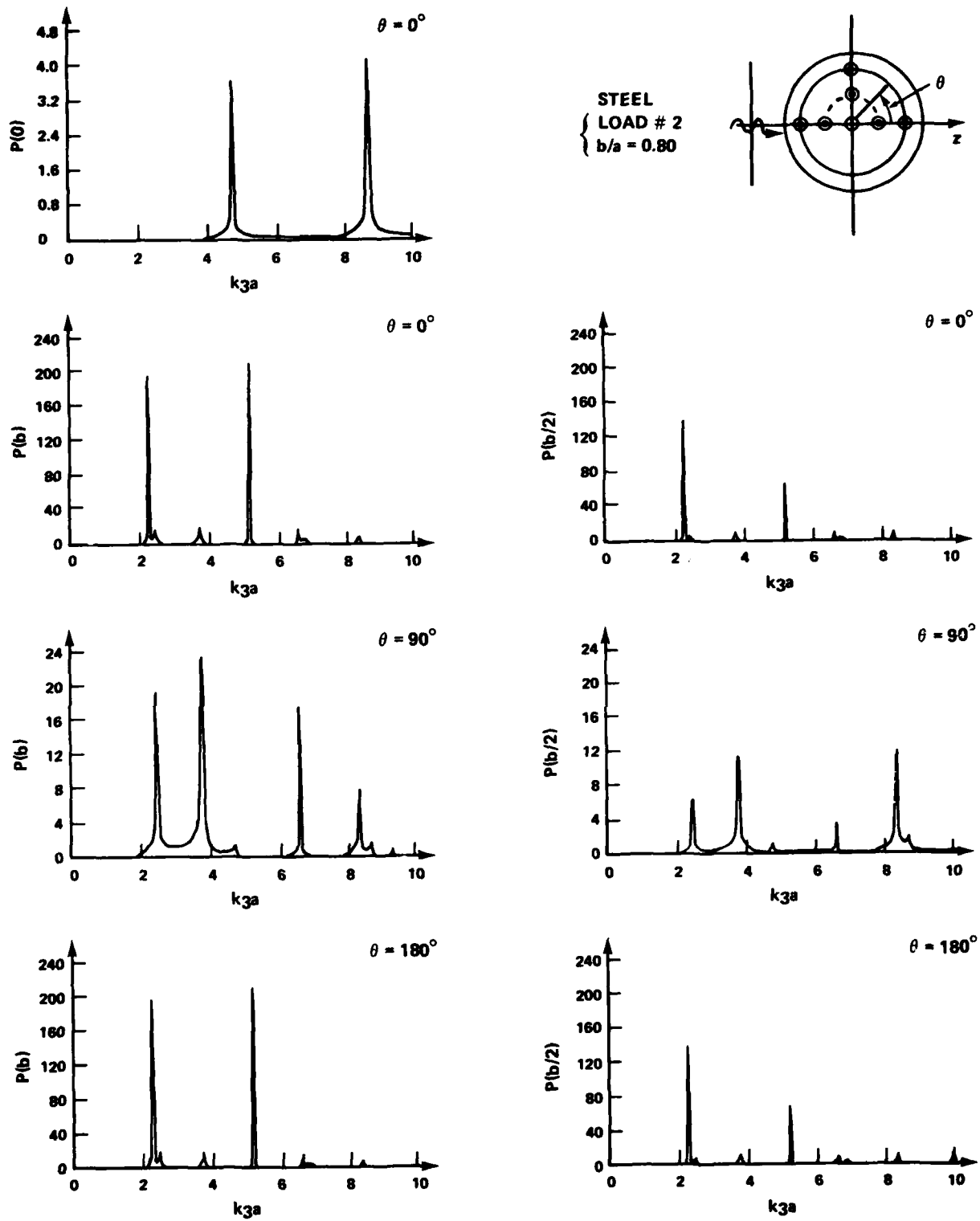


FIGURE 40. INTERNAL PRESSURE LEVELS $|p_3/p_0|$ AT SEVEN POINTS INSIDE A STEEL SHELL IN WATER LOADED WITH LOAD NO. 2, AND INSONIFIED BY A PLANE WAVE, VS. k_3a . THE RELATIVE SHELL-THICKNESS IS $b/a = 0.80$

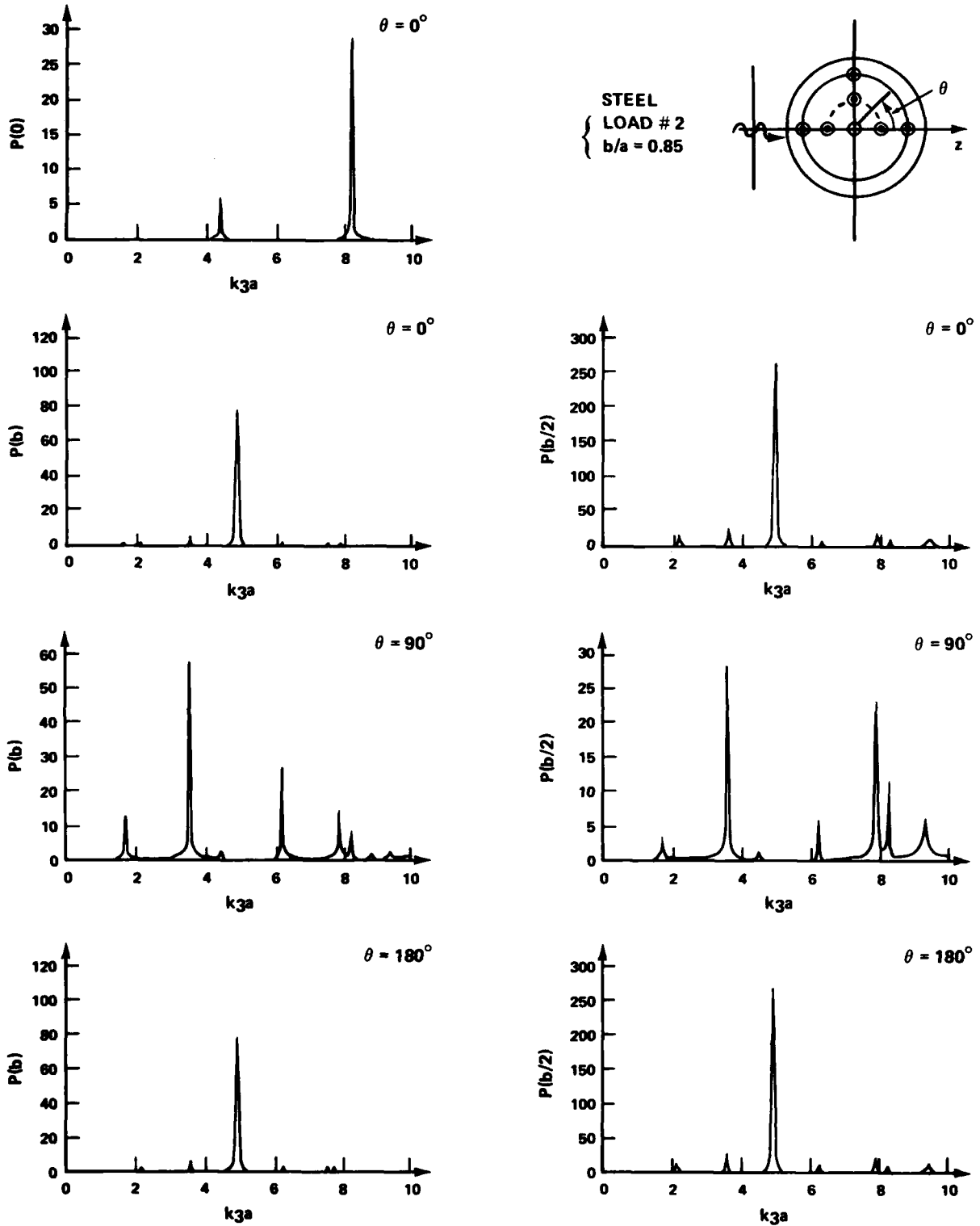


FIGURE 41. INTERNAL PRESSURE LEVELS $|p_3/p_0|$ AT SEVEN POINTS INSIDE A STEEL SHELL IN WATER LOADED WITH LOAD NO. 2, AND INSONIFIED BY A PLANE WAVE VS. k_3a . THE RELATIVE SHELL-THICKNESS IS $b/a = 0.85$

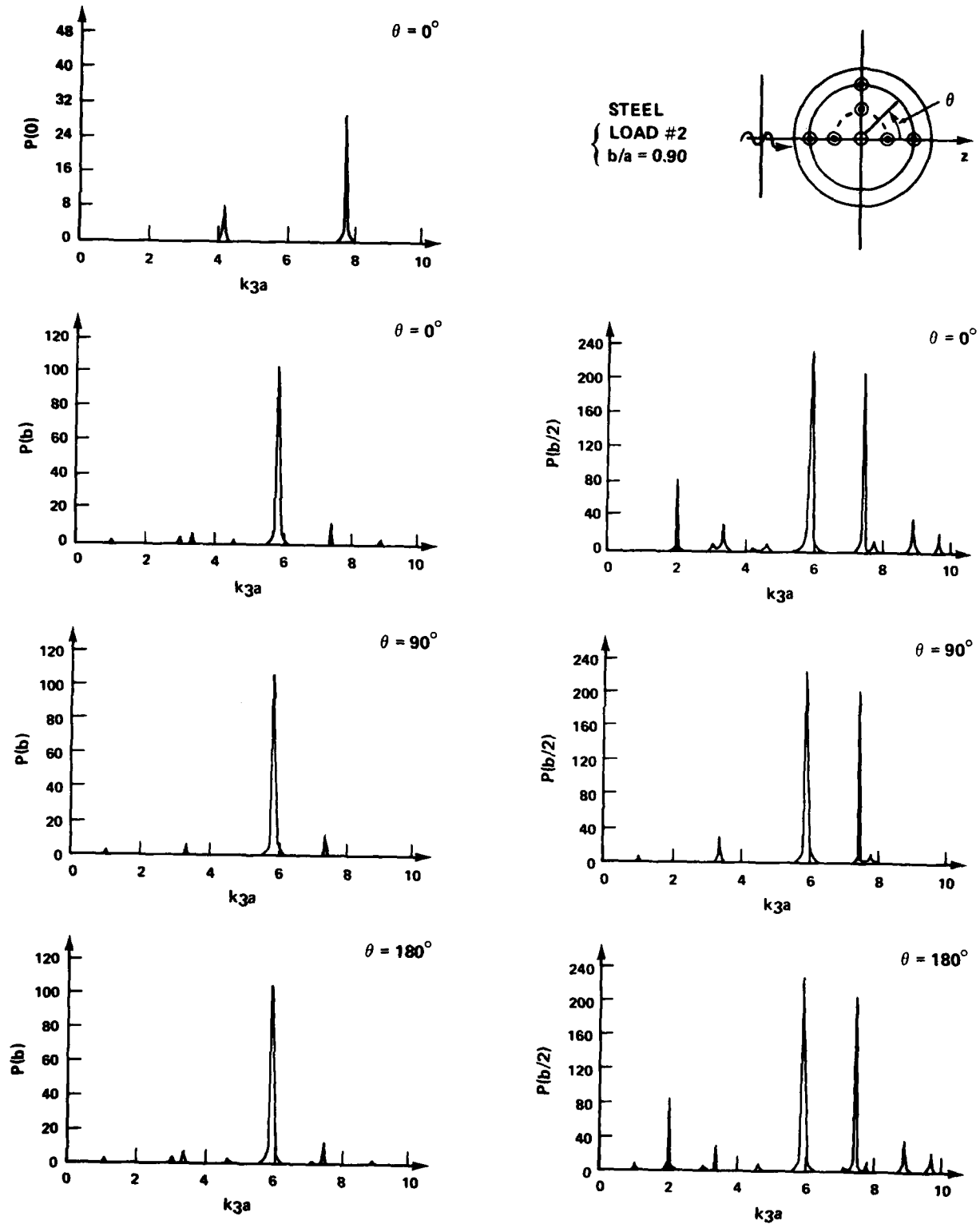


FIGURE 42. INTERNAL PRESSURE LEVELS $|p_2/p_0|$ AT SEVEN POINTS INSIDE A STEEL SHELL IN WATER LOADED WITH LOAD NO. 2, AND INSONIFIED BY A PLANE WAVE VS. k_3a . THE RELATIVE SHELL-THICKNESS IS $b/a = 0.90$

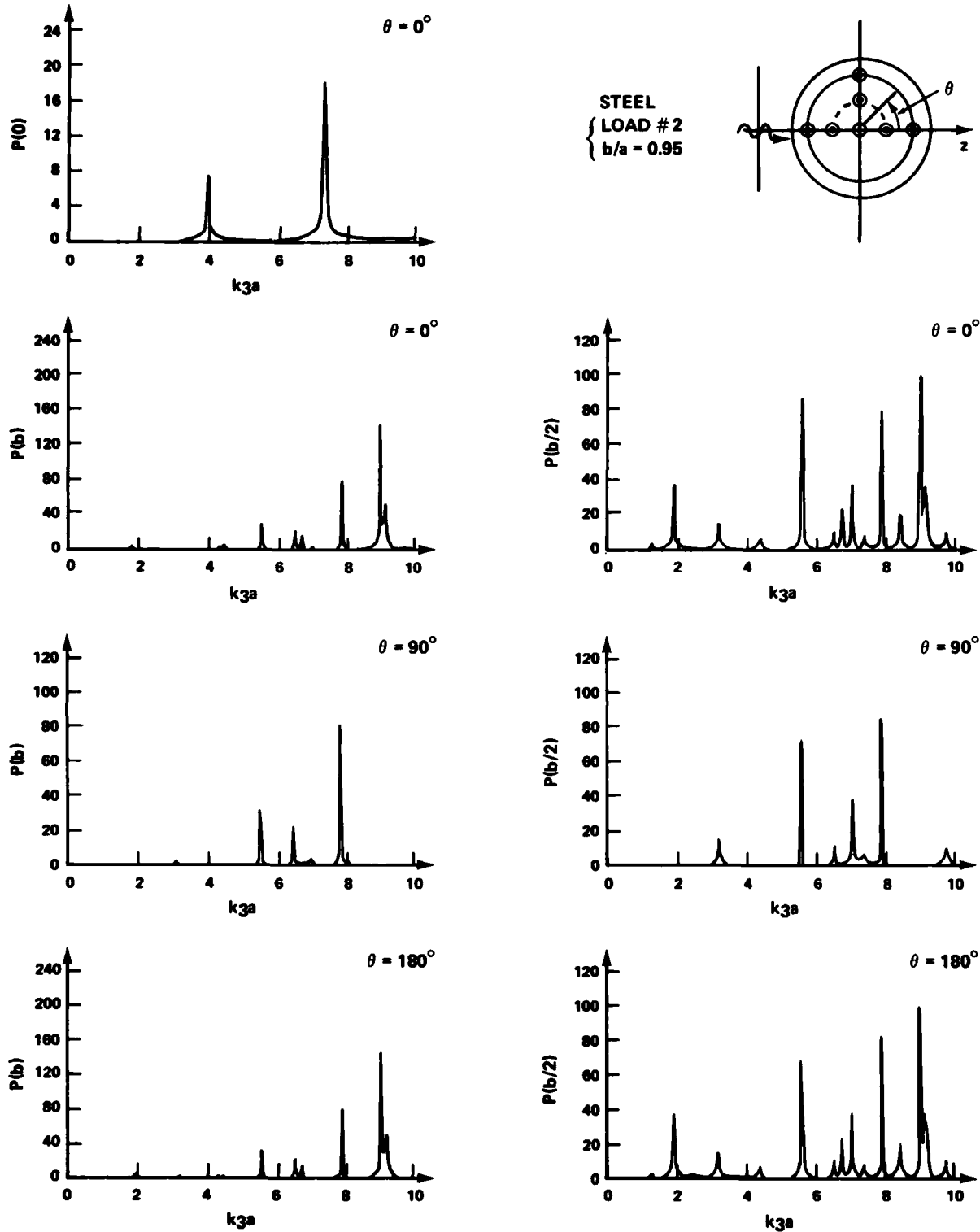


FIGURE 43. INTERNAL PRESSURE LEVELS $|p_3/p_0|$ AT SEVEN POINTS INSIDE A STEEL SHELL IN WATER LOADED WITH LOAD NO. 2, AND INSONIFIED BY A PLANE WAVE VS. k_3a . THE RELATIVE SHELL-THICKNESS IS $b/a = 0.95$

REFERENCES

1. Uginčius, P., Creeping-wave Analysis of Acoustic Scattering by Elastic Cylindrical Shells, Naval Ordnance Laboratory (currently Naval Surface Weapons Center) TR-2128, 26 Feb 1968, p. 108.
2. Junger, M. C., "Sound Scattering by Thin Elastic Shells," J. Acoust. Soc. Amer. Vol. 24., 1952, pp. 366-373.
3. Junger, M. C., "Normal Modes of Submerged Plates and Shells," Fluid-Solid Interaction, pp. 79-119, (Edited by J. E. Greenspon), ASME Press, 1967.
4. Junger, M. C., "Vibrations of Elastic Shells in a Fluid Medium and the Associated Radiation of Sound," J. Appl. Mech., Vol. 14, 1952, pp. 439-445.
5. Gaunaurd, G., "Sonar Cross-section of a Coated Hollow Cylinder in Water," J. Acoust. Soc. Amer., Vol. 61, 1977, pp. 360-368.
6. Gaunaurd, G., "High-frequency Acoustic Scattering From Submerged Cylindrical Shells Coated with Viscoelastic Layers," J. Acoust. Soc. Amer., Vol. 62, 1977, pp. 503-512.
7. Doolittle, R. D. and Überall, J., "Sound Scattering by Elastic Cylindrical Shells," J. Acoust. Soc. Amer., Vol. 39, 1966, pp. 272-275.
8. Gaunaurd, G. and Überall, H., "Suppression of Resonant Modes from the Backscattered Echoes, of Acoustically Coated, Air-filled, Cylindrical Shell in Water," Proceedings, IV (Hydroacoustics) Symposium on Ship-Related Acoustical R&D, ONR Report, Vol. 1B, 1979, pp. 189-218.
9. Gaunaurd, G. and Brill, D., "Acoustic Spectrogram and Complex-frequency Poles of a Resonantly Excited Elastic Tube," J. Acoust. Soc. Amer., Vol. 75, 1984, pp. 1680-1693.
10. Gaunaurd, G., "Target Strength Reduction from Viscoelastically Coated Cylinders," in Proceedings, III United States/Federal Republic of Germany Hydroacoustics Symposium, Munich, FRG, May 1975, Vol. 1, Pt. 2, 1975, pp. 4-31.
11. Flux, L. and Neubauer, W., "Acoustic Reflection from Layered Elastic Cylinders," J. Acoust. Soc. Amer., Vol. 61, 1977, pp. 307-312.

REFERENCES (CONT.)

12. Gaunard, G. and Kalnins, A., "Resonances in the Sonar Cross Sections of Coated Shells," Intern. J. Solids and Structures, Vol. 18, 1982, pp. 1083-1102.
13. Huang, H. and Wang, Y., "Transient Interactions of Spherical Acoustic Waves and a Cylindrical Elastic Shell," J. Acoust. Soc. Amer., Vol. 48, (#1), 1970, pp. 228-235, 50
14. Huang, H. and Wang, Y., J. Acoust. Soc. Amer., Vol. 50, 1971, pp. 885-891.
15. Huang, H., Lu, Y. and Wang, Y., "Transient Interaction of Spherical Acoustic Waves, a Cylindrical Elastic Shell, and its Internal Mechanical Systems," J. Acoust. Soc. Amer., Vol. 56, 1974, pp. 4-10.
16. Gaunard, G., Methods for Solving the (Visco) Elasticity Equations for Cylinder and Sphere Problems, NSWC TR 76-20, Mar 1976, Table 2, Case D.
17. Gaunard, G., et al., "Giant Monopole Resonances in the Scattering of Waves From Air-filled Spherical Cavities and Bubbles," J. Acoust. Soc. Amer., Vol. 64, 1979, pp. 573-594.
18. Gaunard, G. and Überall, H., "Numerical Evaluation of Modal Resonances in the Echoes of Compressional Waves Scattered from Fluid-filled Cavities in Solids," Journ. of Applied Physics, Vol. 50, 1979, pp. 4642-4660.
19. Gaunard, G. et al., "Inverse Scattering and the Resonances of Viscoelastic and Electromagnetic Systems," Wave Propagation in Viscoelastic Media, Pitman Ltd., London, pp. 234-287, F. Mainardi, Editor, 1982 (Invited review chapter).
20. Flax, L., Gaunard, G. and Überall, H., "The Theory of Resonance Scattering" in Physical Acoustics, Vol. 15, Ch. 3, W. P. Mason and R. N. Thurston, Eds., Academic Press, 1981, pp. 191-294.
21. Gaunard, G. and Überall, H., "RST Analysis of Monostatic and Bistatic Acoustic Echoes from an Elastic Sphere," J. Acoust. Soc. Amer., Vol. 73, 1983, pp. 1-12.
22. Gaunard, G., et al., "Interior and Exterior Resonances in Acoustic Scattering I: Spherical Targets," Il Nuovo Cimento, Vol. 76B, (#2), 1983, pp. 153-175.
23. Gaunard, G. and Brill, D., "Acoustic Resonance Scattering by a Penetrable Cylinder," J. Acoust. Soc. Amer., Vol. 73, 1983, pp. 1448-1455.
24. Gaunard, G. and Überall, H., "The Theory of Resonance Scattering from Spherical Cavities in Viscoelastic Media," J. Acoust. Soc. Amer., Vol. 63, 1978, pp. 1699-1712.

REFERENCES (CONT.)

25. Gaunard, G., and Barlow, J., "Sound Transmission into Arbitrarily Loaded, Resonating Shells", presented at the 108th Meeting of the Acoustical Society of America, Minneapolis, MN; abstract in the program, in J. Acoust. Soc. Amer., Vol. 76, (Supplement), 1984, p. S65.
26. Gaunard, G., and Barlow, J., "Resonance Sound-transmission into Arbitrarily Loaded Submerged Cylindrical Shell", J. Acoust. Soc. Amer., Vol., 78, (#1), 1985. pp. 15-25.

APPENDIX A
NON-VANISHING ELEMENTS OF THE MATRICES

The 30 non-vanishing elements of the matrices D and A* are as follows:

$$d_{11} = \left(\frac{\rho_1}{\rho_2}\right) k_{s_2}^2 a^2 H_n^{(1)}(k_1 a)$$

$$d_{12} = (2n^2 - k_{s_2}^2 a^2) J_n(k_{d_2} a) - 2k_{d_2} a J_n'(k_{d_2} a)$$

$$d_{13} = (2n^2 - k_{s_2}^2 a^2) Y_n(k_{d_2} a) - 2k_{d_2} a Y_n'(k_{d_2} a)$$

$$d_{14} = 2n[k_{s_2} a J_n'(k_{s_2} a) - J_n(k_{s_2} a)]$$

$$d_{15} = 2n[k_{s_2} a Y_n'(k_{s_2} a) - Y_n(k_{s_2} a)]$$

$$d_{21} = -k_1 a H_n^{(1)}(k_1 a)$$

$$d_{22} = k_{d_2} a J_n'(k_{d_2} a)$$

$$d_{23} = k_{d_2} a Y_n'(k_{d_2} a)$$

$$d_{24} = n J_n(k_{s_2} a)$$

$$d_{25} = n Y_n(k_{s_2} a)$$

$$d_{32} = 2n[J_n(k_{d_2} a) - k_{d_2} a J'_n(k_{d_2} a)]$$

$$d_{33} = 2n[Y_n(k_{d_2} a) - k_{d_2} a Y'_n(k_{d_2} a)]$$

$$d_{34} = 2k_{s_2} a J'_n(k_{s_2} a) + [k_{s_2}^2 a^2 - 2n^2] J_n(k_{s_2} a)$$

$$d_{35} = 2k_{s_2} a Y'_n(k_{s_2} a) + [k_{s_2}^2 a^2 - 2n^2] Y_n(k_{s_2} a)$$

$$d_{42} = -2k_{d_2} b J'_n(k_{d_2} b) + [2n^2 - k_{s_2}^2 b^2] J_n(k_{d_2} b)$$

$$d_{43} = -2k_{d_2} b Y'_n(k_{d_2} b) + [2n^2 - k_{s_2}^2 b^2] Y_n(k_{d_2} b)$$

$$d_{44} = 2n[k_{s_2} b J'_n(k_{s_2} b) - J_n(k_{s_2} b)]$$

$$d_{45} = 2n[k_{s_2} b Y'_n(k_{s_2} b) - Y_n(k_{s_2} b)]$$

$$d_{46} = \left(\frac{\rho_3}{\rho_2}\right) k_{s_2}^2 b^2 J_n(k_3 b)$$

$$d_{52} = k_{d_2} b J'_n(k_{d_2} b)$$

$$d_{53} = k_{d_2} b Y'_n(k_{d_2} b)$$

$$d_{54} = n J_n(k_{s_2} b)$$

$$d_{55} = n Y_n(k_{s_2} b)$$

$$d_{56} = -k_3 b J'_n(k_3 b)$$

$$d_{62} = 2n[J_n(k_{d_2} b) - k_{d_2} b J'_n(k_{d_2} b)]$$

$$d_{63} = 2n[Y_n(k_{d_2} b) - k_{d_2} b Y'_n(k_{d_2} b)]$$

$$d_{64} = 2k_{s_2} b J'_n(k_{s_2} b) + (k_{s_2}^2 b^2 - 2n^2) J_n(k_{s_2} b)$$

$$d_{65} = 2k_{s_2} b Y'_n(k_{s_2} b) + (k_{s_2}^2 b^2 - 2n^2) Y_n(k_{s_2} b)$$

$$A_1^* = -\left(\frac{\rho_1}{\rho_2}\right) k_{s_2}^2 a^2 J_n(k_1 a)$$

$$A_2^* = k_1 a J'_n(k_1 a)$$

DISTRIBUTION

	<u>Copies</u>		<u>Copies</u>
Chief		Commander	
Office of Naval Research		Naval Underwater Systems Center	
Attn: Code 432	4	Attn: Code 44	1
Code 425	2	Dr. W. Von Winkel	1
Code 102B	1	Code 601 (Mr. T. Bell)	1
Code 220	1	Technical Library	1
ACSAS Office		New London, CT 06320	
(A. Allintheorpe)	1		
800 N. Quincy Street		Library of Congress	
Arlington, VA 22217		Attn: Gift and Exchange Div.	4
		Washington, DC 20540	
Defense Technical Information			
Center		Commander	
Cameron Station		Naval Weapons Center	
Alexandria, VA 22314	12	Attn: Technical Library	1
		China Lake, CA 93555	
Commander			
Naval Research Laboratory		Commander	
Attn: Code 5830	1	Naval Underwater Systems Center	
Code 2620	1	Attn: Technical Library	1
Washington, DC 20375		Newport, RI 02841	
Commander		Commander	
David W. Taylor Naval Ship Research		Naval Research Laboratory	
& Development Center		Underwater Sound Reference	
Attn: Code 1905.4	1	Detachment	
Code 1720	1	Attn: Technical Library	1
Code 1965	1	Orlando, FL 32856	
Code 1844	1		
Code 1908	1	Chief of Naval Operations	
Code 1721 (Dr. R. F. Jones)	1	Attn: Code OP-098	1
Bethesda, MD 20084		Code OP-981H	1
		Department of the Navy	
		Washington, DC 20350	

DISTRIBUTION (Cont.)

	<u>Copies</u>		<u>Copies</u>
Commander Naval Sea Systems Command Attn: Code 05R25 Code 05R26 Code 55N (R. Biancardi) Washington, DC 20362	1 1 1	Chief Office of Naval Technology Attn: Dr. T. Kooij 800 N. Quincy Street Arlington, VA 22217	1
Commander Naval Air Systems Command Attn: Code 03D Code 7226 Washington, DC 20361	1 1	Commander Naval Electronic Systems Command Attn: ELEX 612A Washington, DC 20363	1
Director Naval Research Laboratory Attn: Dr. Joseph E. Blue Dr. Anthony J. Rudgers Undersound Sound Reference Detachment P. O. Box 8337 Orlando, FL 32856	1 1	Naval Postgraduate School Attn: Technical Library Monterey, CA 93940	1
U. S. Naval Academy Mechanical Engineering Department Annapolis, MD 21402	1	OUSDR&E, The Pentagon Attn: Mr. Jerome Persh Staff Specialist for Materials and Structures Room 3D1089 Washington, DC 20301	1
Commander Naval Ocean Systems Center Attn: R. Bologna, Bldg. 175 San Diego, CA 92132	1	Weidlinger Associates Attn: Dr. M. L. Baron 333 Seventh Avenue New York, NY 10001	1
Chief of Naval Operations Attn: OP-21T (Dr. E. Harper) Washington, DC 20350-2000	1	Pennsylvania State University Applied Research Laboratory Department of Physics Attn: Professor E. J. Skudryk State College, PA 16801	1
ASW Systems Program Office (PM-4) Attn: ASW-122 Washington, DC 20362	1	Stanford University Department of Applied Mechanics Attn: Professor G. Herrmann Stanford, CA 94305	1
SSBN Security Attn: OP-2130 Washington, DC 20350	1	Catholic University of America Department of Mechanical Engineering Attn: Professor J. A. Clark Washington, DC 20064	1
Commander Naval Sea Systems Command Attn: SEA-06R Washington, DC 20362	1		

DISTRIBUTION (Cont.)

	<u>Copies</u>		<u>Copies</u>
University of Maryland Department of Mechanical Engineering Attn: Professor J. C. S. Yang College Park, MD 20742	1	Georgia Institute of Technology Department of Mechanical Engineering Attn: Professor J. H. Ginsburg Atlanta, GA 30332	1
Dr. R. D. Mindlin P. O. Box 385 Grantham, NH 03753	1	Stanford University Department of Civil Engineering Attn: Professor P. Pinsky Stanford, CA 94305	1
Lockheed Missiles and Space Company Attn: Dr. T. L. Geers 3251 Hanover Street Palo Alto, CA 94303	1	Drexel University Department of Mechanical Engineering and Mechanics Attn: Professor J. Awerbuch Philadelphia, PA 19104	1
Pennsylvania State University Applied Research Laboratory Attn: Dr. S. I. Hayek P. O. Box 30 State College, PA 16804	1	J. G. Engineering Research Associates Attn: President 3831 Menlo Drive Baltimore, MD 21215	1
Cambridge Acoustical Associates Attn: Dr. M. C. Junger 54 Rindge Avenue Extension Cambridge, MA 02140	1	Internal Distribution:	
North Carolina State University Mechanical Engineering Department Attn: Professor R. Keltie Raleigh, NC 27650	1	R	1
Anatech International Corp. Attn: Dr. R. S. Dunham 3344 North Torrey Pines Court Suite 320 LaJolla, CA 92037	1	R04	1
University of Texas Department of Engineering Mechanics Attn: Professor E. Becker Austin, TX 78712-1085	1	R40	1
		R43 (G. Gaunaud)	21
		R14	1
		R14 (Dr. H. Huang)	1
		E35 (GIDEP Office)	1
		U	1
		U20	1
		U21 (Dr. Stevenson)	1
		E231	9
		E232	3

END

FILMED

11-85

DTIC